UNIVERSITÀ DEGLI STUDI DI PADOVA
DIPARTIMENTO DI INGEGNERIA CIVILE, EDILE E AMBIENTALE
Department Of Civil, Environmental and Architectural Engineering

Corso di Laurea Magistrale in Environmental Engineering

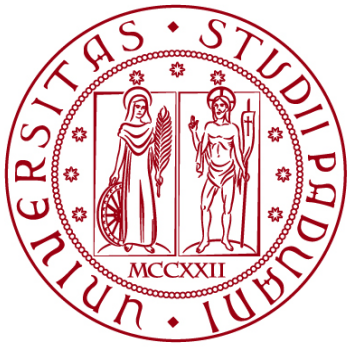

MASTER THESIS

EXPERIMENTAL INVESTIGATIONS ON A SALTMARSH RESTORATION PROJECT IN THE VENICE LAGOON

Supervisor:
PROF. PIETRO TEATINI
Co-supervisor:
PROF. CLAUDIA ZOCCARATO

Candidate:
LEONARDO SERAFINI
2089573

ANNO ACCADEMICO 2023-2024

Table of contents

ABSTRACT

The unique ecosystem of the Venetian Lagoon plays a crucial role in mitigating the impacts of human activity, including climate change, which poses significant threats to Venice. Salt marshes, a key component of this ecosystem, have significantly declined over the past centuries. This thesis aims to contribute to the ongoing research efforts in lagoon restoration focusing on the artificial salt marsh Le Sorelle-B. The research employs using the advanced NATSUB3D simulator, integrating extensive geological, geomechanical, and topographical data to investigate and model the marsh behavior over time. A primary objective of this study is to assess the model cability to forecast the medium and long-term evolution of this landform following itsconstruction. This predictive ability could prove pivotal for informing and optimizing future restoration projects in the Venetian Lagoon and similar coastal environments.

The study is focused on monitoring and modeling nourishment activities, sediment autocompaction, and subsequent subsidence that have largely modified the marsh landform. Novel monitoring techniques developed by the University of Padua in collaboration with the NGO We are Here Venice ETS, specifically the Nourishment Elevation Change (NEC) stations, were employed for validation and calibration of the model. The NATSUB3D simulator was used to model the marsh's evolution over the Holocene to present day, demonstrating that the medium-term evolution depends heavily on the geomechanical behavior of the layers formed during this period and the sediments deposited through nourishment.

The modeling results highlighted several factors that increase the model's response variability, emphasizing the importance of accurately quantifying geomechanical properties of compressible soils for reliable predictions. Significant subsurface compaction was observed, particularly in a shallow peat layer, with nourishment soil also compacting significantly. Future assessments with more specific field data

are expected to provide more accurate results. Currently, the marsh's ultimate elevation is predicted to be within a range that ensures its survivability in the mid-term.

INTRODUCTION

The complex and fragile ecosystem of the Venetian Lagoon makes a significant contribution to mitigate the impacts of human activity – including climate change – that threaten the city of Venice itself. Salt marshes are coastal wetlands that play a critical role in this ecosystem. Typical of the Venice lagoon but occurring worldwide, particularly in middle to high latitudes, they are flooded and drained by salt water brought in by the tides: thriving along protected shorelines, they are a common valuable habitat in estuaries providing several critical services (Gambolati 1973a). These intertidal habitats are essential for healthy fisheries, coastlines, and communities but in the past decades they declined significantly: four centuries ago, the Venice Lagoon encompassed ~250 km^2 of salt marshes, presently only ~45 km^2 (Finotello et al. 2023).

The awareness and the need to take countermeasures rose in recent years and several restoration projects are trying to reverse this trend in the lagoon through build up of artificial new salt marshes, protection actions onto existing ones and rising citizen's awareness activities.

This thesis work contributes to these efforts and aims to investigate and to numerically model Le Sorelle-B - one of these artificial salt marshes - by means of the advanced NATSUB3D simulator and a comprehensive dataset of geological, geomechanical, and topographical measurements collected in the study area. The capabilities of the model in forecasting the middle and long-term behaviour of the artificial salt marsh after its construction are assessed: if verified, the model could be a key tool in restoration projects.

Novel techniques are used and were developed by the partnership between the University of Padua and the non-governative organization We are Here Venice ETS to monitor soil compaction. The latter is involved in the VITAL initiative which began in 2019 in partnership with the LagunaB experts' group.

A previous thesis work, made by eng. Giulia Meneghini, was focused on the same salt marsh and with similar objectives, but further on-site investigations and improvements on the numerical model enabled to describe actual conditions and the future evolution of the investigated salt marsh.

An overview of the Venice Lagoon context and challenges, and a brief description of salt marshes in general are provided in the Chapter 1. The following one contains a comprehensive description of the study site and the summary of the investigation and monitoring activities, including the novel Nourishment Elevation Change stations, along with their procedure and some results. Chapter 3 focuses on the NATSUB3D simulator going through the governing and constitutieve equations, the model implementation and solving, and the main simulator capabilities and features. Chapter 5 and 6, report the model and the monitoring data analysis results, respectively. In the last chapter conclusions and limitations of the study are discussed.

1. SALT MARSHES AND CHALLENGES IN THE VENICE LAGOON

The Venice Lagoon is the largest Italian lagoon and has a surface area of approximately 550 km^2, of which 418 km^2 are open to the tidal excursions of the Upper Adriatic Sea, the largest in the Mediterranean. The sea and the lagoon communicate with each other through three port inlets: Lido, Malamocco, Chioggia. 78% of the surface of the Venice Lagoon is characterized by large bodies of water, crossed by a dense network of canals of varying depths (mosevenezia.eu).

Salt marshes are typical of the Venice Lagoon morphology and, generally speaking, they are part of world Estuarine and Coastal Ecosystems (ECEs). The global decrease in ECEs is known to affect at least three critical ecosystem services (Worm et al. 2006): the number of viable (noncollapsed) fisheries (33% decline); the provision of nursery habitats such as oyster reefs, seagrass beds, and wetlands (69% decline); and filtering and detoxification services provided by suspension feeders, submerged vegetation, and wetlands (63% decline) (Barbier et al. 2011).

The Venice Lagoon salt marshes have faced centuries of decline due to human intervention and they are suffering from a combination of land **subsidence** – the city foundations and the lagoon are slowly sinking into the lagoon subsoil on which they are built – and **rising sea levels**. According to IPCC (Calvin et al. 2023), in the worst-case scenario, it could disappear underwater by the year 2100.

Mismanagement practices dating back to the 1500s, including river diversions (e.g., Taglio del Sile), have deprived the lagoon of essential sediment. Subsequent construction of breakwaters and a shipping canal further exacerbated this issue. While Venice has invested heavily in flood protection measures like the Mo.S.E. barrier system, the salt marshes have been largely overlooked.

Studies from 1970 to 2015 indicate a global loss of 33-35% in salt marsh area (Campbell et al., n.d.) (Figure 1.1). The Venice Lagoon has experienced a similar ecline, with current salt marsh coverage at 8%, down from 25% a century ago (Atlante della laguna di Venezia, 2012). Historical records indicate a significant reduction in Venice Lagoon's marsh area from 180 km^2 to just 43 km^2 over the past two centuries (Figure 1.2). The primary causes of this loss include erosion, due to waves generated by wind and increased maritime traffic, and artificial interventions in response to rising sea levels that limit sediments budget and land subsidence.

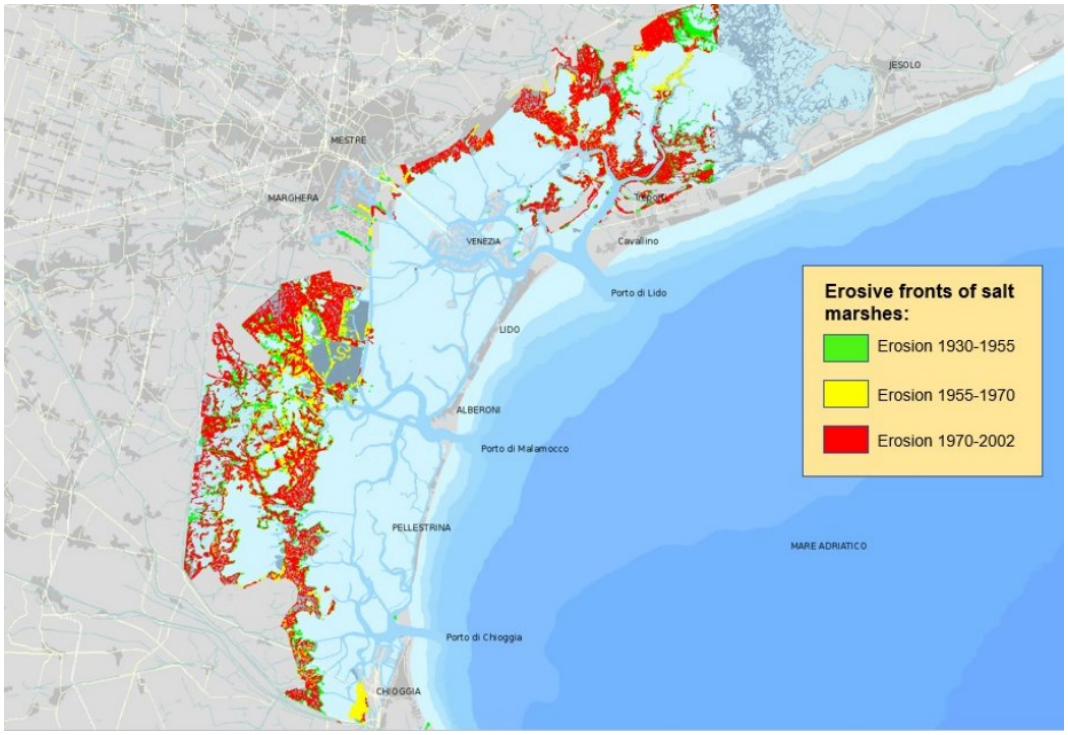

Figure 1.1. Salt marsh erosion in the Venice Lagoon between 1930 and 2002 (Atlante della laguna di Venezia, 2012).

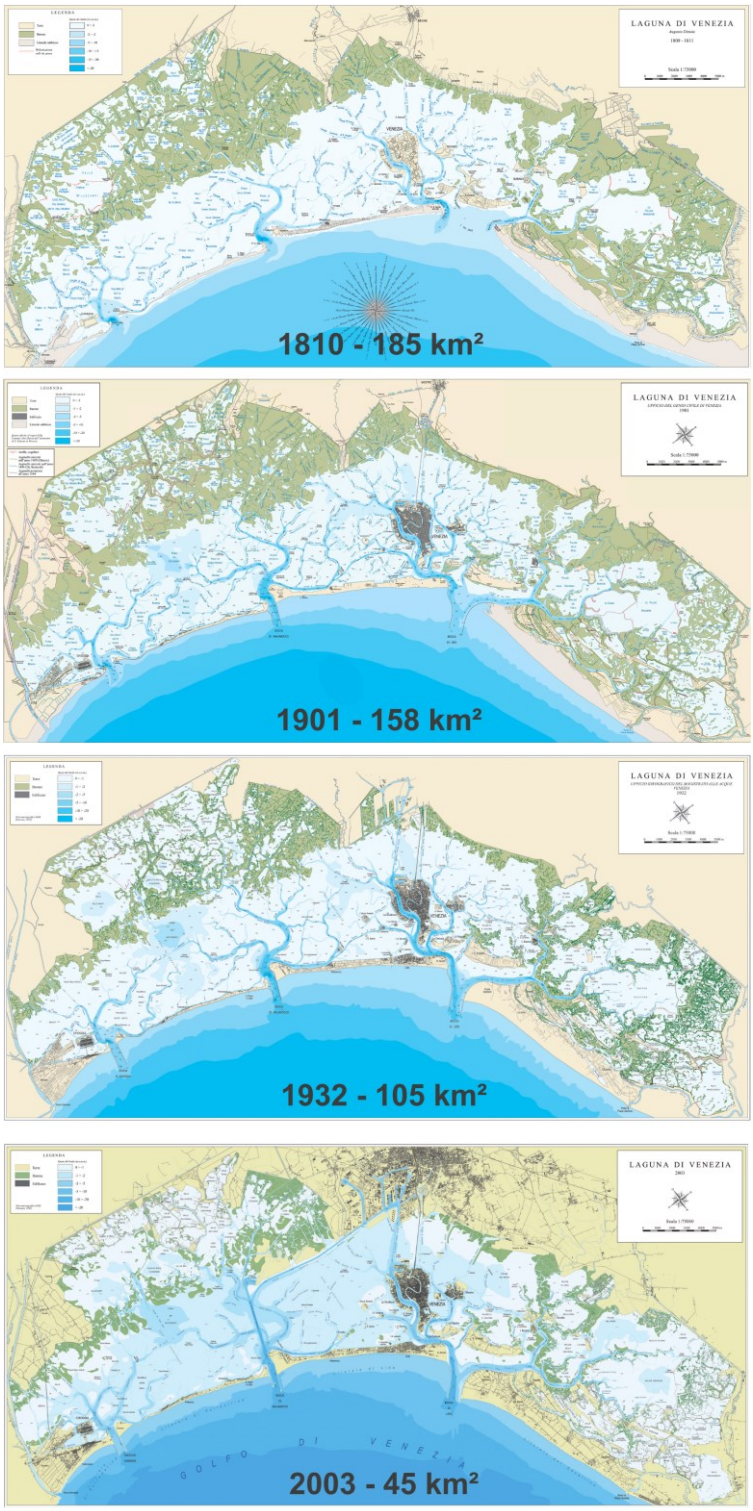

Figure 1.2. Evolution from 1810 to 2003 of natural salt marshes in the Venice Lagoon (Magistrato delle Acqua di Venezia).

1.1. Salt marshes characteristics

As above-mentioned, salt marshes are a typical morphological soil bodies of the Venice Lagoon, but also of other lagoons around the world and of ECEs as well. Salt marshes are landforms whose elevation is higher than mean sea level, therefore they are generally above the water level but flooded during high tides that occur twice a day in Venice, since the tide is semi diurnal. Hence, salt marshes are characterized by **strong fluctuations** in salinity, temperature and submersion and this makes them an even more unique environment.

The salt marsh elevation above mean sea level is typically between 20 and 50 cm, hence, salt marshes are populated by **halophytic vegetation**. Examples of halophytic vegetation include Spartina, Salicornia, Limmoniu, Sarcocornia, Juncus (Figure 1.3). Halophytes can withstand periodic flooding by salt water but cannot thrive if the salty water level is constantly too high: salt marshes suvivance is linked to their elevation on sea level. This is also due to the fact that plants, which cannot bear a too high sea-water table,

- strengthen the soil structure,
- trap sediments,
- reduce erosion and
- slow down water run off.

Therefore, **long-term survival** of salt marshes will depend on their ability to keep pace with the relative sea level rise that has increased to around 4-5 mm/y in the Venice Lagoon (20 years average). This rising is due to climate change effects, such as: ice melting and water thermal expansion, and land subsidence which today is mainly caused by natural consolidation of the Quaternary deposits forming the Northern Adriatic basin.

To maintain their elevation in relation to the rising sea level and mitigate erosion, salt marshes **accrue sediments** thanks to tides and storm surges which carry

inorganic sediments from channels, called “ghebi” in the Venice Lagoon, and tidal flats onto them (Figure 1.3). These sediments are both inorganic (e.g., sand, silt, clays) and organic (i.e., the organic matter produced by plants) (geoscienze.unipt.it, 2022).

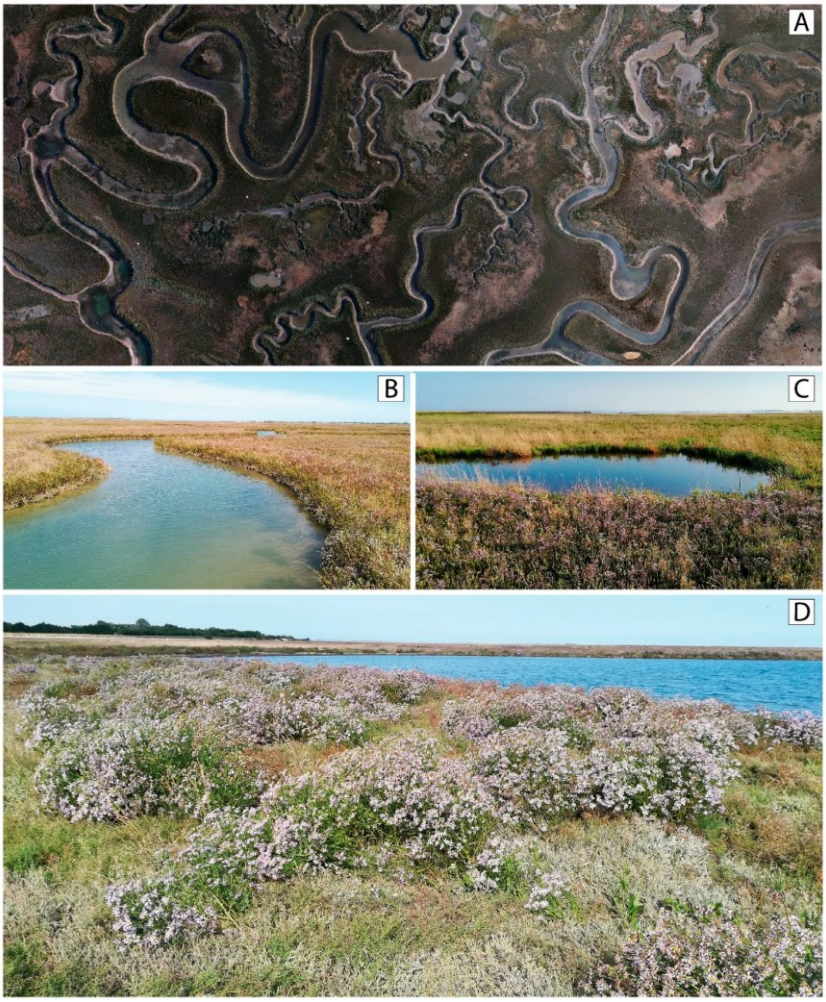

Figure 1.3. Biogeomorphic patterns in the Venice Lagoon.
*(**A**) Tidal channel network cutting through the San Felice salt marsh (Norther Venice Lagoon), providing an example of morphological diversity that is associated to biogeomorphic patterns. The channel network structure influences the distribution of marsh elevations that, in turn, controls vegetation distribution. (**B**) Detail of a tidal channel meandering through the San Felice salt marsh. (**C**,**D**) zonation patterns in the Conche salt marsh (Southern Venice Lagoon), a mosaic of extensive, rather uniform vegetation patches, exhibiting sharp transitions associated to small topographic gradients. Salt marshes are characterized by large biodiversity in terms of, e.g., different vegetation species (Limonium narbonense, Salicornia veneta, Sarcocornia fruticosa, Puccinellia palustris, and Aster tripolium, in the photographs, courtesy of Alice Puppin and Davide Tognin).*

1.2. Venice Lagoon salt marshes typology and classification

Salt marshes are dynamic ecosystems that have evolved over time in response to changing environmental conditions. Understanding the different types of salt marshes is essential for their conservation and management. Their classification is based on their formation processes and location within the lagoon and their characteristics vary depending on their formation processes and evolutionary history.

There are several types of salt marshes (Figure 1.4), each with distinct features:

- **Lagoon-edge salt marshes:** Some salt marshes are what remains of the emerged part of the coastal plain and are so saturated with brackish water that only halophytes plants can survive. They are often found along the lagoon edge towards the mainland.
- **Internal Area salt marshes:** These salt marshes have a more complex history. Initially submerged in saltwater, they later became freshwater marshes, and peat bogs due to river inflows. After river courses were diverted, they reverted to lagoon conditions. They are primarily found in the southern lagoon.
- **Salt marshes at the Sides of Ancient River Inflows:** Formed by ancient alluvial deposits, these salt marshes are often found near the former mouths of rivers.
- **Salt marshes at the Edges of Lagoon Channels:** Created by sediments transported by marine currents and deposited at the edges of lagoon channels, these salt marshes are often found in the northern lagoon.
- **Paleo-salt marshes:** These are ancient salt marshes whose emergence is evidenced by traces of oxidation and plant remains. Their formation was caused by a drop in sea level.

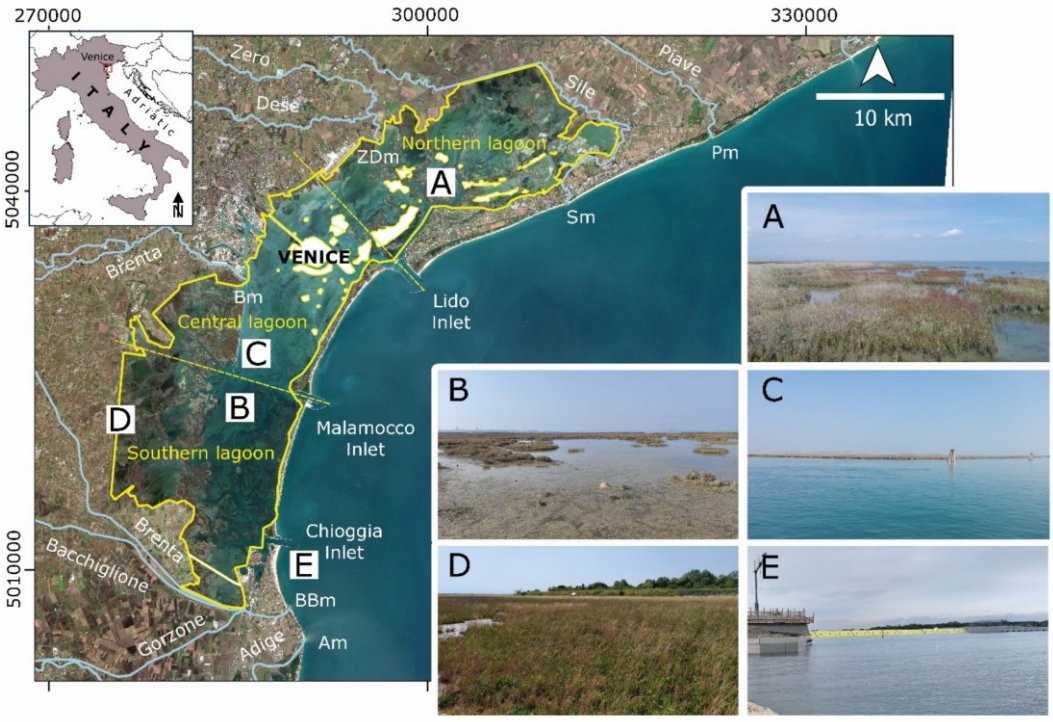

Figure 1.4. Figure 1.4. Typical morphologies in the Venice Lagoon and M.o.S.E. barriers.
The photos on the right show typical (A) salt marsh, (B) tidal flat, (C) subtidal flat morphologies, (D) the embankments bordering the lagoon margin, (E) the Mo.S.E. mobile barriers. Coordinate system: EPSG 32633 (Tosi 2024).

1.3. Habitat

Salt marshes thrive in fine sediments, while halophytes plants favor sandy soils. In salt marshes, both **plant roots and fungi** contribute to soil structure, creating pores and promoting bioturbation. Microorganisms like algae and cyanobacteria help stabilize the soil surface through biofilm formation, reducing erosion and adding organic matter. High organic content and moisture in these environments often lead to low oxygen levels, especially in lower intertidal areas. Salt marshes are typically rich in sulfur-forming sulfides, which impact soil color, odor, and plant growth. Flooding regimes in intermittent areas can further limit plant diversity, favoring only the most resistant species (Zedler 2017).

These environments also support fish habitats and a huge bird population.

Figure 1.5. Typical vegetation of a salt marsh in the Venice Lagoon.
1) Spartina stricta, 2) Artemisia caerulescens, 3) Inula Crithmoides, 4) Arthrocnemum fruticosum, 5) Sueda marittima, 6) Juncus maritimus, 7) Salicornia, 8) Juncus acutus, 9) Puccinellia palustris, 10) Limonium serotinum (Meneghini, 2022).

1.4. Ecosystem services

Generally speaking, salt marshes are densely populated and vegetated areas within transitional environments (Barbier et al. 2011). These ecosystems play crucial roles in :

- **Carbon sequestration:** absorbing and storing carbon dioxide from the atmosphere;
- **Raw materials and food provision:** generate biological productivity and diversity;
- **Sediment trapping:** capturing and retaining sediments.
- **Coastal protection:** wave attenuation and and/or dissipation reducing erosion;

- **Erosion control:** capturing and retaining sediments, stabilizing and soil retention in vegetation root structures;
- **Nutrient cycling:** regulating nutrient flows between land and sea;
- **Habitat provision:** supporting a diverse range of plants and animals;
- **Water purification:** provides nutrient and pollution uptake, as well as retention, particle deposition;
- **Recreation, tourism, education:** provides unique and aesthetic landscape, suitable habitat for diverse fauna and flora**.**

1.4.1. Carbon sequestration

Salt marshes store huge amount of carbon in both living plant material and soil. Carbon sources include marsh plants, algae, bacteria, and organic matter from surrounding areas. As marshes grow vertically with rising sea levels, more **carbon is buried in the soil**. Some of this buried carbon is **permanently stored**, while the rest is eventually released through microbial decomposition. Carbon storage refers to the total amount of carbon accumulated in the marsh, including both buried and sequestered carbon (Figure 1.6 and Figure 1.7).

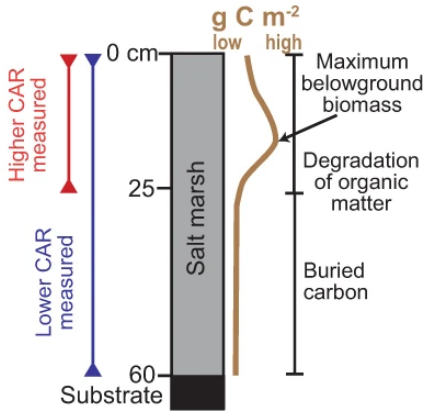

Figure 1.6. Higher and lower carbon accumulation rates that result from integrating over short (0–25 cm) and long (0–60 cm) intervals and associated time scales, respectively (Miller et al. 2022).

Figure 1.7. Greater carbon removal and storage of salt marhses and mangroves (coast.noaa.gov).

1.5. Major factors compromising salt marshes

The construction of jetties and coastal defend systems, land subsidence, and rising sea level in the Venetian Lagoon led to a shift in tidal flows, favoring the **export of fine sediments and preventing the import of new sediments**. This imbalance, combined with **reduced sediment input from rivers**, caused a decline in salt marsh coverage. As a result, increased wind exposure led to **larger waves**, which further eroded salt marshes and mudflats. This cycle of erosion and deepening mudflats created a **negative feedback loop**, exacerbating the loss of these valuable ecosystems (Figure 1.8) (Finotello et al. 2023).

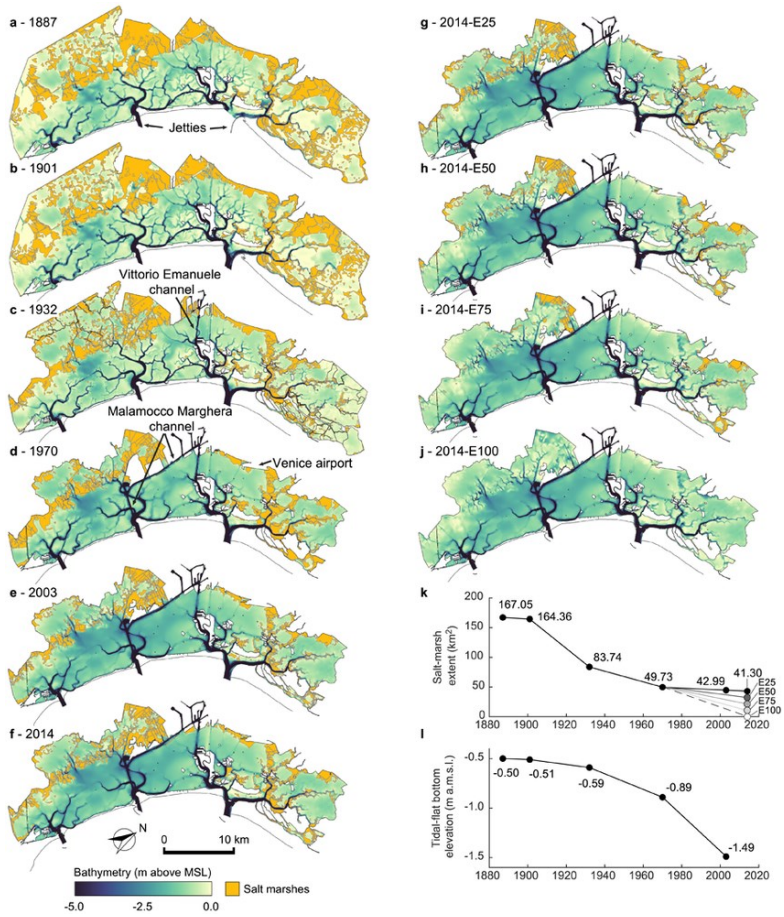

Figure 1.8. Morphological evolution of the Venice Lagoon.
Bathymetry of the Venice Lagoon in 1887 (a), 1901 (b), 1932 (c), 1970 (d), 2003 (e), and 2014 (f), as reconstructed from available historical topographic and bathymetric data. (g, h, i, j) Morphology of the Venice Lagoon according to the hypothetical scenarios of marsh erosion analyzed in the above cited study. These scenarios assume different rates of marsh erosion equal to 25% (2014-E25), 50% (2014-E50), 75% (2014-E75), and 100% (2014-E100), respectively. Temporal variation of salt-marsh extent (k) and spatially-averaged bottom elevation of tidal flats (l) between 1887 and 2014 are also shown.

1.5.1. Subsidence and mean sea level rise

Three major factors responsible for the relative land settlement occurred in the Venice lagoon area over the XX century:

1. the **anthropogenic geomechanical subsidence**, induced by groundwater over-exploitation,
2. the **geological subsidence**, and
3. the **eustatic sea level rise** (i.e., rise in sea level caused by climate change).

Cumulatively, thet have caused a loss of elevation for Venice amounting to 23 cm with respect to the m.s.l. (Figure 1.9).

Other more specific causes deeply studied over the last years are:

1. land sinking due to the expected gas production from the Chioggia-Mare reservoir, but the development project is to date shelved despite the reassuring results obtained by a modeling analysis, and
2. geochemical subsidence due to peat oxidation and salinisation of clayey sediments taking place in the southern catchment of the Venice lagoon ("Land Subsidence in the Venetian Area: Known and Recent Aspects" 2005).

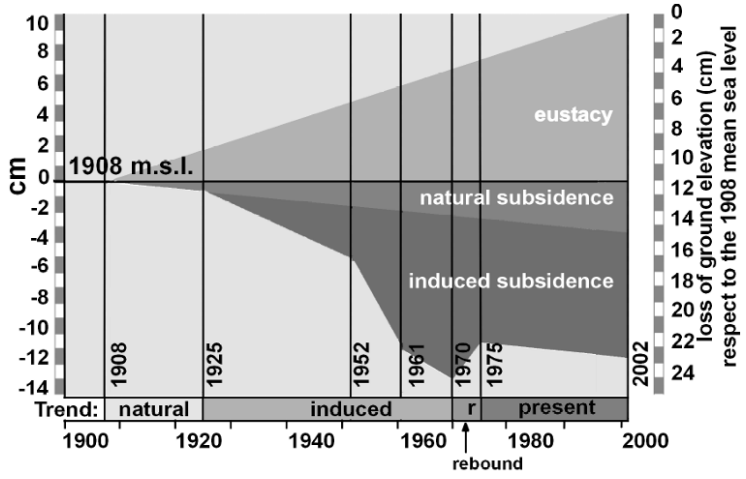

Figure 1.9. Graphical representation of the three components of the relative ground elevation loss at Venice consisting of about 3 cm of natural subsidence, 9 cm of anthropogenic subsidence, and 11 cm of sea level rise ("Land Subsidence in the Venetian Area: Known and Recent Aspects" 2005).

This contributes to the flattening and deepening of the lagoon topography and thus to the loss of lagoon landscape diversity, likely leading to a decrease in the ecosystem services the tidal morphologies provide (Figure 1.10).

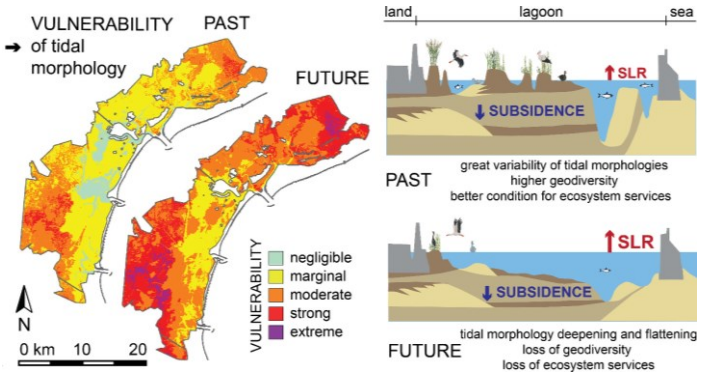

Figure 1.10. Vulnerability of Venice Lagoon to the differential land sinking (Tosi 2024).

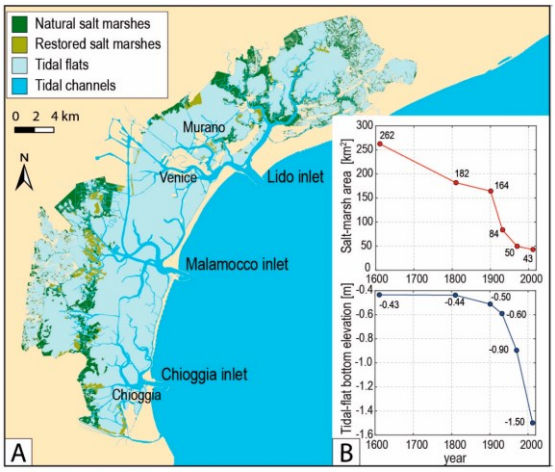

Figure 1.11. (A) The Venice Lagoon and its main morphological features:salt marshes, tidal flats, and tidal channels.
(B) Temporal evolution of salt-marsh area (top) and of tidal-flat bottom elevations(referenced to mean sea level) between 1600 and today (D'Alpaos and D'Alpaos 2021).

Figure 1.11 (B) clearly shows how strongly the how the displacement of the tidal-bottom elevation affected the total saltmarsh area in the Venice Lagoon: the accelerated deepening of the lagoon bottom between 1900 and 2000 was concomitant to an abrupt loss of saltmarsh area.

1.5.2. Human coast protection interventions

Sediments delivered cyclically at high tides and during surges, along with organic matter produced by vegetation, ensure that wetlands grow vertically to keep pace with a small rate of SLR. Today, however, many coastal systems around the world suffer from a lack of sediment input ((Tosi 2024) and the Venice Lagoon is not an

exception. For more than a thousand years, Venetians carried out **hydraulic works** to preserve the strategic role of their lagoon for economic and safety purposes. They diverted large rivers out of the lagoon to avoid siltation (i.e., process where river water deposits silt into reservoirs, leading to environmental issues such as reduced water storage capacity), built large sea walls called Murazzi, modified the inlets, and dug new deep canals (D'Alpaos, 2010; Silvestri et al., 2018). The sediment supply from the rivers has decreased. Hence, the Venice Lagoon is characterized by negligible riverine and marine sediment inputs. Therefore, its morphological evolution is primarily driven by the redistribution of sediment resuspended from within the lagoon (Tognin et al. 2021).

The construction of jetties and rising sea levels in the Venetian Lagoon led to a **shift in tidal flows**, favoring the export of fine sediments and preventing the import of new sediment. This imbalance, combined with reduced sediment input from rivers, caused a decline in salt marsh coverage. As a result, increased wind exposure led to larger waves, which further eroded salt marshes and mudflats. Once more, this cycle of erosion and deepening mudflats created a negative feedback loop, exacerbating the loss of these valuable ecosystems.

Coming to recent times, the Mo.S.E. (acronym for “Modulo Sperimentale Elettromeccanico”, Electromechanical, Experimental Electromecanical MOdule) system (Figure 1.12), designed to shield Venice from Adriatic Sea floods, paradoxically harms the marshes.

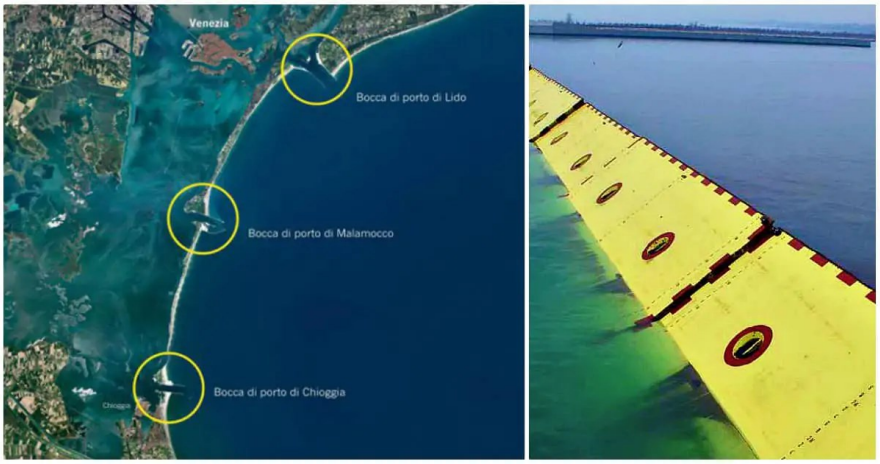

Figure 1.12. Position of the Mo.S.E. floodgates in the Venice Lagoon's and the raised floodgates when the system is active.

By blocking storm surges, it prevents the delivery of sediment that is vital for most of the salt-marsh sedimentation (more than 70% in this case), contributing to the dramatic retreat of the marshes (Figure 1.13) (Marsh resilience to sea-level rise reduced by storm-surge barriers in the Venice Lagoon).

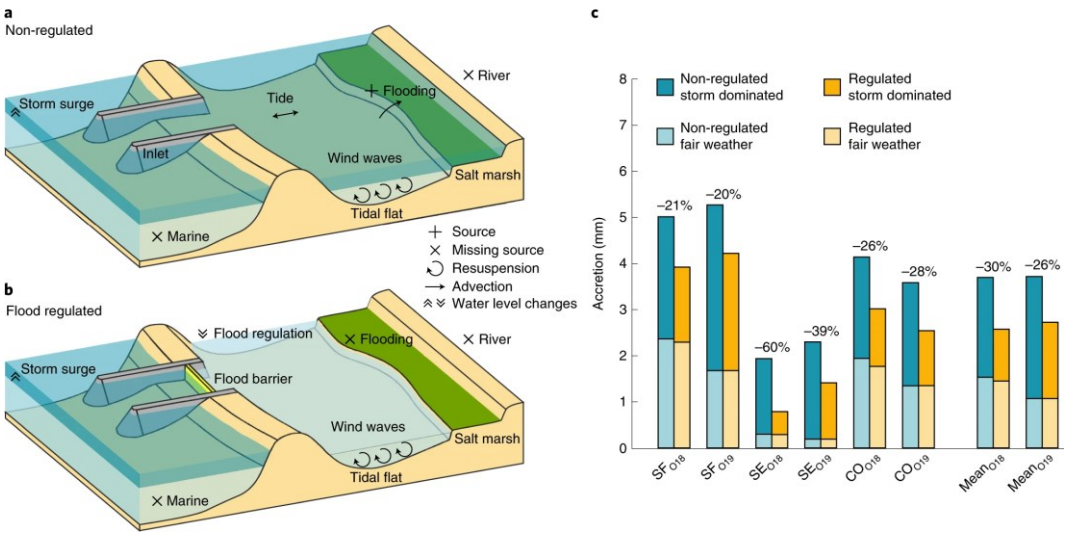

Figure 1.13. Sedimentation changes in the flood-regulated scenario.
***a)**, **b)** Sediment dynamics in a non-regulated (**a**) and flood-regulated (**b**) system. **c)** Change in accretion between the non-regulated (teal bars) and regulated scenario (yellow bars). Categories refer to the study areas (SF, SE and CO) or their mean. Subscripts indicate the beginning of the grouping period: O18, from October 2018 to October 2019, O19, from October 2019 to October 2020. Percentages indicate the relative change in the flood-regulated scenario with respect to the non-regulated one (Tognin et al. 2021).*

The first 15 closures of the mobile floodgates operated between October 2020 and January 2021 contributed to a 12% reduction in marsh deposition, simultaneously promoting a generalized channel infilling (Figure 1.14) (Loss of geomorphic diversity in shallow tidal embayments promoted by storm-surge barriers, tognin et al).

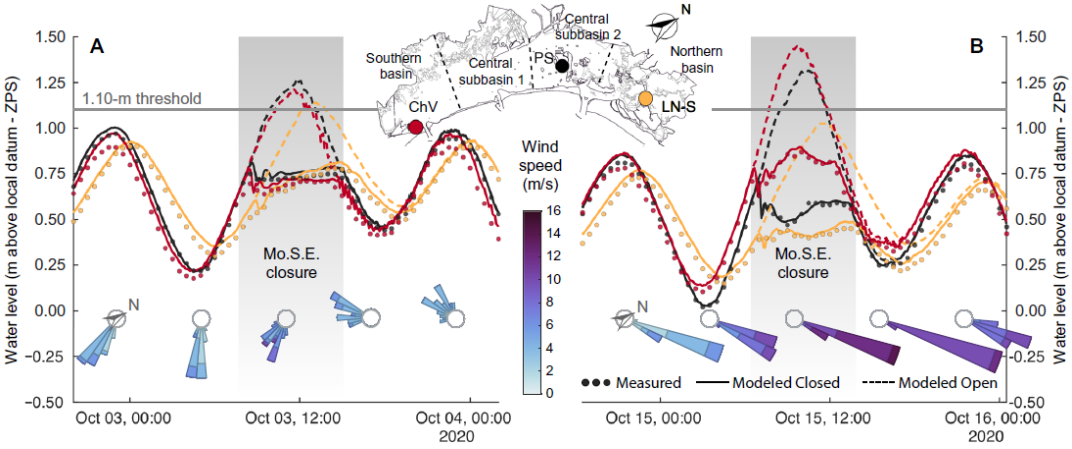

Figure 1.14. Effect of floodgate closure on the lagoon hydrodynamics.
*Water level and wind conditions for the 3 October (**A**) and 15 October 2020 (**B**) events. Solid circles represent water level measurements in three different stations [Punta della Salute (PS), Laguna Nord–Saline (LN-S), and Chioggia Vigo (ChV)] represented in the inset, and solid and dashed lines represent water levels modeled in closed and open barrier scenarios, respectively. Wind roses show wind conditions grouped by 6-hour-long intervals and measured in the Laguna Nord–Saline station. Gray background indicates the time span of Mo.S.E. closures (Loss of geomorphic diversity in shallow tidal embayments promoted by storm-surge barriers, Tognin et al. 2021).*

2. INVESTIGATION SITE AND CONTEXT

The future of low-lying tidal landscapes will largely depend on how quickly recently deposited soils compact. Recent findings suggest that sedimentation rates need to double to offset the expected rise in sea levels (Zoccarato and Da Lio 2021). To restore salt marsh areas in the Venice Lagoon and slow down the loss of them, several initiatives have been carried out at different levels.

2.1. Salt marshes restoration projects in Venice Lagoon

The present thesis contributes to a project driven by the NGO We Are Here Venice (WaHV) ETS. WaHV is conducting the VITAL research project aimed at investigating whether artificial mudflats can be turned back into the marshes that once thrived in the area and become a functioning part of the lagoon ecosystem again (Figure 2.1).

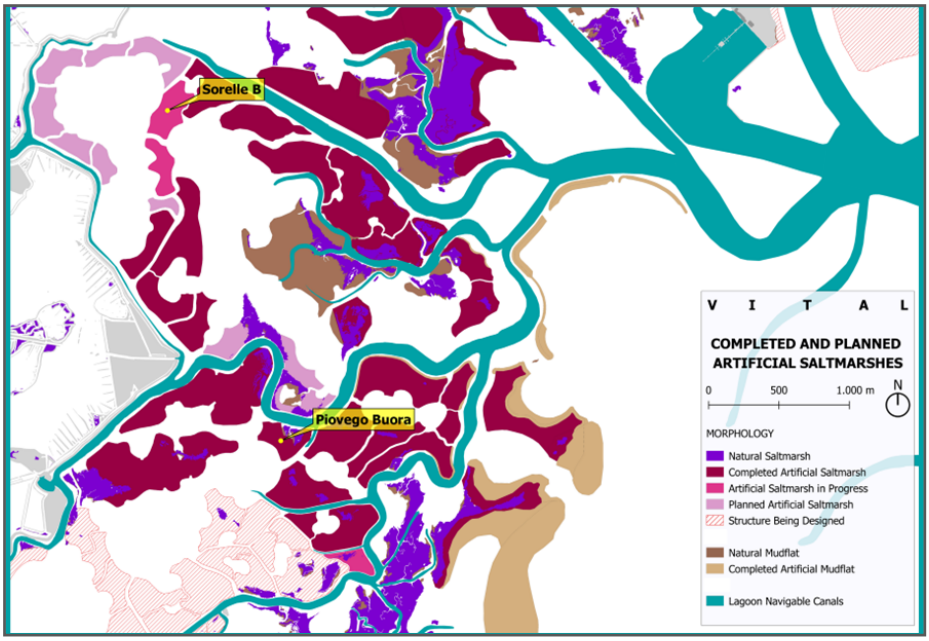

Figure 2.1. Completed and planned artificial salt marshes in the central portion of the Venice Lagoon where the VITAL project is ongoing. The evolution of the Piovego Buora and Le SorelleB artificial salt marshes have been monitored within VITAL (Zoccarato, 2023).

The Decree 22 May 2023, No. 86 of the Italian goverment provides a framework for the **management of sediments** within the Venetian Lagoon. It establishes the criteria for granting permits for sediment movement, exempts certain sediment activities from waste classification, and mandates compliance with environmental impact assessment procedures. Additionally, it requires adherence to guidelines for sediment management and environmental quality standards to protect the lagoon ecosystem.

Restoration of natural salt marshes or construction of artificial marshes requires the following steps:

1. **Construction of retaining structures for sediment containment:**

   This is especially needed when a fluid sediment-water mix is discharged and where the aim for this pumped sediment is to remain in place following disposal, such as to raise the level of a marsh or form a new marsh. In this situation, the relatively fluid sediment will need time to settle, dewater and

stabilize, which can be further supported following colonization of the material. There are several different sediment retention structures that can been used. A most used method is the realization of retention walls made by adjacent wooden poles inserted in the lagoon subsoil and covered by geotextile to contain the sediment while allowing water exchange (Figure 2.2).

Figure 2.2. Wooden poles and geotextile sheets as containment structure for a salt marsh restoration project.

2. **Dredged sediments placement:**

   The nourishment is carried out using sediments dredged from shallows or nearby channels. The disposal can be carried out with various methods, such as bottom placement, mechanical placement, and hydraulic pumping via pipeline. With this latter case, sediment is pumped through a pipeline from an appropriately equipped dredging vessel to the receiving disposal site. In this approach, the material is mixed with water, either through the dredging process itself or within the hopper (Figure 2.3).

Figure 2.3. Disposal of dredged soil and water mixture at Le Sorelle-B via pipeline and hydraulic pumping.

3. **Protection of salt marsh edges and sediments traps:**

   Various types of revetments (i.e., structures that protect against erosion) can also be strategically placed to disperse wave energy and act as a sediment trap so that, over time, salt marsh plants may colonize the sediment (Figure 2.4). Brushwood structures is one option. Rock rolls (tubes of strong mesh filled with stones) or rock mattresses can form a more permanent option, and coir rolls can also encourage salt marsh vegetation to settle and colonize. When the wave motion is reduced, salt marsh receives a higher sedimentation rate. The sediments removed from the most exposed areas and transported in suspension by the tidal currents are here deposited. Therefore, it is possible to create areas in which sedimentation is favored near the perimeter of an eroding salt marsh by installing devices capable of reducing the turbulence of the water but at the same time are permeable to the sediments themselves (Cecconi, 1995). Biodegradable materials are preferable. Generally, the product is estimated to disintegrate in around 10 to 30 years (depending on temperature and light levels), when it is expected that salt marsh plants will become sufficiently established to continue trapping the sediments and colonize any remaining unvegetated areas.

Figure 2.4. Salt marsh edges protection structures and sediments trap.
A) Brush Fascine Boxes are used 300 metres out into a salt marsh to encourage sedimentation, Rumney Marsh, South Wales, UK; B) Coir logs are being tested as possible backstop against erosion in Sengekontacket Pond; C) Brushwood fences to capture sediments transported by water in the Venice Lagoon. The brushwood bundles are positioned between two wooden pole alignments and fixed with a rope to them.

2.2. Signs of salt marshes restoration project effectiveness

Some artificial salt marshes created years ago in the Venice Lagoon have very little vegetation and are vulnerable to erosion or already eroded whereas other areas that were filled in above the typical elevation (relative to average water level) have been vegetated by plant species more typical of islands than intertidal zones. Moreover, artificial marshes frequently lack channels – a key feature of marsh topography, that allows correlations with water dynamics, vegetation cover, and other parameters that are closely associated with ecological functionality.

The aim of the thesis is to prove the effectiveness of a numerical model to forecast the compaction and autocompaction phenomena during and after the artificial salt marsh restoration. This could constitute a key tool in the salt marsh restoration or project design and management: it could lead to understanding and predicting the medium and long-term evolution of Le Sorelle-B artificial salt marsh starting from

the entity of artificial nourishment. The importance of proper control of nourishment intensity in a site to be restored or constructed is highlighted by the comparison of two similar sites:

- Le Sorelle-A: in front of Le Sorelle-B artificial salt marsh, a large portion of the artificial marsh built/up in 2017 is permanently submerged (Figure 2.5);

Figure 2.5. Aerial view of Le Sorelle-A (lower part) and Le Sorelle-B (upper part) salt marshes.

- Lago della Pietra: even if the vegetation cover remains more patchy and less biodiverse than on natural marshes, it thrives.

Figure 2.6. view of Lago della Pietra salt marsh.

The main difference between the two above-mentioned artificial salt marshes is the mean surface elevation: the first one is only few decimeters lower than the second

one. A better result on Le Sorelle-A could be achieved by knowing in advance the behaviour of the salt marsh platform during and after.

Apart from this, a pilot site in the central lagoon of Venice, the so-called "Piovego-Buora" artificial salt marsh, gives hope for the future of the reconstruction project: after the **creation of openings in the infill perimeter**, the increased exposure to the energy of the tidal currents, wind and waves has triggered the **spontaneous formation of new channels** (Figure 2.7).

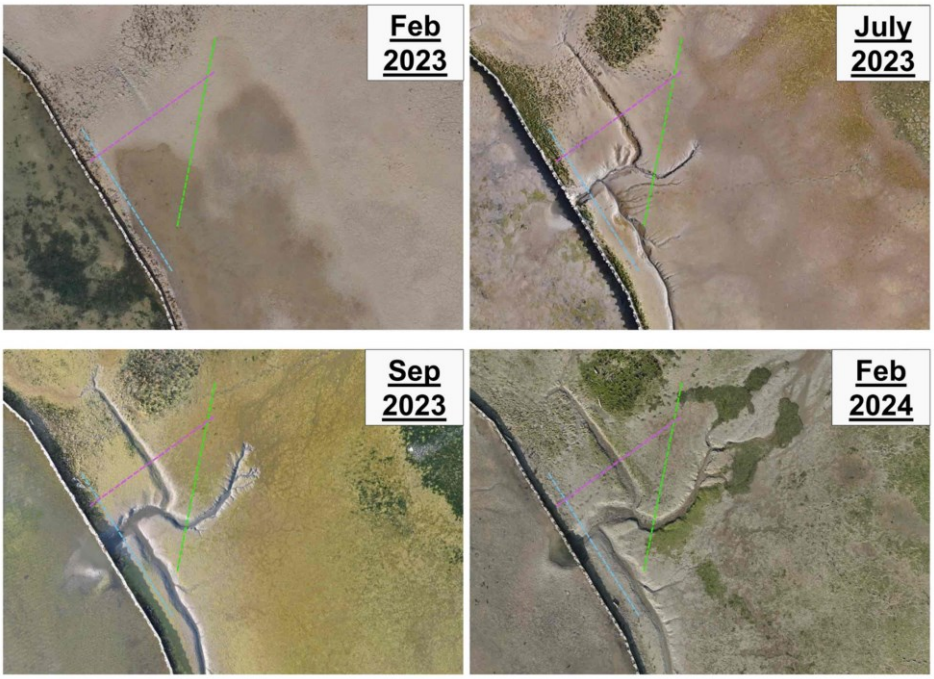

Figure 2.7. Orthophoto from drone of one of the Vital pilot sites, the Piovego-Buora artificial salt marsh, in the central lagoon of Venice. Rework by eng. Alessandro Gasparotto from WaHV.

By connecting to lower inner areas of the infill a large drainage system is now developing as well. Even if the processes need time and the dynamics can produce unexpected outcomes, this is expected to enhance the above-mentioned ecological functionality of the artificial salt marsh (v-i-t-a-l.org).

2.3. Description and evolution over time of Le Sorelle-B site

Le Sorelle-B site is located in the central basin of the Venice Lagoon, approximately 14.5 km south-west of the Venice city center. The site is in the Campagna Lupia municipality and it can only be reached by boat through the Canale Novissimo del Cornio.

Le Sorelle-B includes around 62.230 m^2 and its perimeter extends to 1.130 m. The reclaimed area extends around 435 m and 95 m along the Southeast-Northwest and Northwest-Southeast directions, respectively (Figure 2.8).

Figure 2.8. Le Sorelle-B site in the Venice Lagoon.

A large-scale salt marsh restoration project using dredged sediment began in the 1970s. The "Le Sorelle" artificial marshes were part of this effort. While "Le Sorelle-A" was completed in 2016, construction on "Le Sorelle-B" was halted due to a shortage of dredged material (Figure 2.9).

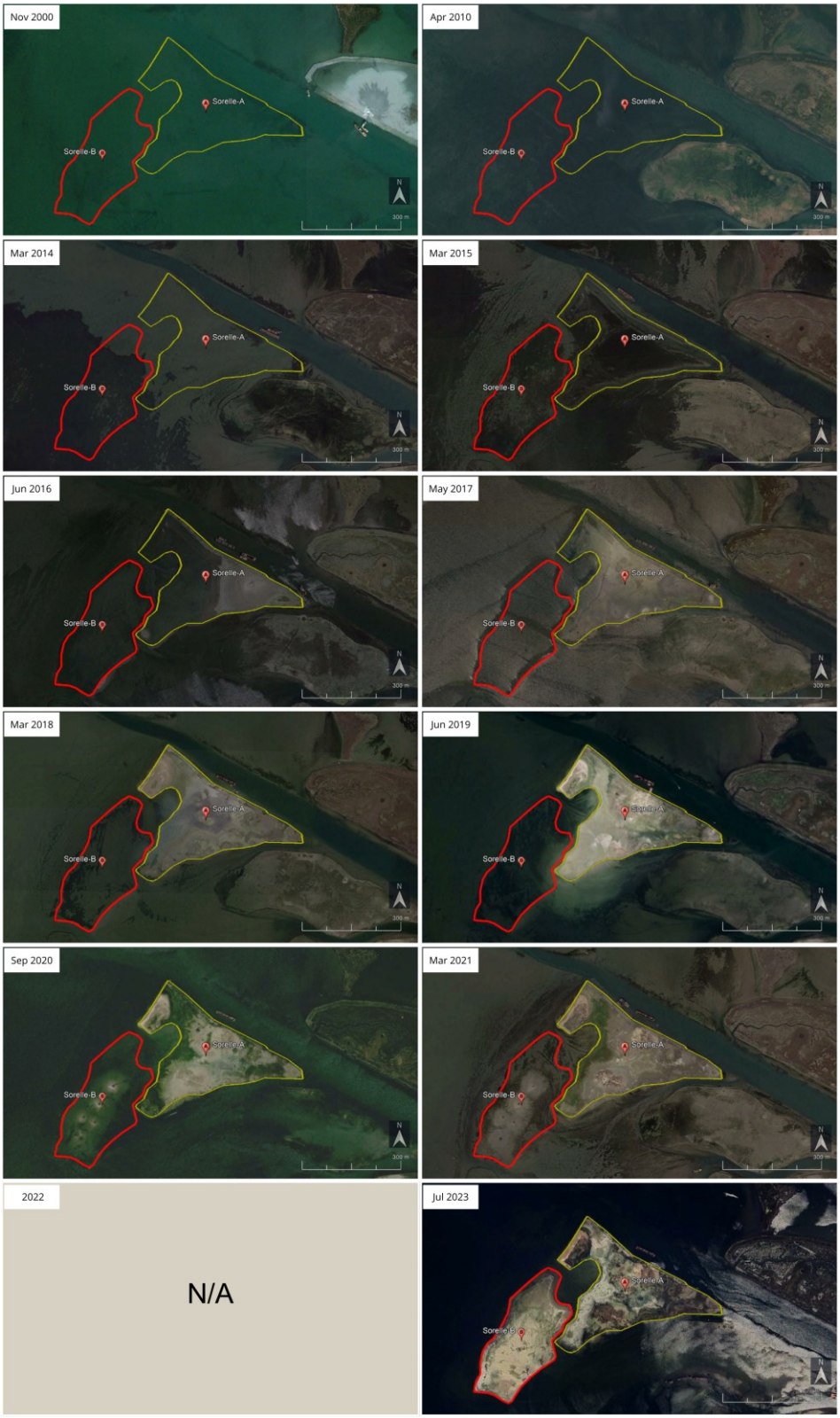

Figure 2.9. Sorelle-A and Le Sorelle-B evolution in time 2010-2023 - Sorelle-B's works started in 2014.

A timeline of nourishments was provided by the Port Autorithy:

1. December 2019 – April 2020: ~ 30.000 m³ sediment deployment in Le Sorelle-B from Malamocco Marghera dredging;
2. August 2021 – October 2021: ~ 22.000 m³ from the same dredging location; operation lasted for ~ 320 h
3. September 2022 – November 2022: ~ 33.000 m³ from "West channel"; operation lasted for ~ 450 h

Regarding the dredger, the pipe diameter is 400 mm. The pump can handle 800 m³ of the mixture per hour, with 200 m³ of that being solid material (Figure 2.10).

Figure 2.10. Disposal of dredged soil and water mixture at Le Sorelle-B site via pipeline and hydraulic pumping.

2.4. Bathymetric surveys

Since 2017, traditional and innovative measures have been carried out on Le Sorelle-B pilot site to collect a significant dataset enabling the development of advanced modeling. As mentioned above, this could constitute a key tool in the salt marsh restoration or project design and management to understand and predict the medium and long-term evolution of Le Sorelle-B artificial salt marsh starting from the amount of artificial nourishment. Hence, Le Sorelle-B has been used as proof of concept to develop an appropriate methodology for the construction of artificial

marshes that can be naturalized and therefore can self-sustain (i.e., keep pace with mean sea level rise) and maintain over time also from an ecological perspective. Surveys of Le Sorelle-B site are periodically carried out to obtain the elevation and geotechnical information necessary to determine the soil elevation evolution and to observe the progress of nourishment with a focus on its sediments autocompaction.

Figure 2.11 shows the bathymetric map of the Le Sorelle-B marsh in September 2021, just before the second nourishment phase, and constitutes the first bathymetry in the records.

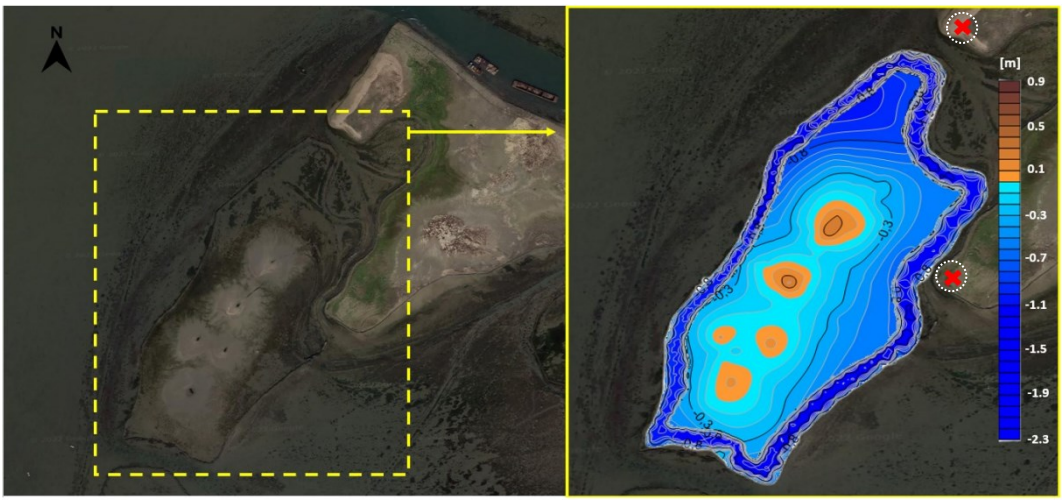

Figure 2.11. Satellite image of Le Sorelle-B salt marsh (left) and the bathymetry (m above msl) in September 2021, before the beginning of the second reclamation phase (Meneghini, 2022).
The red crosses on Le Sorelle-A represents the location of the deep poles used as reference in the topographical surveys.

The map derives from the interpolation of a dataset acquired by topographic measurements using total station and GNSS with two deep benchmarks established in Le Sorelle-A as reference points (red crosses in Figure 2.11). The brown and blue areas correspond to the parts of the bottom of the lagoon above and below the mean sea level (msl), respectively. The brown mounds reach an elevation around +0.30 m above msl and correspond to the areas where sediments were conveyed in the 2019 nourishment. The perimeter zone of the salt marsh reaches -2.3 m below msl representing a sort of canal, dug in summer 2021 to allow a working-ship the positioning of the wall to contain the filling sediments.

To realize the bathymetry map, the dataset was processed through various steps:

- **Georeferencing:** The scattered monitoring points from the topographic survey were georeferenced using AutoCAD.
- **Channel Representation:** Special attention was given to accurately represent the 20-m-wide channel, which represents a discontinuity in the lagoon topography.
- **Data Enhancement:** Additional bathymetric transects and points were manually introduced to improve channel representation using linear interpolation.
- **Gridding:** The updated dataset was processed using Surfer software to create a regular, rectangular grid of interpolated data points (Figure 2.12).
- **Kriging:** The measurements were interpolated by kriging, with a variogram model fitted on the collected dataset.

Table 2-1. Main topological parameter for the model mesh.

	East (EPSG 3003)	**North (EPSG 3003)**
Min (m)	1750309.9	5026673
Max (m)	750972.8	5027467.3
Distance (m)	662.9	794.3

	Spacing between nodes (m)		Number of Nodes
	Min (m)	Max (m)	
East	2	20	134
North	2	20	160

2.5. Soil stratigraphy and radiocarbon age determination

The subsurface of the Venice Lagoon is highly heterogeneous. The formation and the evolution of the lagoon during the last ~ 11.000 – 13.000 years led to the deposition of different types of sediments (peat, silt, clay and sand), that, varying from site to site, testify the different depositional environments occurred over time (v-i-t-a-l.org).

A 10-m core was sampled in the vicinity of the Le Sorelle-B site to characterise the sediments composing the subsurface and the thickness of each stratigraphic unit (Figure 2.13). The continuous core starts from the lagoon bottom (placed at 0.91 m below msl) down to a depth of 10 m.

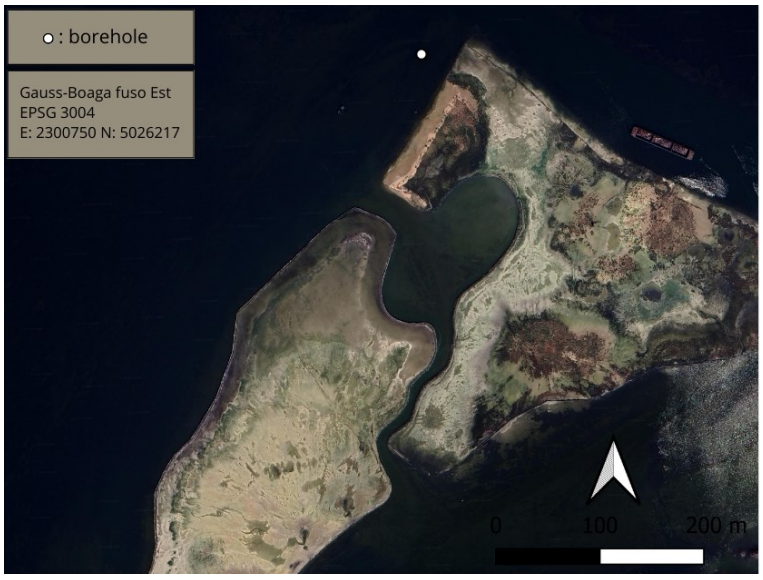

Figure 2.12. Map showing the position of the deep core, drilled to characterize the lithostratigraphic setting of the Venice Lagoon subsoil in the nearby of Le Sorelle artificial marshes.
The borehole coordinates are provided.

The core, which is characterized by a 100-mm diameter, was extruded and placed in ad-hoc **pvc cataloging boxes** consisting of 5 slots of size 1.00 x 0.60 x 0.15 m

(Figure 2.14). Simultaneously, five samples were collected during the coring to be analysed with the C14 radiocarbon dating technique. The borehole was carried out by means of a vibrocorer mounted on a pontoon (Figure 2.14) and using a **Osterberg infixion sampler** suitable for sampling of silt, clay and granular soils of medium-fine grain.

Figure 2.13. The drilling machine used in coring procedure and cataloging boxes at relative depths.
The empty zones indicate the undisturbed specimens collected for the oedometric tests (Meneghini, 2022).

Along with the drilling, on-site geotechnical tests were conducted using a pocket penetrometer and Torvane shear device to assess the compressive and shear strength of cohesive soils encountered during drilling:

- The **pocket penetrometer** measures compressive strength by measuring the force required to penetrate a metal cylinder into the soil;
- The **Torvane shear device** measures undrained shear resistance by rotating a blade within the soil and measuring the required torque.

The so-called "**Caranto**" layer was identified at a depth of -6.906 meters. The Caranto is a stiff, over-consolidated silty or silty-sandy clay layer characteristic of the Venice coastland. Its presence was confirmed by its distinctive color and depth, which aligns with regional geological maps (Figure 2.15).

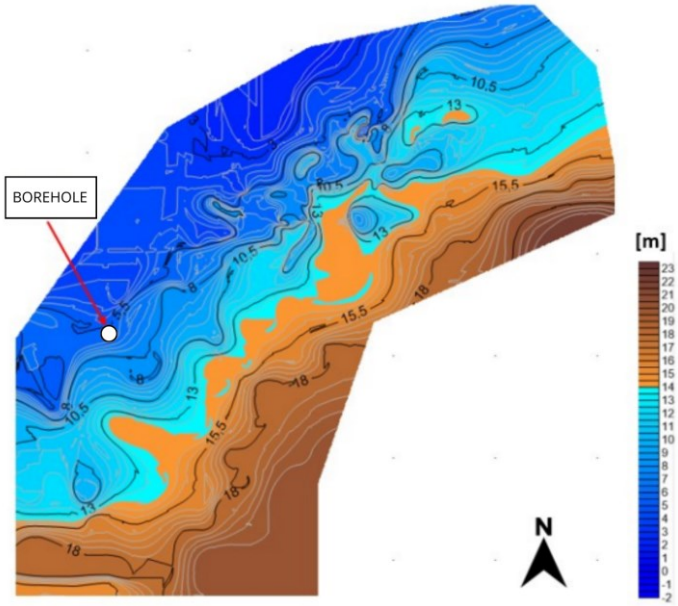

Figure 2.14. Map of the depth of the Holocene base (Meneghini, 2022).
The white dot represent the location of the borehole in the nearby of Le Sorelle-B marsh. The Caranto depth at this location is about 5.72 m, in agreement with the soil stratigraphy obtained from the borehole.

Due to drilling disturbance in the upper meter of the core, a **manual core sample** was taken near the borehole location; the sample revealed a peat layer extending to a depth of 0.73 meters, followed by silty soil (Figure 2.16).

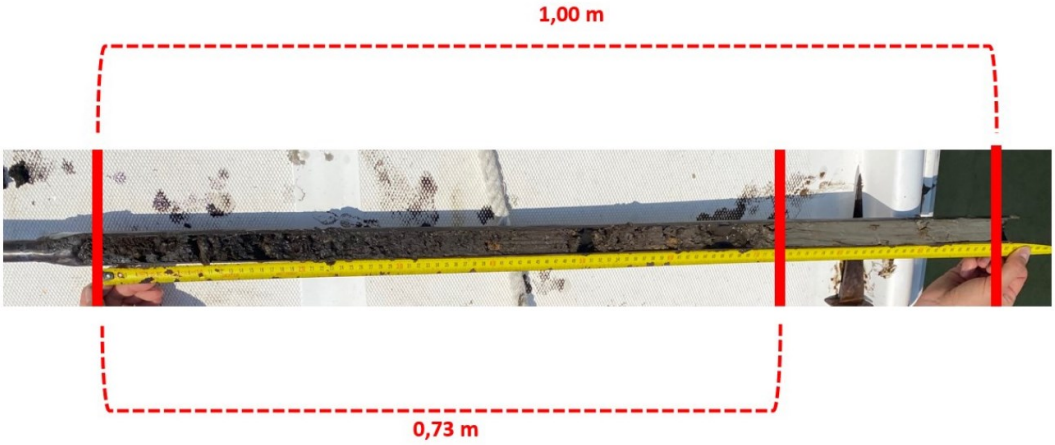

Figure 2.15. Photo of the sample obtained from manual coring in the nearby of the 10-m deep core.
The first 0.73 m part is composed of peat and dark brown organic material. Between 0.73 and 1.00 m the soil changes to greyish clayey silt.

The stratigraphic profile, depicted in Figure 2.17, of the Le Sorelle-B marsh was determined through previous operations and it provide critical input data for the

numerical model. Given the significantly stiffer nature of Pleistocene sediments compared to Holocene deposits, the stratigraphic column analysis is focused on the Holocene layers and the compaction model is developed specifically for these more compressible deposits.

Several soil samples were collected from the core for **radiocarbon dating** to determine the ages of the various soil layers. Organic material samples were taken at the boundaries between these layers.

Radiocarbon dating involves analyzing the concentration of Carbon-14 (C14) relative to stable isotopes Carbon-12 (C12) and Carbon-13 (C13). C14 is formed in the atmosphere and absorbed by plants and animals during their lifetimes. After death, C14 levels decay at a known rate.

Accelerator Mass Spectrometry (AMS) was used to measure C14 levels in the soil samples. The OxCal software, calibrated using the INTCAL database, was employed to convert radiocarbon ages to calendar years.

The results of C14 dating, shown in Figure 2.17, indicate ages ranging from 1930 to 13,630 years before present.

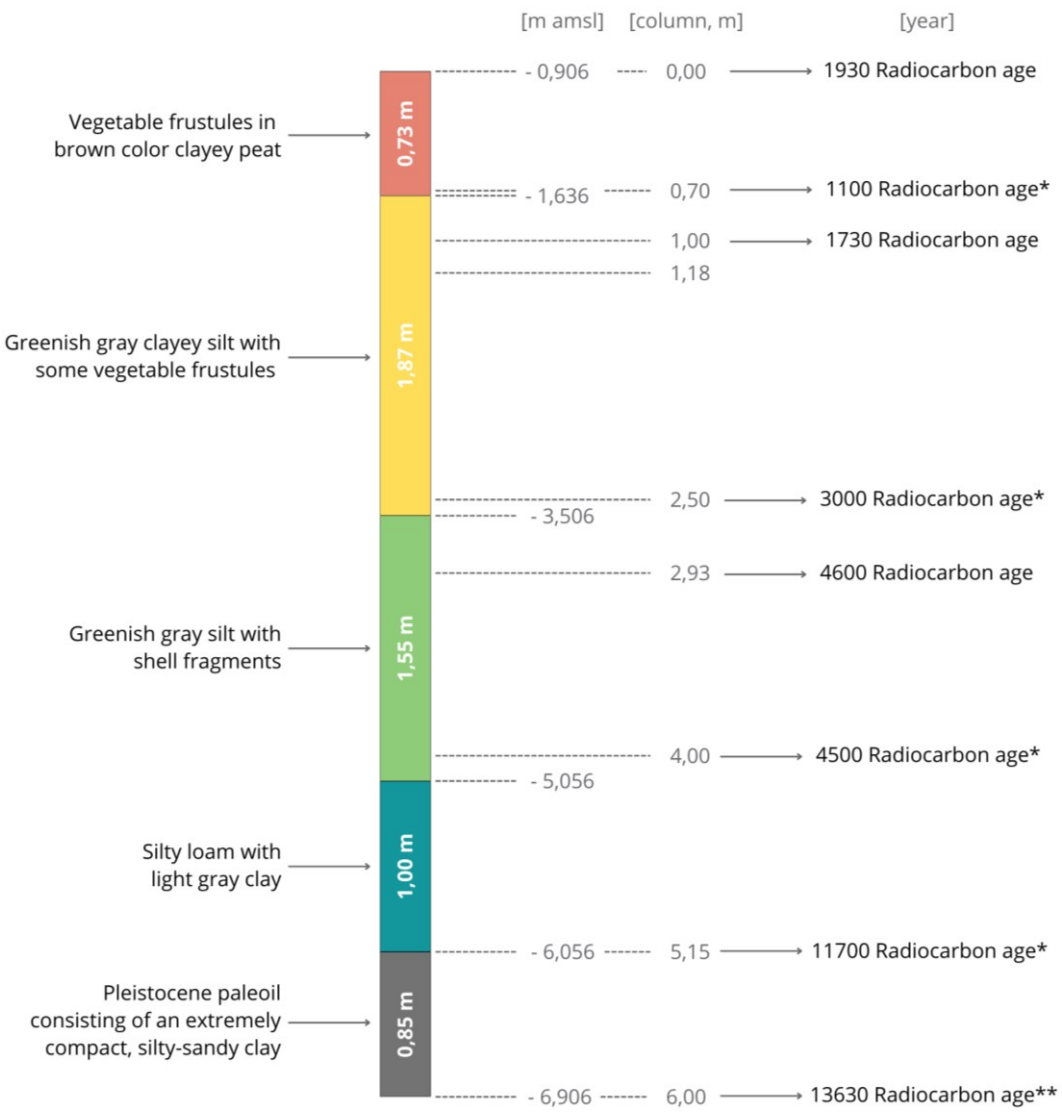

Figure 2.16. Soil stratigraphy at Le Sorelle-B, derived from coring, and Radiocarbon Age (Ra).
From top to bottom the Holocene sequence is made by peat, clayey silt, silty sand, silty loam below which a Pleistocene overconsolidated clay layer is found. Ra is derived from laboratory tests performed by INNOVA ScaRL9; (*) Ra data taken from the literature (Pirazzoli et al., 1981); (**) Ra at depth 6.00 m is obtained by a linear interpolation of the available data.

2.6. Innovative Nourishment Elevation Change (NEC) stations

As already mentioned, a key aspect of marsh restoration design is determining its long-term elevation to ensure ecological functionality and resilience

to sea-level rise. Past restoration projects often failed due to insufficient attention to factors like **sediment autocompaction** and **underlying strata subsidence**. A novel **Nourishment Elevation Change (NEC)** station was developed at the Dept. ICEA of the University of Padova to monitor these dynamics ADDIN ZOTERO_ITEM CSL_CITATION {"citationID":"BkLgqleB","properties":{"formattedCitation":"(Gambolati 1973)","plainCitation":"(Gambolati 1973)","noteIndex":0},"citationItems":[{"id":7,"uris":["http://zotero.org/users/local/D37gJrty/items/93QXV59U"],"itemData":{"id":7,"type":"article-journal","abstract":"A new mathematical derivation of the one-dimensional flow equation in an elastic, saturated, porous medium is presented. The approach involving the consideration of a fixed elemental volume in fixed coordinates is developed by starting from both Lagrangian and Eulerian definitions of the position vector. The confusion existing about these two fundamental points of view has so far led to theoretically erroneous results. The Lagrangian and Eulerian formulations prove to be equivalent and provide the same outcome if they are correctly interpreted and consistently applied. The rigorous equation, compared with Cooper's (1966) equation, turns out to contain an additional nonlinearity resulting from the correct expansion of the partial spatial derivative of the grain velocity. It is also shown that an approach based on a deforming element in fixed coordinates is simple and straightforward, since it does not introduce the grain velocity into the development. However, it needs a particular definition for the compressibility different from the classical one. It is proved that these two compressibilities are not equal; their mathematical link is derived.","container-title":"Water Resources Research","DOI":"10.1029/WR009i004p01022","ISSN":"0043-1397, 1944-7973","issue":"4","journalAbbreviation":"Water Resources Research","language":"en","license":"http://onlinelibrary.wiley.com/termsAndConditions#vor","page":"1022-1028","source":"DOI.org (Crossref)","title":"Equation for one-dimensional vertical flow of groundwater: 1. The Rigorous Theory","title-short":"Equation for one-dimensional vertical flow of

groundwater","volume":"9","author":[{"family":"Gambolati","given":"Giuseppe"}],"issued":{"date-parts":[["1973",8]]}}],"schema":"https://github.com/citation-style-language/schema/raw/master/csl-citation.json"} (Gambolati 1973). NEC station elevation is monitored using a high-precision topographic intersection technique with stable benchmarks as references. Aerial drone photogrammetry is also used to track changes in the distance between the NEC top plate and the marsh platform.

Figure 2.17. Nourishment Elevation Change stations at Le Sorelle-B site.
Left: photo taken by Giulia Meneghetto in the June 2022 inspection, depicting a deep NEC in the Le Sorelle-B site, with annotation regarding the features for topographic features. Right, installing a NEC station, photo by Claudia Zoccarato.

Each NEC station consists of four steel bars embedded in the lagoon bottom (2 m deep) and a central steel pole that can freely move vertically with respect to its specific foundation level (Figure 2.18). There are **two types of NEC** (Figure 2.19) epending on the foundation anchorage: pole's foundation is either on the lagoon bottom (shallow NEC) or an anchor inserted into the subsurface to a depth of interest, 1 m in Le Sorelle-B case, (deep NEC):

- **Shallow NEC** – determines the shallow movement of the lagoon bottom; The foundation consists of a plate resting either on the top of the pristine lagoon bottom;
- **Deep NEC** – measures lagoon subsoil subsidence below 1 m depth; The foundation consists of an anchor inserted into the subsurface to a depth of interest.

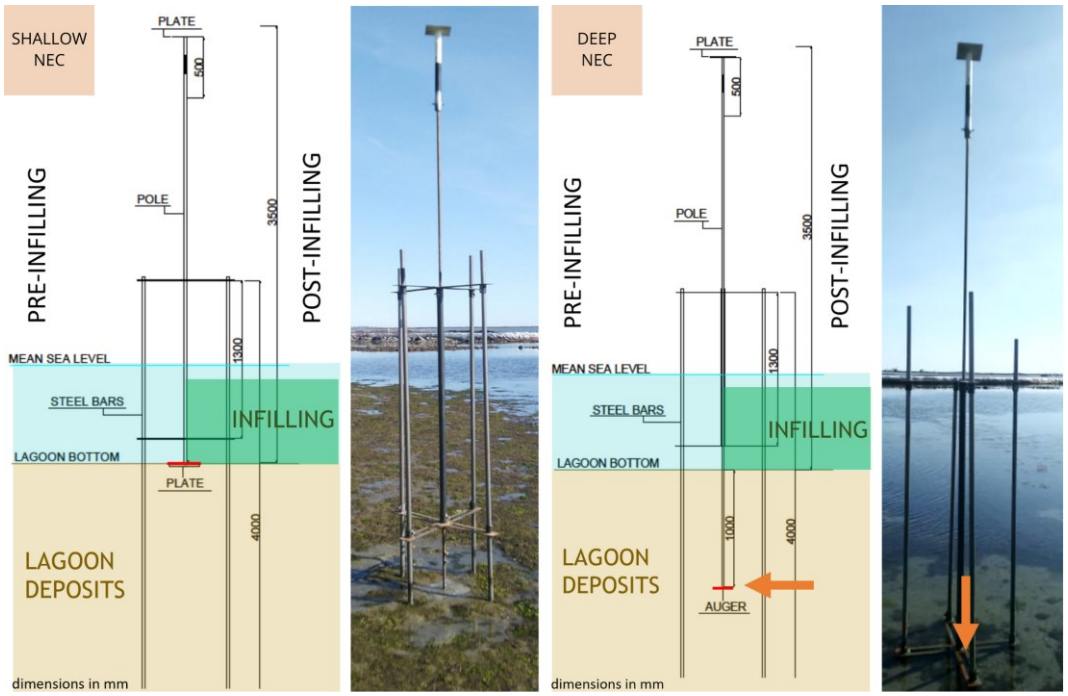

Figure 2.18. Structure of shallow and deep NECs at Le Sorelle-B site.

A network of 10 NEC stations was established in the artificial marsh area before nourishment began. NECs with even numbers are shallow, and those with odd numbers are deep (Figure 2.20).

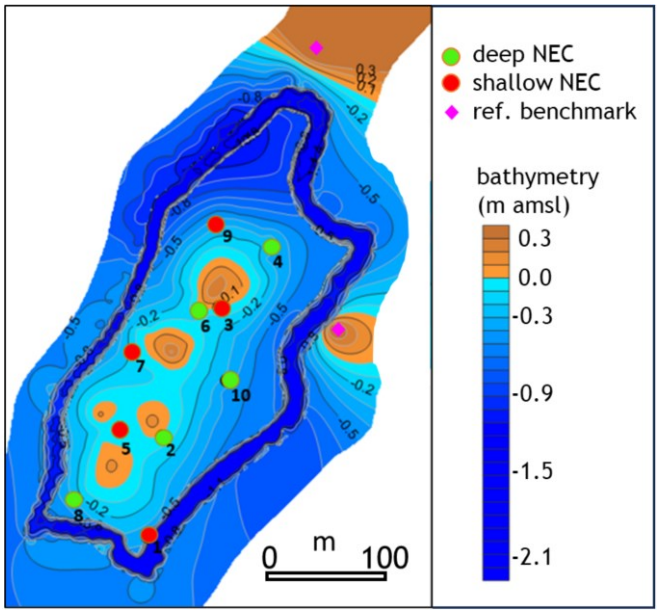

Figure 2.19. Bathymetry map showing the position and number of deep NEC in green and shallow NEC in red (Meneghini, 2022).

Initial measurements have revealed a maximum subsidence of 7 cm in the NEC station closest to the nourishment pipe. The other stations, unaffected by sediment deposition, remained stable. This monitoring system shows promise for quantifying elevation dynamics in newly created artificial marshes. The results are shown in Paragraph 5.2.

Figure 2.21 reports the timeline of interventions and monitoring at Le Sorelle-B site.

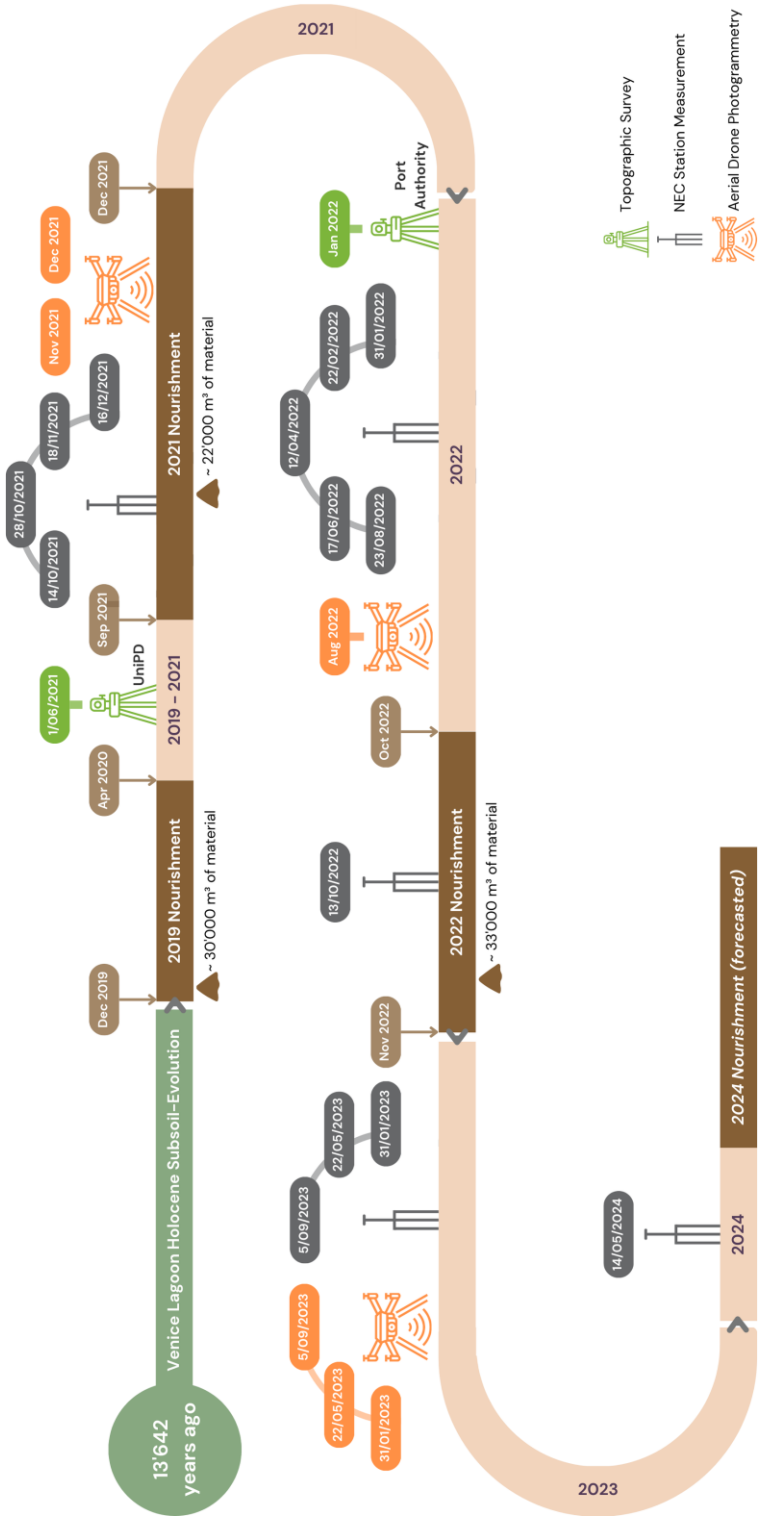

Figure 2.20. Timeline of the interventions and monitoring activities on Le Sorelle-B site.

3. NATSUB3D SIMULATOR

The NATSUB3D is a 3D finite element (FE) simulator developed at the University of Padua and is used to model the evolution of Le Sorelle-B salt marsh. This code simulates sediment compaction, groundwater flow, and landform accretion over time. It employs a 1D geomechanical module based on the Terzaghi approach coupled with a 3D groundwater flow module in the context of large (i.e., not infinitesimal) vertical motion of soil grains (Gambolati 1973a).

The model uses an **adaptive mesh** and considers both deposition and consolidation mechanisms: using a **Lagrangian approach**, the landform evolution is simulated through

A. a deposition mechanism, with the sedimentation rate representing a condition on the upper boundary of the model domain and new elements added on this surface when the amount of sediment exceeds a threshold value (10 cm in the present study); and

B. a consolidation mechanism accounting for soil compaction with node positions updated at each time step.

The geomechanical properties of the soils are characterized by a nonlinear elasto-plastic constitutive model (Xotta et al. 2022).

The size of the time step varies to optimize the computational performance and properly manage sedimentation rates that vary over time and space. Specifically for this study case, the simulator models the whole Holocene evolution of the salt marsh (i.e., 13631 years) till 2015, before any known human intervention. Nourishment on the salt marsh accelerate its evolution, hence a more frequent and controlled maximum time step could be required to get the output prints when there are sudden changes in the salt marsh or specific measures or surveys. This allows

the software to run as fast as possible during past years till human interventions and surveys: from 2015 to 2024. More details in the Paragraph 3.4.

3.1. Governing equations

To accurately model the evolution of sedimentary landforms experiencing substantial compaction (over 5%), vertical grain displacements must be accounted for (Gambolati 1973b)). The successive model by Gambolati (Gambolati 1998) was recently extended to a 2D domain by (C. Zoccarato and Teatini 2017) and then generalized to obtain the governing equation of the groundwater flow in a 3D porous system undergoing large deformations can be as:

$$\nabla \cdot \left(\frac{K}{\gamma} \nabla p\right) = (c_b + \beta\phi)\, Dp - \omega\, c_b\, (1 - \phi_0)\, (\gamma_s - \gamma) \qquad (3.1)$$

Parameters of the Equation (3.1) follow:

- $K = \begin{bmatrix} K_x(\sigma_z) & 0 & 0 \\ 0 & K_y(\sigma_z) & 0 \\ 0 & 0 & K_z(\sigma_z) \end{bmatrix}$ is the hydraulic conductivity tensor

  with the $K_i(\sigma_z)$ are the components along the principal anisotropy direction;
- σ_z is the vertical effective stress;
- p is the incremental pore pressure referenced to hydrostatic condition (i.e., overpressure);
- γ is the specific weight of water;
- γ_s is the specific weight of soil grain;
- c_b is the oedometric compressibility of soil, $c_b = c_b(\sigma_z)$;

- $\phi(\sigma_z)$ is the solid matrix porosity with ϕ_0 the value at the land surface where the vertical stress is negligible, $\phi = \phi(\sigma_z)$;
- β is the volumetric water compressibility;
- ω is the sedimentation rate, defined as mm of soil material deposit in one year;
- D is the Eulerian derivative:

  $Dp = \frac{dp}{dt} + v_{g,z}\frac{\partial p}{\partial z}$, where $v_{g,z}$ is the vertical grain velocity and t the time.

Important to be noticed, the parameters K_x, K_y, K_z, ϕ, and c_b depend on the vertical effective stress σ_z.

The Lagrangian approach (Gambolati 1998) underlies the numerical solution of Equation (3.1), where a dynamic mesh is employed: the grid nodes follow the grains movement caused by consolidation and, as a consequence, FEs deform. The FE discretization approach used to solve Equation (3.1) leads to a system of non-linear ordinary differential equations solved by a back Euler method in time with a fixed-point iteration scheme.

Equation (3.1) is coupled to the consolidation equation which allows to compute the FE deformation due to overpressure dissipation. The latter is due to the accumulation of new sediments on the landform surface. The new sediments cause an increase of the total geostatic load $\Delta\sigma_t$, that can be expressed by the following (Xotta, et al. 2022):

$$\Delta\sigma_t = (1 - \phi_0)\,(\gamma_s - \gamma)\,\omega\,\Delta t \tag{3.2}$$

where Δt is the time interval in wich the sedimentation occurs and ω the sedimentation rate expressed as thickness of new soil per unit of time.

This term is the external factor that determines the variation of the interstitial pressure with respect to the balanced hydrostatic distribution. Then, the correlation

of the pressure variation p associated with the increase in the geostatic load $\Delta\sigma_t$ and the effective vertical stress $\Delta\sigma_z$ is obtained from the well-known Terzaghi principle (Equation 3.3): the response of a soil mass to changes in applied stresses (compressibility and shearing resistance) depend on the effective stresses in that soil mass.

$$\sigma_c = \sigma_z + p \tag{3.3}$$

The Terzaghi's Principle assumes that the soil is assimilated to a set of grain in contact and it's fully saturated. In Figure 3.1 the horizontal section A thought the soil intersecting contact sites may be visualized.

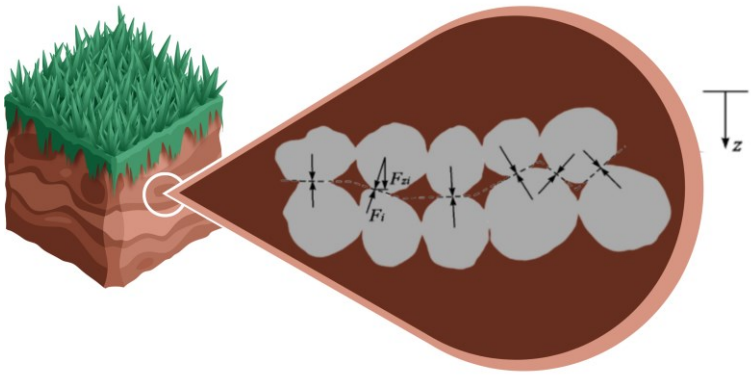

Figure 3.1. Terzaghi's principle.

The vertical component of the stress between two grains, $\sigma_{z,i}$, referred to the horizontal area of contact, A_i , can be expressed as:

$$\sigma_{z,i} = \frac{F_i}{A_i} \tag{3.4}$$

$F_{z,i}$ correspond to the vertical component of the force that the grain exchange i-th contact area. Mathematical steps are used to obtain the effective intergranular stress σ_z for the total section area A:

$$\sigma_z\, A = \sum_{I=1}^{n} \sigma_{z,i}\; A_i \tag{3.5}$$

$$\sigma_z = \frac{\sum_{I=1}^{n} \sigma_{z,i}\; A_i}{A} = \frac{\sum_{I=1}^{n} F_{z,i}}{A} \tag{3.6}$$

where σ_c correspond to the geostatic stress, or the weight of the horizontally unit-rea soil column at a specified depth. Assuming complete saturation and $A = 1$, σ_c is balanced by σ_z and the hydrostatic pressure p according to the equation:

$$\sigma_c = \sigma_z + p \tag{3.3}$$

A variation in the effective stress, $\Delta\sigma_z$, causes a reduction in the thickness of the sil column ℓ, which can be expressed as:

$$\Delta\ell = \alpha\, \ell\, \Delta\sigma_z \tag{3.7}$$

where α is the classical compressibility of the soil and it is related to the bulk compressibility c_b of the soil as follows:

$$c_b = \frac{p\frac{d\alpha}{dp} + \alpha}{1 + \alpha p} \tag{3.8}$$

Therefore, the soil column compaction $u(z,t)$ from 0 to an elevation of z is provided by (Zoccarato, et al., 2017):

$$u(z,t) = -\int_0^z \frac{\alpha(\sigma_z)\,\sigma_z}{1 - \alpha(\sigma_z)\,\sigma_z}\, dz \tag{3.9}$$

3.2. Constitutive relationships

The principle constitutive relationships describing how the main hydro-geomechanical features, that is, compressibility, porosity, and hydraulic conductivity, vary with the effective stress are presented in this paragraph.

Oedometric compressibility (c_b) is a crucial parameter in determining soil consolidation. It varies depending on the type of sediment and can be estimated through laboratory oedometric tests. These tests involve valuating the relationship between changes in void ratio (e) and effective stress (σ_z). c_b can be expressed as follows:

$$c_b = -\frac{1}{\ln 10}\frac{C_c}{(1+e)\,\sigma_z} \tag{3.10}$$

where C_c is the **soil compressibility index**.

C_c can be derived from a graphical interpretation of the laboratory oedometric tests.

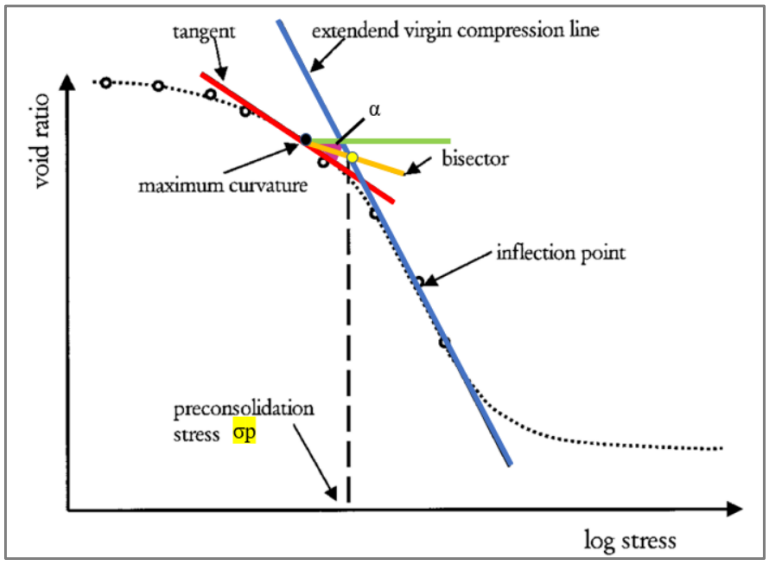

Figure 3.2. Determining Pre-Consolidation Stress (σ_p) using Casagrande's Method.

Figure 3.2 illustrates Casagrande's graphic method for determining pre-consolidation stress. The point of greatest curvature on the consolidation curve (highlighted in black) is identified. A tangent is drawn at this point, followed by a horizontal line. The bisector of the angle between these lines intersects the virgin compression curve, indicating the pre-consolidation stress (σ_p).

Pre-consolidation stress (σ_p) is the maximum effective vertical stress a soil has previously experienced. When current effective stress (σ_z) is less than or equal to σ_p, the re-compression index (C_r) must be used instead of the compression index (C_c). σ_p is determined indirectly from the consolidation curve $\log(\sigma_z - e_0)$ obtained through oedometric testing. This curve shows the transition point between the reloading consolidation phase and the virgin loading phase (Figure 3.2).

The constitutive relationships between σ_z and e follow (Gambolati, et al., 1998):

$$e = \begin{cases} e_0 - C_r \log\dfrac{\sigma_z}{\sigma_{z0}} , & \sigma_z \leq \sigma_p \\ \\ e_c - C_c \log\dfrac{\sigma_z}{\sigma_p} , & \sigma_z > \sigma_p \end{cases} \tag{3.11}$$

where:

- e_c is the void index at the preconsolidation stress;
- σ_{z0} is the effective stress at very shallow depth;
- e_0 is the void index at depths with stresses equal to σ_{z0}.

By means of Equations (3.11), the sediments geomechanical behavior is completely defined by the two parameters e_0 and C_c (or C_r). Once the relationship between σ_z and e is known, it is possible to calculate c_b through Equation (3.10).

The following relation is used to compute the hydraulic conductivity (Koster, Stafleu, and Stouthamer 2018):

$$K_z = K_{z_0} 10^{\left(\frac{e-e_0}{C_k}\right)} \tag{3.12}$$

with K_{z_0} the vertical hydraulic conductivity at e_0, that is, for a soil close to the land surface, and C_k a parameter related to lithology and void ratio.

3.3. Numerical model implementation

The NATSUB3D simulator solves the partial differential equations described in the paragraph 3.1 by means of a tetrahedral FE discretization. It implements the following algorithm:

- The sedimentation thickness $d\ell_i$

$$d\ell_i = \omega(x,t)\,\Delta t_i \tag{3.12}$$

  is initially computed to evaluate the soil deposited during the i-th time step Δt_i;

  Note that if $d\ell_i > \Delta z_{max}$, Δt_i must be reduced to $\Delta t_i = \frac{\Delta z_{max}}{\omega}$, where Δz_{max} is the threshold value fixed for the maximum Fes thickness;
- σ_t is computed by Eqaution (3.2) and updated;
- The system of nonlinear ordinary differential equations obtained by the numerical discretization of Equation 3.1 is solved through the Picard iterative scheme;

- Once obtained the overpressure at the k+1-th non-linear iteration $p^{(k+1)}$, the Terzaghi relation $\sigma_z{}^{(k+1)} = \sigma_t - p^{(k+1)}$ allows to compute $\sigma_z{}^{(k+1)}$. Note that σ_t doesn't vary in he time interval Δt_i and remains constant since its value changes only in response to the accumulation of sediment on the surface of the landform.
- $\Delta z_i^{(k+1)}$ (i.e., the depth interval between two adjacent nodes) is updated by solving the equation

$$\Delta z_i^{(k+1)} = \Delta z_i^0 + \Delta u_i^{(k+1)}$$

  in which Δz_i^0 is the depth interval in the previous step and $\Delta u_i^{(k+1)}$ is calculated with Equation (3.9).
- At this point if the difference between the solutions of two subsequent iterations does not overcome the established tolerance, system convergence is obtained.
- The new (i+1) time step starts checking the need for mesh update.
- A new timestep begins and the model verifies the need to update the mesh by relating the thickness of the element h_{i+1} above a generic node *j* with $\Delta z_{max} \geq h_{i+1}$ (Figure 3.3), while its characteristics are assigned based on the properties of the type of sediment corresponding to the shallowest depth (Xotta, et al., 2022).

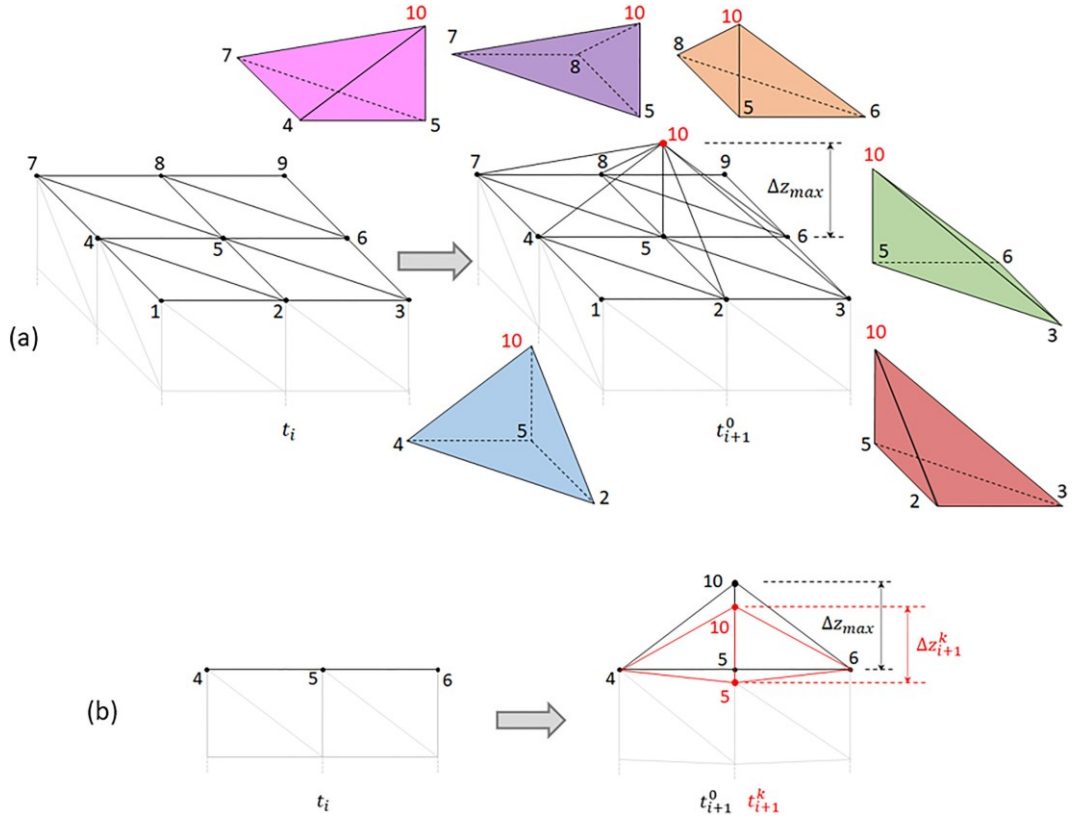

Figure 3.3. NATSUB3D simulator's ynamic mesh.
(a) Visualization of tetrahedra added at time tᵢ+1 to the growing finite element mesh when the sedimentation thickness above node 5 reaches the prescribed thickness Δzmax. Adding node 10 implies the creation of new elements above those sharing node 5. In this example, six new tetrahedra are added to the previous mesh, individually depicted and highlighted in different colors. The vector containing the nodes on the top is updated from (1, 2, 3, 4, 5, 6, 7, 8, 9) at time ti to (1, 2, 3, 4, 6, 7, 8, 9, 10) at time ti+1.
(b) Vertical section of the mesh through the alignment connecting nodes 4, 5, and 6, illustrating how the mesh deforms due to compaction caused by the sedimentation Δzmax above node 5.

3.4. NATSUB3D advanced configuration starting (restart)

The NATSUB3D simulator provides the so called “restart” feature, which allows to start the model from an advanced configuration obtained by a previous one. This is crucial when the focus is on the final stages of the model, but there is still a need to reproduce the previous geology to accurately simulate the system's behavior. For instance, in the present study, the aim is to investigate the development of the artificial salt marsh following the nourishment activities over the past 12 years. However, it is essential to reproduce the entire stratigraphy

potentially affected by anthropogenic interventions, which took approximately 13,600 years to form. It is evident how computational costs can be significantly reduced by simulating the natural geology only once and subsequently using it as input model in a second simulation that focuses on the most critical and brief phases associated to the artificial mourishments without starting from zero.

The tests conducted to validate this feature of the simulator initially focused on a simple case related to a previous study (Xotta et al., 2022), and then on the model of the Le Sorelle-B salt marsh. The results of these tests are reported in Chapter 6, along with other results from the numerical model. To anticipate the outcome of these tests, using the Restart can lead to a non negligible reduction in the soil compressibility of the strata before the restart – the restart stiffens the model used as advacend configuration. By comparing the same zones at the same time but with and without the use of Restart in the Le Sorelle-B case, a reduction from 8.4% to 21.8% in the c_b parameter was noticed. This led to a significant underestimation of the overall saltmarsh subsidence.

4. NATSUB3D SIMULATION OF LE SORELLE-B

NATSUB3D has been used to simulate the evolution of Le Sorelle-B. In this chapter the computational tetrahedral grid (i.e., mesh) (i), the boundary conditions (ii), the assumed initial materials properties are described (iii) and the procedure for lithology and sedimentation rates (iv).

To achieve a comprehensive understanding of the system, the model aim is to simulate the Holocene period along with the various phases of nourishment, emphasizing the importance of also modeling the long-term natural evolution after the recent nourishing activities. This approach is critical as it provides the only consistent distribution of hydro-geomechanical properties, upon which the artificial nourishment can be applied and its subsequent behavior analyzed.

4.1. Computational mesh

At the beginning of the simulation, the grid is 2D and it is created by using the software ArgusOne based on the available bathymetric data. In particular, the model domain encompasses the salt marsh Le Sorelle-B as delimited by the wooden poles established for nourishment containment and a surrounding rectangular area (Figure 4.1). The rectangle is 794.3 m wide in the north-south direction and 662.9 m in the east-west one.

The mesh size was set equal to 20 m at the perimeter, 10 m in the inner region of the marsh and refined to 3 m along the excavated channel to better reproduce its steep slope and the deposition process during the nourishments since a relevant amount of the sediments reached the lower zones.

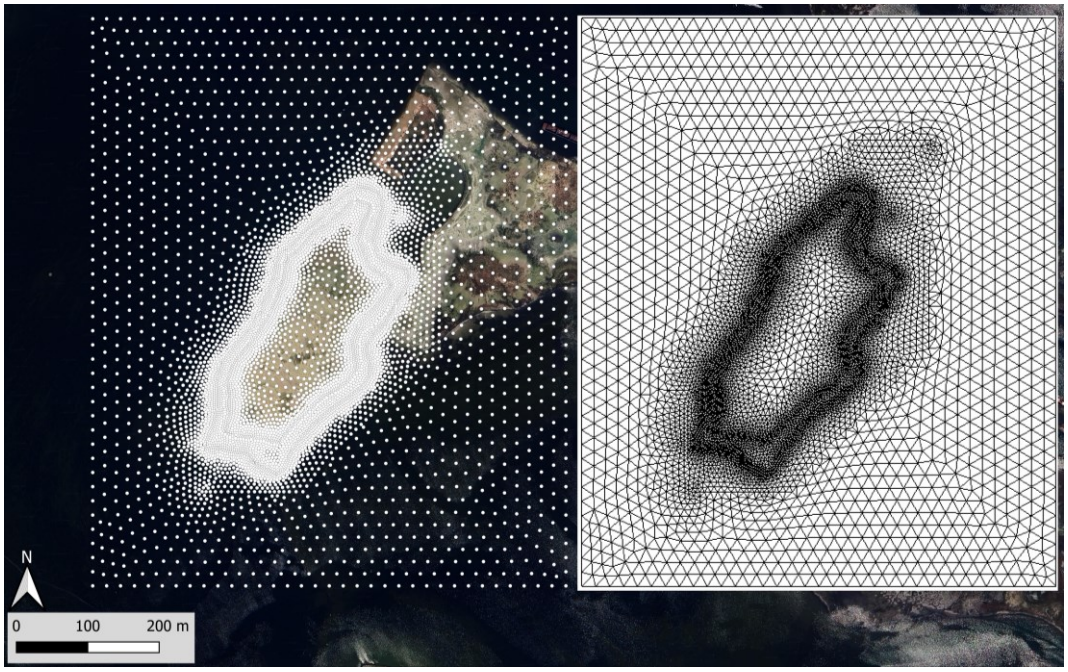

Figure 4.1. 2D grid resulting from ArgusOne to discretize the model domain with triangular elements.

The 2D grid is constituted by 7480 nodes and 14958 elements (Figure 4.1)

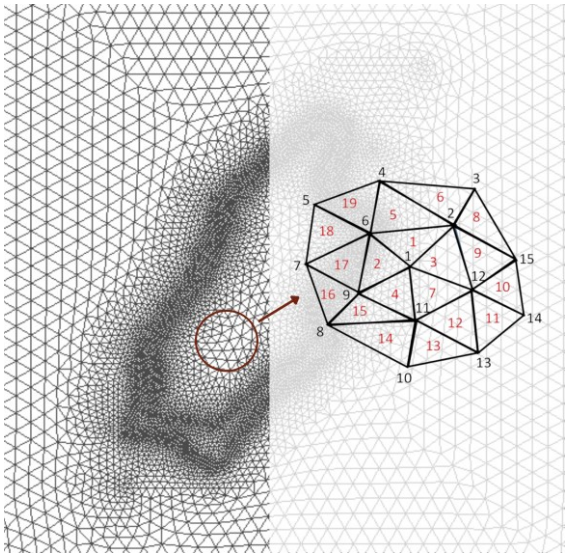

Figure 4.2. Nodes and elements form the grid (2D, in this case).

The mesh boundary is sufficiently far from the salt marsh perimeter to avoid boundary disturbance: there is an at least 150 m separation between the salt marsh perimeter and the model boundary. This is one of the improvements implemented

on the previous study (Meneghini, 2022) where the simulated domain was smaller, with the boundaries too close to the salt marsh (Figure 4.3):

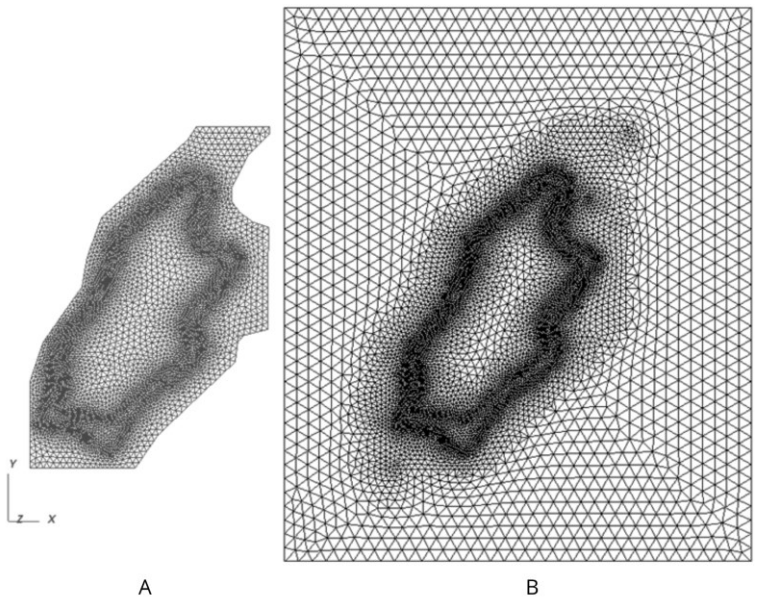

Figure 4.3. (A) before (Meneghini) and (B) after the current mesh extension for Le Sorelle-B site model

The sediments build up from a 3D tetrahedral mesh starting with a 10-cm-thick incompressible layer. This layer represents the Caranto unit, i.e, the stiff over consolidated deposit representing a "basement" for the Venice Lagoon over which it developed during the Holocene from around 13'600 years ago.

As mentioned above, when the buildup of sediments over a node exceeds the fixed threshold, a node is added by the simulator on top of the previous one (see Figure 3.3). Consequently, new tetrahedral elements are created over every triangular face that shares the node beneath the new one. A 10 cm threshold is fixed for $\Delta z_{,max}$.

The sedimentation rates are discussed in more detail in paragraph 4.4.

4.2. Boundary conditions

Boundary conditions are needed to solve the partial differential equations.

Model Boundary Conditions:

- **Impermeable Basement:** The model assumes an impermeable basement to prevent water flow.
- **No-Flow Lateral Boundaries:** Lateral surfaces are considered impermeable, with no water flow across them (Neumann conditions).
- **Hydrostatic Pressure at Top:** Null Dirichlet conditions are applied at the top boundary, representing hydrostatic pressure. No overpressure can develop at the soil surface.

Model Updates with Sediment Accretion:

- When the thickness of sedimented deposits above a surface node reaches a predetermined threshold, a new node is added to the top of the model (Figure 4.4).
- Boundary conditions are updated to reflect the new node configuration.
- If the new node is on a lateral boundary, the vector containing Neumann or Dirichlet nodes is increased to include the new node index. This ensures accurate representation of the changing boundary conditions as the model evolves.

4.3. Materials geomechanical properties

A number of eight soil classes has been used to characterize the Holocene deposits and the nourishment soils at Le Sorelle-B. The hydro-geomechanical

properties and parameters of the following eight lithological layers are required by the NATSUB3D: Caranto, silty loam, clayey sand, clay silt, peat and the three materials for the nourishment. All nourishment phases were initially assumed to be characterized by the same soil type as their provenance is unknown. Parameter values (Table 4.1) were based on literature and oedometric tests from nearby salt marshes (La Grisa and Lazzareto) in the Venice Lagoon (Bonardi and Tosi, 1994; Zoccarato et al., 2022).

Table 4-1. Initial hydro-geomechanical properties of the lithological classes used in the modelling of Le Sorelle-B salt marsh

	Soil material	γ_s [kg/m³]	e_0 [-]	C_c [-]	C_r [-]	σ_0 [kPa]	σ_p [kPa]	K_{z0} [m/s]	$K_{x,y}/K_z$ [-]
8	Nour. 2023	2650	10	0.5	0.25	0.1	0.1	3E-06	3.0
7	Nour. 2021	2650	10	0.5	0.25	0.1	0.1	3E-06	3.0
6	Nour. 2019	2650	10	0.5	0.25	0.1	0.1	3E-06	3.0
5	Peat	1700	8	2.4	0.35	0.1	4	1E-07	3.0
4	Clayey silt	2616	1.765	0.14	0.04	0.1	4	3E-07	3.0
3	Sand	2650	1	0.033	0.033	0.1	4	1E-05	3.0
2	Silty loam	2650	1.1	0.23	0.07	0.1	4	1E-06	3.0
1	Caranto	2600	0.455	0.086	0.017	0.1	4	1E-07	3.0

Table 4-1 reports the initial – prone to be changed during the parameter-calibration phase in the following chapter – hydro-geomechanical properties of each soil stratum. Based on available dating (Figure 2.17), the deposition intervals of the various soil classes addressed in the simulation are summarized in Table 4.2.

Table 4-2. Deposition intervals for each lithological class used in the modelling of Le Sorelle-B salt marsh.

	Soil material	Deposition interval [y - y]
8	Nour. 2023	13641.25 - 13641.42
7	Nour. 2021	13639 - 13639.33
6	Nour. 2019	13631 - 13637
5	Peat	12438 - 13631
4	Clayey silt	10631 - 12438
3	Sand	9034 - 10631
2	Silty loam	1931 - 9034
1	Caranto	0 - 1931

4.4. Decompaction of the original soil column

Pre-processing is essential for calculating sedimentation rates (ω) using NATSUB3D. This involves decompacting the actual soil column at each node location (x) to determine the original uncompacted thickness.

A 1D decompaction model was used to calculate the original uncompacted thickness b between depths z1 and z2. This model also determines the corresponding change in effective stress with depth. The decompacted thickness is calculated using the Formula (5.20) provided by Gambolati et al. (1998).

$$b = (1 + e_1) \int_{z_1}^{z2} \frac{dz}{1+e(z)} \tag{5.20}$$

Where

- e_1 is the void index value corresponding to the depth of z_1
- $e(z)$ is the void index value corresponding to the depth of z
- z_1 and z_2 are the depths at which the soil column to be decompacted lays

By knowing the original or uncompacted thickness of each stratum, its relative averaged sedimentation rate is easily computed, as it is discussed in the following paragraph.

4.5. Sedimentation rates – ω

Sedimentation rates, ω, represent the flow of sediments expressed as meters per year for a specific soil material. They are essential to recreate the landform evolution. Sedimentation rates vary in space and time $\omega = \omega(x, t)$ and each value corresponds to a (x, t) position and time of a node in the Sorelle-B model. They basically consist of the amount of sediment delivered above a specific node in one year over the time for the starting and ending of the relative sedimentation.

Sedimentation rates are deducted by the stratigraphic sequence provided by boreholes and by the carbon-14 age testings (Figure 2.17). Given a soil stratum and the deposition times t_1 and t_2 for sediments at depths z1 and z2, respectively, the average sedimentation rate (ω) within the time interval $\Delta t = t_2 - t_1$ can be calculated as follows:

$$\omega = \frac{\Delta h}{\Delta t}$$

where

- $\Delta t = t_2 - t_1$, the time interval in which the sedimentation occurs;
- Δh , the soil stratum thickness.

The latter one is calculated as reported in the previous paragraph for the Holocene naturale sequence.

The procedure used to determine the sedimentation rates associated to the nourishments is described in detail.

4.5.1. Sedimentation rates for nourishments

Le Sorelle-B has been nourished three times starting in 2019. Unfortunately, the first topographycal survey was carried out by the Geomatic research group of University of Padua in June 2021. Hence, only the last two nourishments have been characterized with the following method. The timeline for relevant events is promptly summarized in the following (see also Figure 2.21 above):

- June 2021: University of Padua topographical survey by means of total stations;
- September - December 2021: second nourishment;
- January 2022 - bathymetric survey by the local Port Authority;
- August 2022 - University of Padua UAV photogrammetry survey;
- October - November 2022: third nourishment;
- January 2023 - University of Padua UAV photogrammetry survey.

These bathymetries enable us to compute the thickness of sediments poured onto the salt marsh.

The processing of survey data is mainly carried out with Surfer 13 and QGIS 3.16 softwares. The first one is a gridding software designed to interpolate scattered data and carries out two critical tasks in our case:

- create a regular grid from scattered points (x, y, z) given in a .txt file and compute the elevation difference for each point between two grids obtained by topographic surveys or bathymetries;
- mapping the resulting grid into the mesh nodes of Le Sorelle-B model in order to assign the elevation difference to every node of the model mesh by means of the “Residual” operation.

QGIS is used to compare and visualize results and other geodata, but also to change their coordinate reference system (CRS) when it differs with the model’s coordinate

system, the EPSG (European Petroleum Survey Group) 3003 - Monte Mario / Italy zone 1, and to match them.

4.5.2. Procedure for determining sedimentation rates for salt marsh nourishment

The first nourishment (2019) characterization and the related sedimentation rate was provided by the previous thesis work on Le Sorelle-B, so this description mainly regards the other two nourishments.

To obtain a nourishment thickness map, firstly a grid is created by interpolating scattered data from measurements. Surfer provides several gridding methods; kriging and triangulation with linear interpolation were preffered in this work.

The second nourishment (2021) is obtained by the subtraction (A-B) where (A) is the Port Authority 2022 bathymetry and (B) the University of Padua 2021 topographical survey (B). The Port Authority map was provided as an AutoCAD file; hence it was exported into a .dxf format before gridding it on Surfer (Figure 4.4).

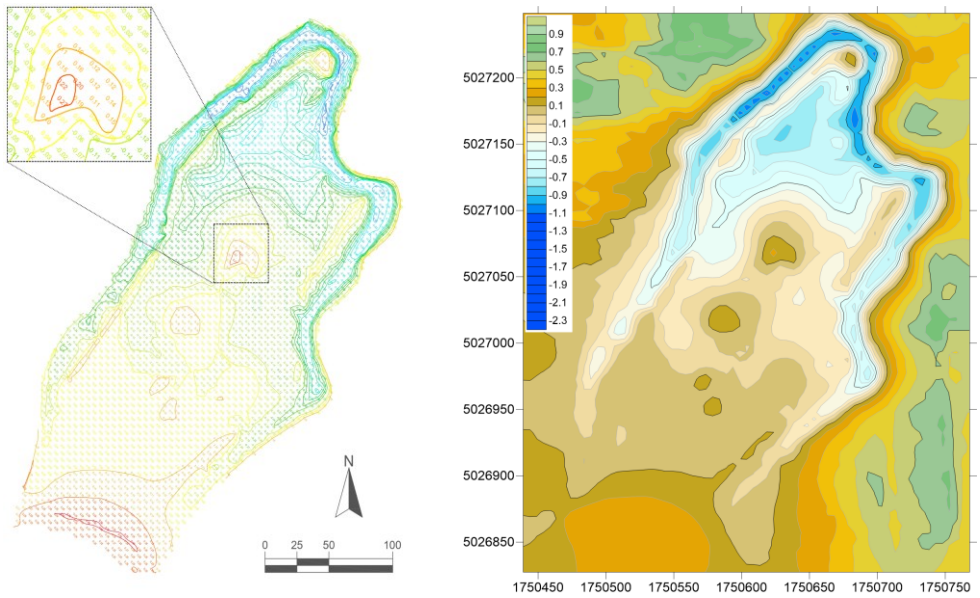

Figure 4.4. Port Authority's 2022 bathymetry as AutoCAD file and the resulting contour map in Surfer after the gridding.

The UniPD bathymetry (Figure 4.5) was already processed in the previous thesis work and the relative grid file was already available. Both bathymetries were checked and processed in QGIS since they required a CRS transformation to match the project's CRS (EPSG: 3003) before gridding.

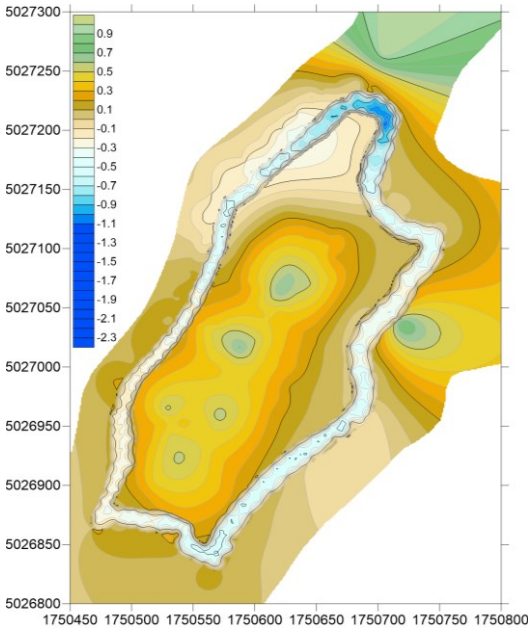

Figure 4.5. Padua University 2021 contour map in Surfer after the gridding (G. Meneghini, 2022).

Once the bathymetry grids are created, the Surfer "Residual" function is employed to interpolate grid values onto the numerical model mesh, enabling the execution of subsequent operations. Consequently, the Surfer "Math" function was used to compute the difference between the grids simply as C=A-B (Figure 4.6).

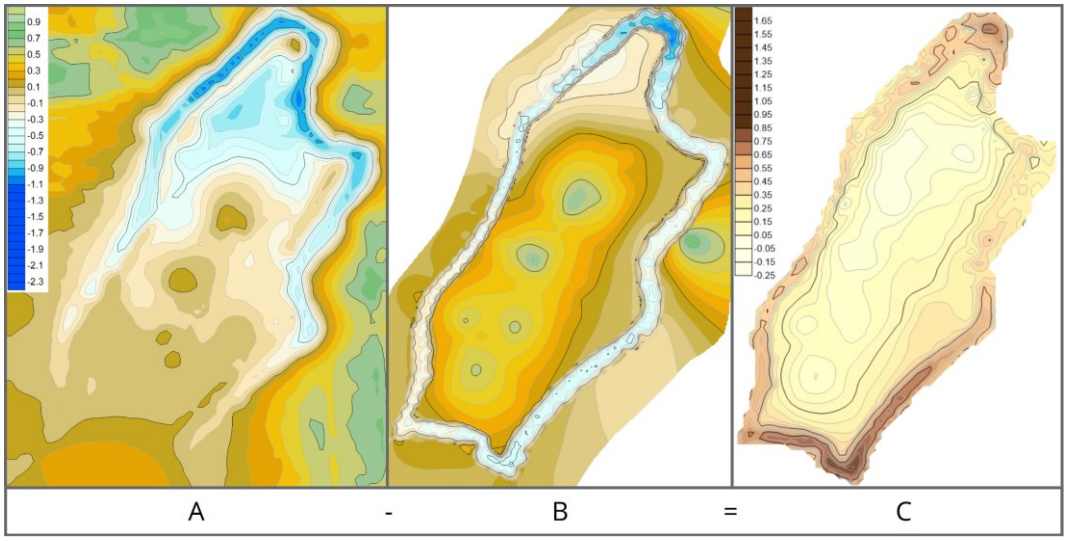

Figure 4.6. Second nourishment (2021) contour map resulting from the difference between bathymetries. *Port Authority's 2022 bathymetry (A) and University of Padua 2021 one (B) of the Sorelle-B salt marsh on Surfer along with the resulting blanked difference map (C) of the second nourishment determination - units of measure in meters above mean sea level*

The output results in a grid with the same nodes positions of Le Sorelle-B in the x and y directions, while the z value corresponds to the thickness of nourished sediments.

There are two relevant operations left:

- sediments on the saltmarsh are confined with structures along the perimeter and only the points inside of it are relevant. To model this confinement the output grid is “blanked” around the perimeter of the saltmarsh. For sake of clearness, the above nourishment map (C) is already blanked;
- the NATSUB3D simulator cannot consider nor model the salt marsh erosion: hence, points in the output grid that present negative values must be assigned with a z value equal to 0; this consists in a non-conservative hypothesis and represents one of the limitations of the present version of the NATSUB3D simulator.

Figure 4.7 shows the obtained outcome: a grid with the mesh nodes positions and null z values apart from those nodes that are located within the salt marsh where the actual sediments thickness is assigned.

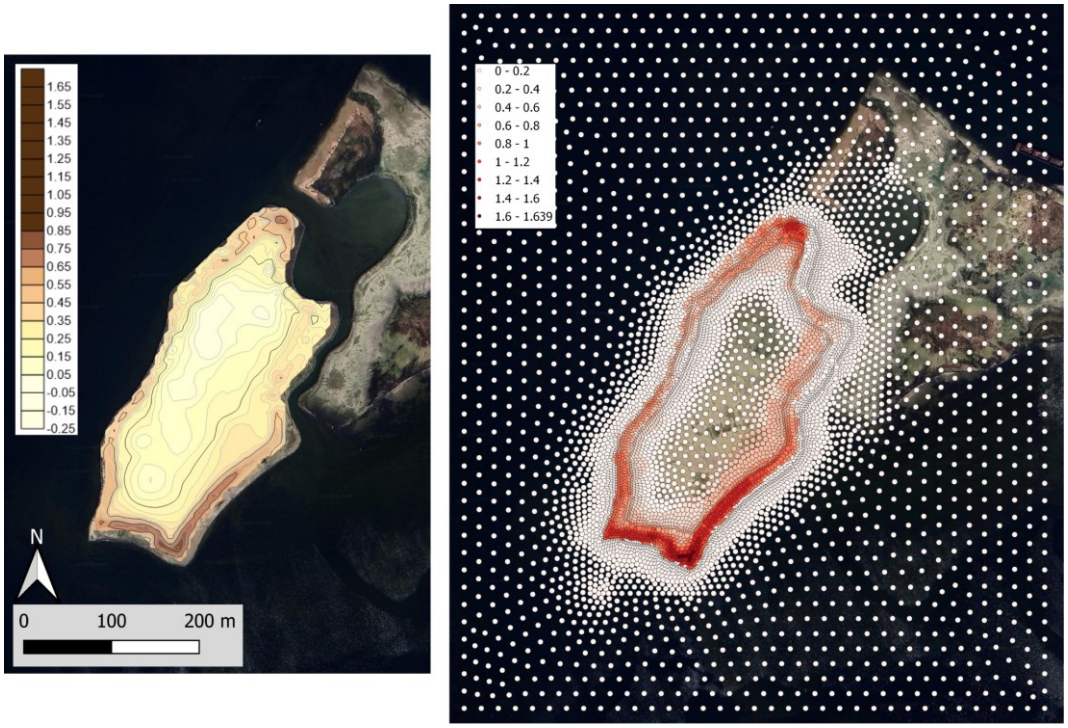

Figure 4.7. Second nourishment (2021) contour map over satellite image (right) and the corresponding values interpolated over the model grid (left).
Notice that negative values are nulled in the grids nodes version.

Finally, the sedimentation rate is obtained by dividing these interpolated values by a factor equal to the fraction of year in which the nourishment occurred:

$$\omega_{model} = \frac{\omega_{actual}}{\Delta t/12}$$

where

- ω_{model} is the sedimentation rare assigned to model nodes in m/y;
- ω_{actual} is the total sedimentation occurred on Le Sorelle-B artificial salt marsh in m;
- Δt time interval in months during which the nourishment occurred.

Since the second nourishment occurred in four months, the values obtained with the Residual must be divided by ⅓ (i.e., multiplied by a factor of three). The time interval over which this omega (i.e., omega7) is applied ranges from the modelling time 13639 y to 13639.33 y.

Analogous steps are followed to obtain the sedimentation rate for the third nourishment (2022) by using as input bathymetries the UAV photogrammetric surveys (August 2022 and January 2023). In this case, gridding their scattered data conveyed to comparable grids, and it was not necessary to interpolate them onto the model mesh in the first place. Avoiding this coarser interpolation allowed them to preserve their higher resolution (points are given every 10 cm) during the difference operation between the grids. At the same time, part or all of this precision is lost when interpolating the resulting grid onto the numerical model mesh.

The same blanking and nulling the negative values operations were performed to obtain the sedimentation rate omega8.dat file (Figure 4.8). To convert the nourishment thickness into sedimentation rate, the thickness of new sediments was multiplied by six since it occurred over two months. The nourishment between the simulation times 13640.08 years and 13640.25 y. The nourishment reported on the model nodes are shown in **Error! Reference source not found.**.

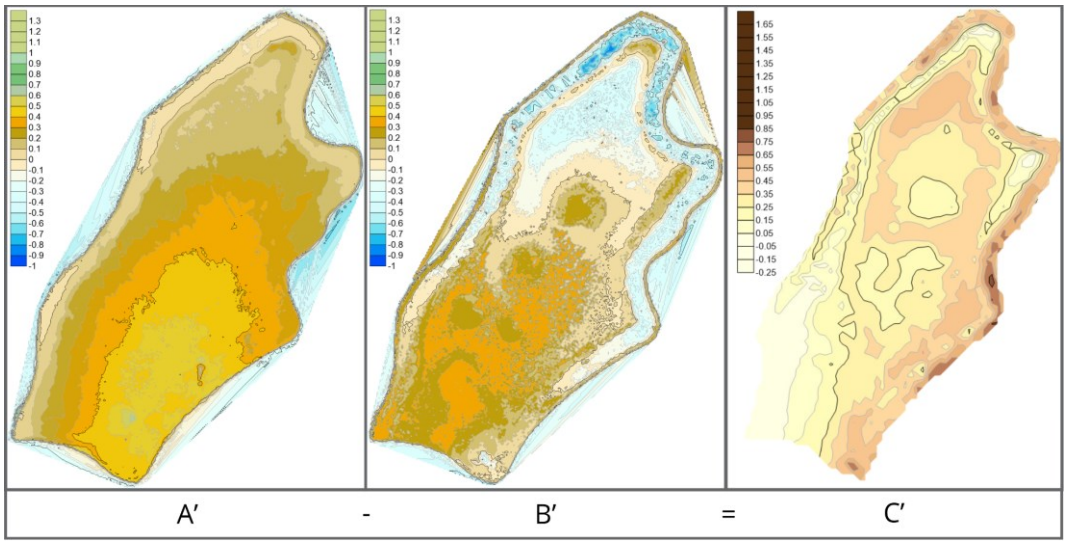

Figure 4.8. Third nourishment (2022) map resulting from the difference between bathymetries. *January 2023 (A') and August 2022 (B') topographic maps of the saltmarsh on Surfer along with the resulting blanked difference-map (C') for the third nourishment determination - units of measure in meters and coordinates are given in EPSG:3065 - IGM95 / UTM zone 33N.*

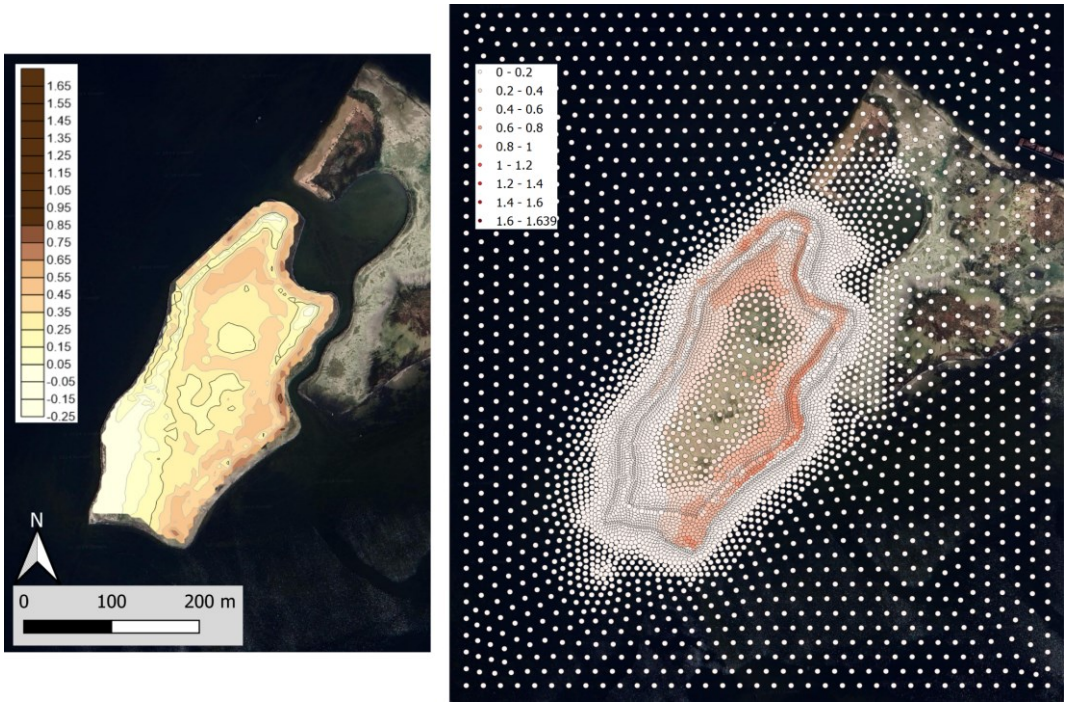

Figure 4.9. Third nourishment (2022) contour map over satellite image (right) and the corresponding values interpolated over the model grid (left).
Notice that negative values are nulled in the grid's nodes version.

Contour maps for the three nourishments are shown together in Figure 4.10 to ease the comparison between them.

Figure 4.10. Nourishments contour maps over satellite image of the Sorelle-B salt marsh from 2019 to 2022.
The color scale is different for the 2019 nourishment to better represent the smaller contours' values.

5. RESULTS OF MONITORING DATA ANALYSIS

In this chapter, we will see how the surface of the salt marsh has evolved over time and the NEC stations records.

5.1. Evolution of Le Sorelle-B landform surface

The drone scans conducted after the second nourishment in 2021 provide a detailed view of the evolution over time of the Le Sorelle-B salt marsh (Figure 2.21). Additionally, the high-resolution (10 cm) Digital Terrain Models (DTMs) obtained from these scans offer valuable information and maps related to changes in the surface of the salt marsh. This facilitates easier observation of changes that occurred before and after the nourishments.

The available DTMs for the site are referred to November and December 2021, August 2022, and January, May, and September 2023. Unfortunately, a significant part of the bathymetry from November 2021, which is also the first, is unusable. This is likely due to the presence of water on the surface of the artificial salt marsh during the survey, which prevented correct sampling. The flooded areas are characterized by an unphysical elevation of about 7 m below or above sea level and are therefore inconsistent with the actual field conditions.

Similar to the operations that allowed us to obtain the sedimentation rates described in paragraph 4.5, starting from December 2021, contour maps showing the differences between one DTM and another were created (Figure 5.1). The map related to the November 2021 DTM is in grayscale and uses a much wider range of ad hoc values to highlight the discrepancy between it and the other DTMs, emphasizing its unusability.

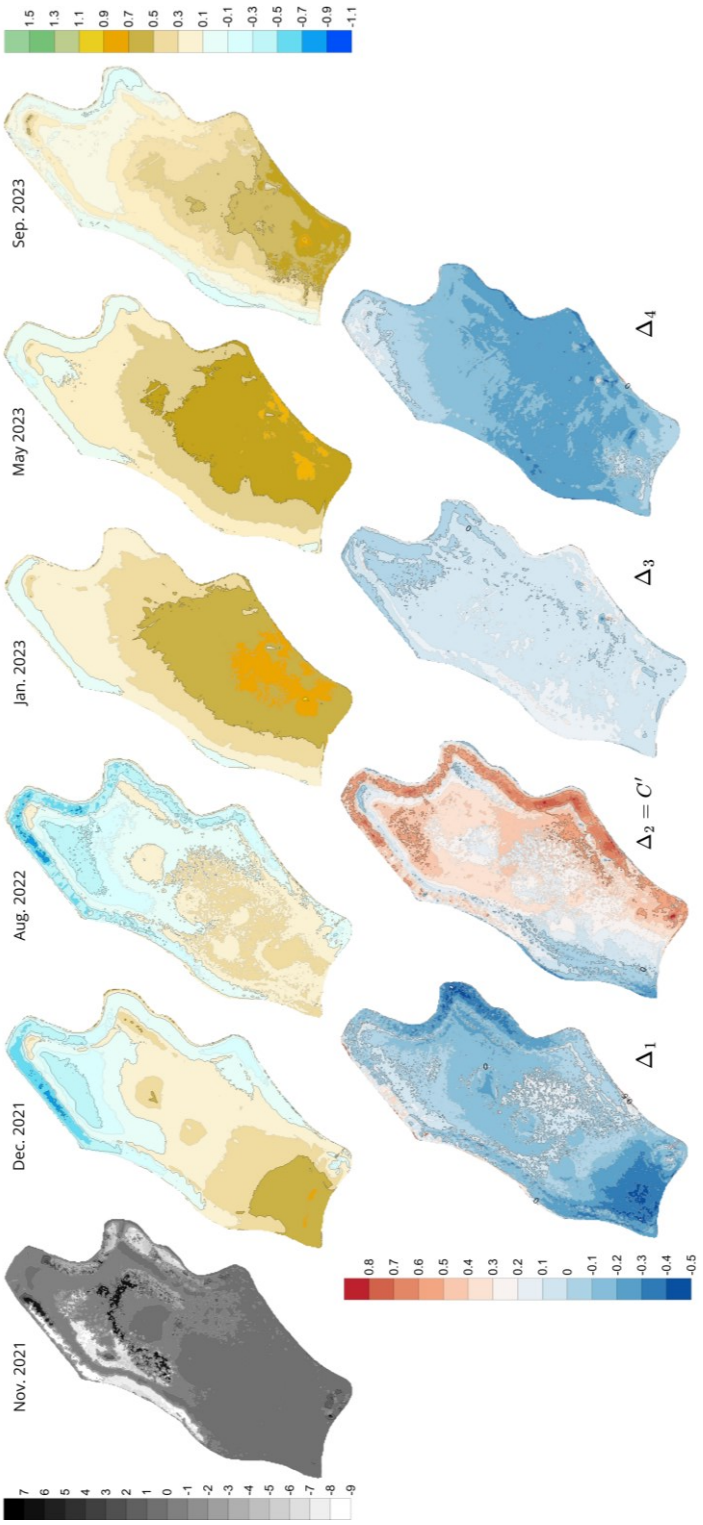

Figure 5.1. DTMs of Le Sorelle-B artificial saltmarsh and countour maps of the differences between a DTM and the previous one. Scale is in meters above mean sea level.
C' is reffered to the third nourishment (2022) contour map (Figure 4.8)

In addition to the elevation variations between different bathymetric surveys, the Surfer software enables the calculation of volume variations between them. Decreases in elevation between surveys will correspond to negative volumes, and increases will correspond to positive volumes. This functionality also allows for the monitoring of cumulative volume changes starting from the reference bathymetry, which in this case is the one acquired in December 2021.

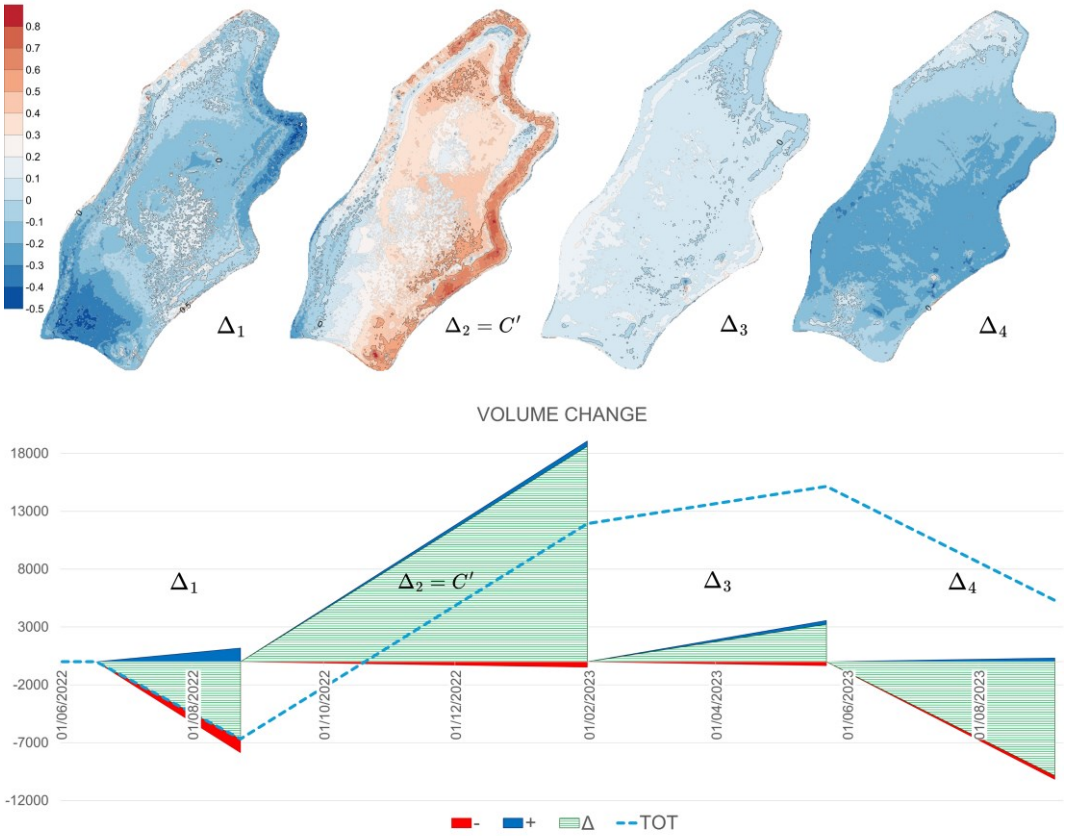

Figure 5.2. Incremental volume and cumulative volume on Le Sorelle-B saltmarsh starting from the December 2021 DTM.
The light blue dash line represents the cumulative volume. The red and blue areas the loss and gain of volume between two DTMs respectevel, while the striped rectangles represent the net volume change relative to the same two DTMs. Values in m³.

Inspection of Figure 5.2 reveals that the nourishment that took place between August 2022 and January 2023 greatly contributes to the overall increase in volume (net increase of 1800 m³) and, in parallel, the average elevation of the salt marsh surface. Furthermore, during the first and last intervals there are significant volume losses: this is mainly due to the land subsidence and autocompaction in soil strata

but also probably due to the direct loss of sediments caused by storm surges or their escape through the openings in the contermination which was built in summer 2021.

5.2. NEC records and saltmarsh surface elevation change

The DTMs are also used to determine the elevation of the soil near the NEC stations. This allows us to compare the saltmarsh surface evolution at the NEC stations with the lowering of deeper strata monitored by the NECs themselves. This also enables the immediate correlation between soil deposition – where the corresponding DTM zone gains elevation – over the NEC zone and the consequent subsidence, as the NEC's plate embedded in the soil lowers (Figures 5.3, 5.4). For the reader's ease, Figure 2.20, which illustrates the NEC positions, is reported as Figure 5.5.

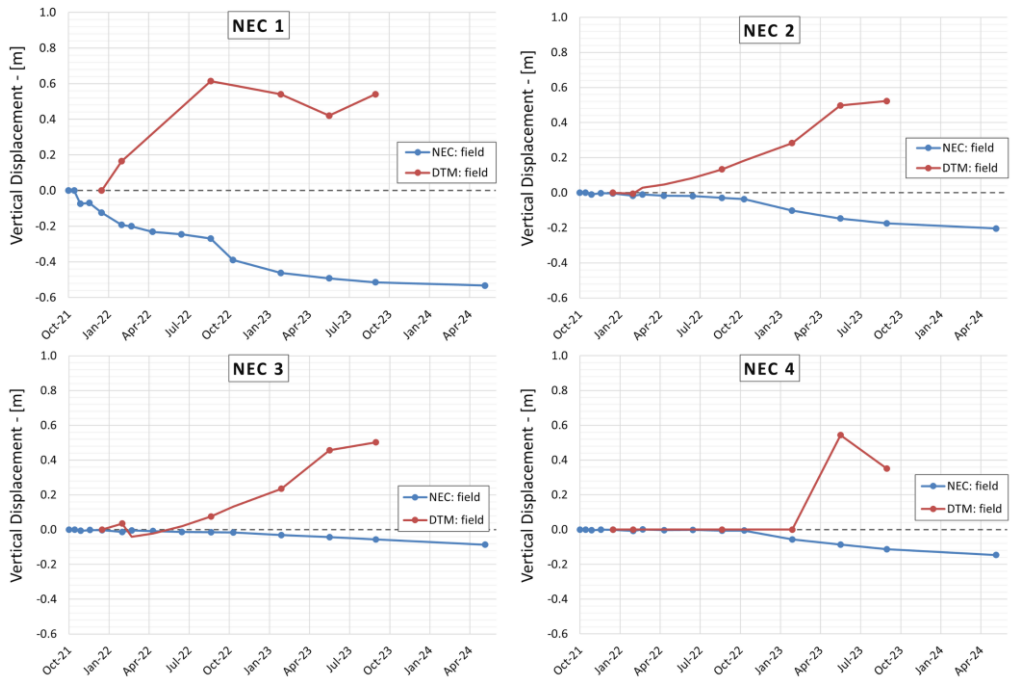

Figure 5.3. Comparison between the displacement occurring at the surface of the saltmarsh nearby a NEC and the vertical displacement measured by the NEC itslef. NECs from 1 to 4.

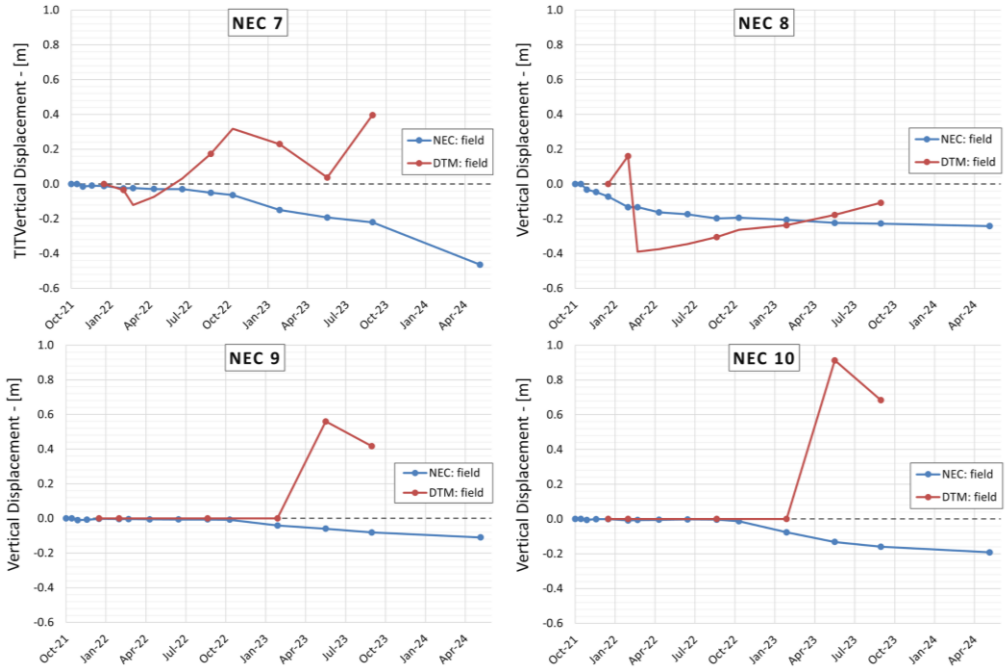

Figure 5.4. Comparison between the displacement occurring at the surface of the saltmarsh nearby a NEC and the vertical displacement measured by the NEC itslef. NECs from 5 to 10.

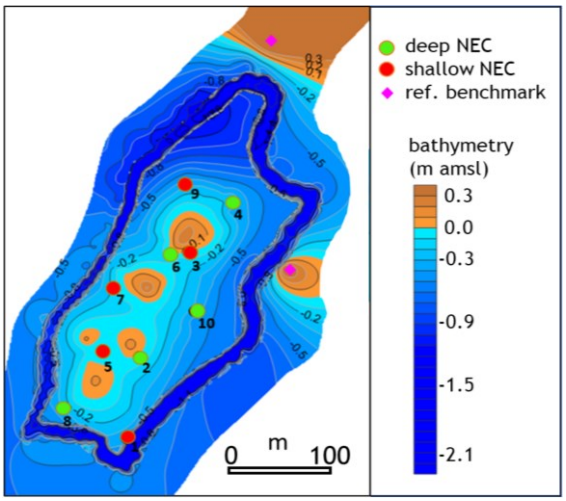

Figure 5.5. UniPD bathymetry map (2021) showing the position and number of deep NEC in green and shallow NEC in red (Meneghini, 2022).

The vertical displacement relative to the DTMs is referenced to a starting measurement taken in November 2021. The DTM values are obtained by averaging the elevation of a cloud of DTM points surrounding the NEC position. This introduces some uncertainty in the measurement, and the overall data quality is also

affected by the low measurement frequency and the failures of the retainment structure. Despite this, for NEC 1, 2, and 5, it is quite evident that when the saltmarsh surface rises, mainly as a consequence of nourishment or sediment reallocation, the corresponding NEC subsides accordingly. The steepest segments of the DTM correspond to the last nourishment in 2022. For NECs 7 and 8, abrupt decreases in DTM displacement are likely caused by sediment being missed due to failures in the retainment structure in several sections of the saltmarsh perimeter. These two NECs are the closest to the perimeter along with NEC 1, but the DTM of the latter apparently shows behavior consistent with the amount of sediment deposited close to it.

5.2.1. Secondary consolidation

Regarding the NEC records, the frequency and precision of measurements are higher, enabling a better depiction of the subsidence phenomenon at artificial saltmarshes, which can be distinguished in two phases. When a saturated soil layer consisting of fine-grained soils is subjected to loading, the resulting deformation occurs in two successive phases: primary consolidation and secondary consolidation.

During the primary consolidation phase, the deformation of the soil structure is related to the ability of the pore fluid to drain. Initially, the load is instantaneously transferred to the pore fluid, causing an increase in pore pressure. This excess pore pressure dissipates over time as the soil drains, and the initial total stress applied becomes effective as it transfers from the pore fluid to the soil structure. This transfer increases the effective intergranular stress, leading to soil deformation (compaction).

Once primary consolidation ends, the excess pore pressure has been completely dissipated. However, the soil continues to deform without changes in pore-water pressure, entering a phase known as secondary consolidation. Secondary

consolidation is due to the rearrangement of the soil skeleton after the disturbance induced during primary consolidation. The deformations that occur during secondary consolidation are also known as creep deformations, and the trend of displacement is characterized by a negative logarithmic law.

These two phases are especially evident in NEC 1 records for both the last nourishments (2021 and 2022). Starting from November 2021, the first and steeper segment highlights the primary consolidation, while the second and flatter segment represents the elastic component of compaction (i.e., creep phenomenon). This pattern replicates for the second nourishment, which starts at the end of the first creep phase (Figure 5.6).

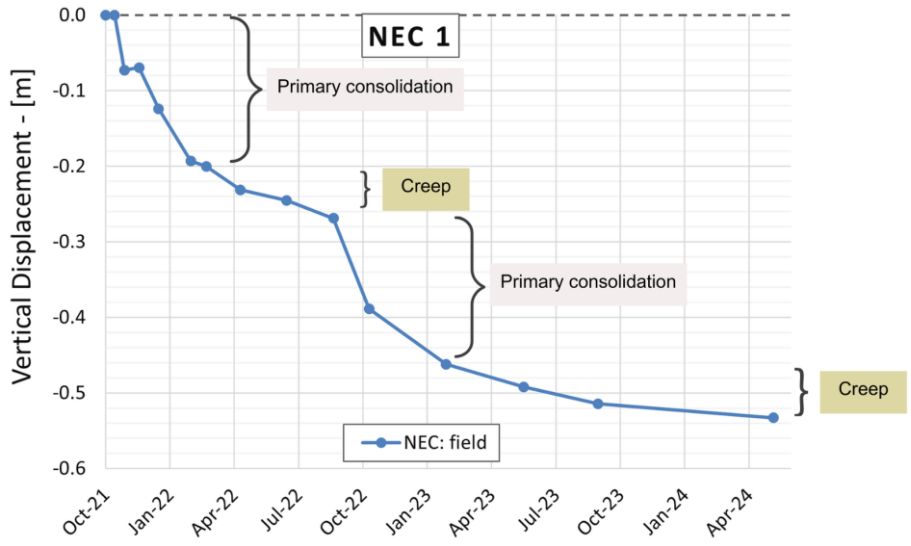

Figure 5.6. First and second (creep) consolidation phase for the Le Sorelle-B saltmarsh at NEC 1.

Despite it may seem that creep plays a marginal role, it must still be accounted for in the overall subsidence. As already mentioned, the long-term survival of a saltmarsh is a matter of a few decimeters, and the creep phenomenon carries on for decades, even if with diminishing intensity. The creep effect is most evident in NEC 8, but almost all NEC stations exhibit it. Only NEC 3 and 6 show a less well-depicted negative logarithm trend.

Since all simulations were carried out without considering the creep phenomenon, the NEC records have been cleaned of the effect of secondary deformation by removing the displacements recorded after the complete dissipation of the pore-water pressure. This allows for a better comparison of the numerical model results with the observed measurements (see Chapter 6).

To achieve this aim, it is necessary to compute the secondary consolidation coefficient C_α also known as creep coefficient which represents the slope of the deformations (ϵ)-logarithm of time curve:

$$C_\alpha = \frac{\Delta\epsilon}{\Delta\log(t)}$$

where

- $\Delta\epsilon = \frac{\Delta h}{H}$ is the deformation computed by dividing the difference between displacements Δh and the thickness of the soil column H;
- $\Delta\log(t)$ is the difference between the logarithm of the two-reference time t_1 and t_2,

C_α should be evaluated for both loading phases (when present) caused by nourishming operations. Once $C_{\alpha_{1,2}}$ are known, the amount of vertical displacement due to secondary deformations for the two phases can be evaluated as:

$$d_{s_1}(t) = C_{\alpha_1}\, H\, log\frac{t}{t_{ref}}$$

$$d_{s_2}(t) = C_{\alpha_2}\, H\, log\frac{t}{t_{ref}}$$

where

- is the vertical displacement induced by secondary consolidation at a certain time t from the beginning of the loading phase;

- t_{ref} is the time at which all the excess of pore-water pressure has been dissipated and the secondary consolidation starts.

Since H varies for each NEC and our scope is to clean the total displacement from the creep contribution, it was convenient to compute the product $C_\alpha H$ instead of C_α alone. $C_\alpha H$ is estimated for the last point (f) of the NEC data serie as the steepness of the displacement (d)-logarithm of time curve (time t starts at the beginning of the loading fase):

$$C_\alpha H = \frac{h_f - h_{f-1}}{log\left(\frac{t_f}{t_{f-1}}\right)}$$

The sudden increase of negative displacements observed at the end of the NEC 7 date serie do not allow proper compensation of creep deformations and the $C_\alpha H$ has been computed on the last reasonable value before the abrupt loss in elevation.

In order to give a steem of a possible C_α value for the NEC1, where the creep is very influent, the product $C_\alpha H = 0.1316$ was divided by H ranging from 6 m to 7 m, i.e.the distance of the NEC plate from the stiff caranto layer. Hence, $|C_\alpha| = 0.022 - 0.019$ which is coherent with other experimental value obtained at La Grisa and Campalto Venice Lagoon saltmarshes during fiel loading test (Zoccarato et al., 2022; Gatto, 2023). Once again, the lack of frequent measurements makes it difficult to obtain precise values for creep coefficient. Figures 5.7 and 5.8 show the results of the cleaning operation over creep phases for each NEC data series along the numerical simulation for the NECs displacement using default values (see Table 4.1). More on the numerical model results in Chapter 6.

Figure 5.7. NEC actual and creep-cleaned observed measure and initial-value numerical model elevation change at the NEC node for NECs from 1 to 8.

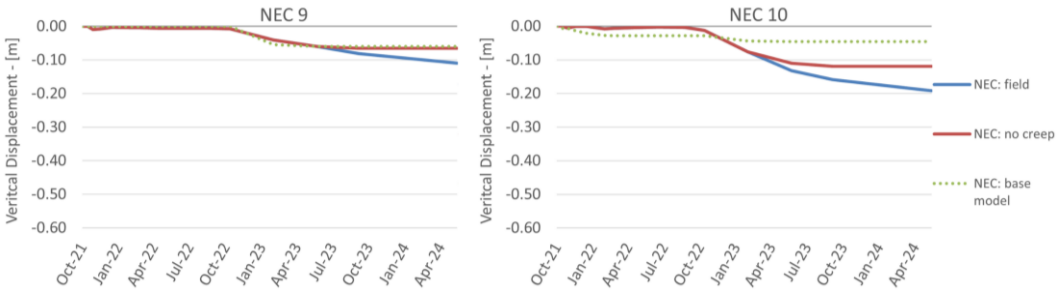

Figure 5.8. NEC actual and creep-cleaned observed measure and initial-value numerical model elevation change at the NEC node for NECs 9 and 10.

For NEC 3, 6 and 9 the numerical model lends a good approximation of the compensated NEC serie while for the remaining ones, there is an evident underestimation of overall compaction. Despite this, the graphs reported in Figures 5.7 and 5.8 make the need to clean creep contribution evident. For NEC 1, 2, 5 and 6 the last sections of the plot cleaned from the creep are slightly upwards: this isn't consistent with reality, but it's still a good overall approximation. The overestimation of the creep effect in the final phase can be caused by the overall uncertainty of the measures or, more probably, by the overestimation of the $C_\alpha H$. The latter can be linked to the lack of more frequent and recent measurements: having a longer and sufficiently extended time series beyond the last loading phase would have made it possible to obtain a more reliable measure of C_α, ensuring that only creep was acting during the interval in which it is calculated. Moreover, it is difficult to precisely determine the time at which the overpressure dissipated t_{ref} based solely on the series of vertical displacements; even more so if it is so sparse over time.

No compensation for the creep contribution was carried out for the DTM at the NEC stations: the measured values are so scattered and with abrupt changes in the latest segments – where the creep would affect most – that the potential change caused by compensating the creep is of little meaning.

Figure 5.9 sums up and highlights changes in NEC values before and after the creep effect removal.

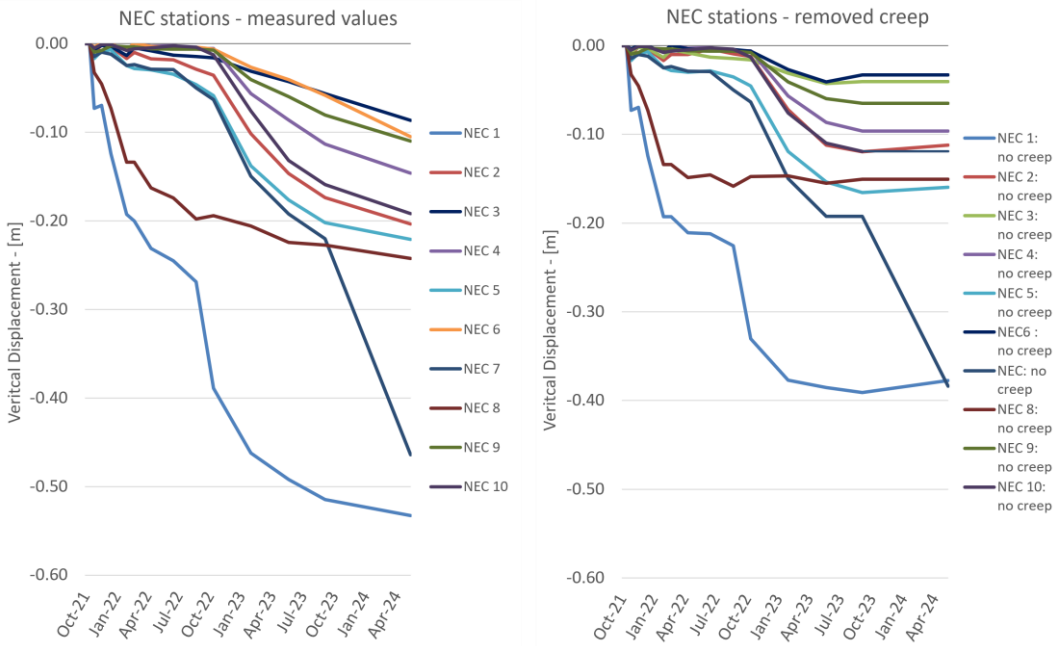

Figure 5.9. Vertical displacement recorded by the NEC stations with and without the creep contribution.

6. NUMERICAL MODELING

Before working on Le Sorelle-B case study, the NATSUB3D capabilities have been tested on a simple saltmarsh model. This has allowed to assess the simulator sensitivity to the main soil parameters and its reliability when using the so called “Restart” feature. Even though the test on Restart looked promising on the simple case some flaws came out while using the restar on Le Sorelle-B model and deeper analysis were carried out before going through the soil parameters calibration process.

6.1. Testing the NATSUB3D capabilities on a simple model

NATSUB3D has been preliminary applied to a simple case to investigate the simulator capabilities to reproduce auto-compaction of sedimentary landforms. The used model was created by the Department of Civil and Environmental Engineering of the University of Padova (Xotta et al., 2022) while developing the simulator itself. This model has same boundary condition and purpose to the present study case and comes handy due to his reduced spatial and temporal dimensions. The simulated domain is 10 × 10 m with a top elevation of 3.8 m and the number of model elements in the domain increases from 60,000 (with 20,402 nodes) at the beginning of the simulation (when only a single FE layer representing the marsh sandy basement composes the mesh) to 2,144,131 (and 362,971 nodes) at t = 3,000 years (Xotta et al., 2022). In contrast, the Le Sorelle-B model lasts for more than 13640 years, it encompasses thousands of m^3 and it ends with more than half million nodes.

The model simulates the evolution of a salt marsh adjacent to a tidal creek under gradual relative sea-level rise (SLR). The simulated domain is the above-mentioned 10 × 10 m square with a spatial discretization of 0.5 meters in both horizontal and

vertical ($\Delta z_{max} = 0.5\ m$) directions. No-flux conditions are applied to the inner lateral and bottom boundaries, with (p = 0) along the creek bank and land surface.

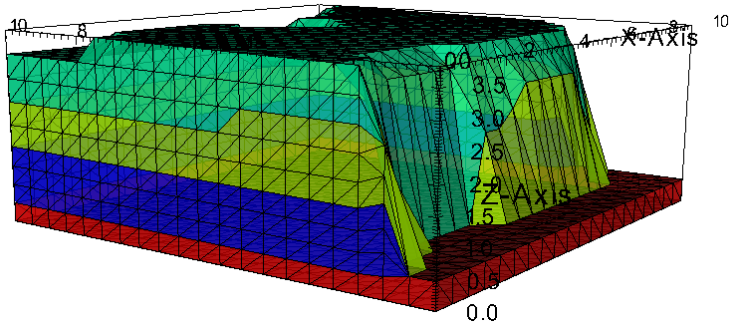

Figure 6.1. Tidal marsh simple case numerical model mesh and materials on Visit.
Starting from the bottom, the stratigraphy is the following: sand, peat, silt and clay.

The simulation covers 3,000 years, with sediment deposition occurring in three phases (Figure 6.2):

1. **Peatland Growth (0-1,000 years)**: Peat accumulates at a rate of 1.5 mm/year on the marsh and 0.15 mm/year in the creek.

2. **Overbank Deposits (1,000-1,500 years)**: Silts are deposited on top of the peat, forming a natural levee next to the creek, simulating increased tidal activity and sediment influx. The deposition rates remain constant at 1.5 mm/year on the marsh and 0.15 mm/year in the creek.

3. **Continued Salt Marsh Growth (2,000-3,000 years)**: The salt marsh continues to grow with the accumulation of finer-grained sediments (clay) and organic matter, simulating a transition to a lower-energy environment. The sedimentation rate is 1.5 mm/year on the salt marsh, except for a central pond where it is reduced to 0.5 mm/year.

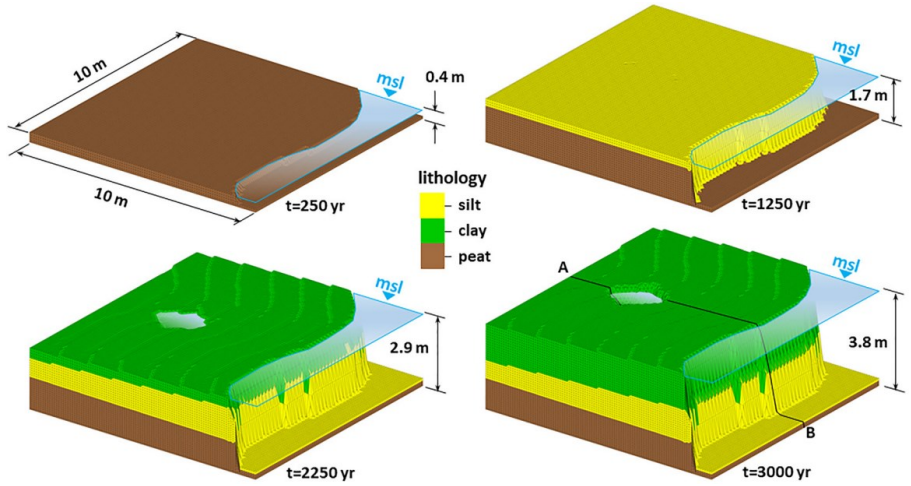

Figure 6.2. Tidal saltmarsh evolution at times 250, 1,250, 2,250, and 3,000 years (Xotta et al., 2022). *The simulated salt marsh borders a tidal creek. The colors represent the different sediment types. Note that in this picture the mesh discretization was 0.1 m ($\Delta z_{max} = 0.1\ m$).*

The main soil geomechanical parameters used as starting values are reported in Table 6-1.

Table 6-1. Initial hydro-geomechanical properties of the lithological classes used in the modelling of tidal saltmarsh (Xotta et al., 2022).

	Soil material	γ_s *[kg/m³]*	e_0 *[-]*	C_c *[-]*	C_r *[-]*	σ_p *[kPa]*	K_{z0} *[m/s]*	$K_{x,y}/K_z$ *[-]*
4	Clay	27	10	3.0	0.1	1.0	1E-09	3.0
3	Silt	27	3.0	0.5	0.05	1.0	1E-07	3.0
2	Peat	20	15	4.0	0.4	1.0	1E-07	3.0
1	Sand	27	1.0	0.2	0.02	1.0	1E-06	3.0

A sensitivity analysis was performed by changing three parameters for the peat layer – C_c, K_x and e_0 – leading to 8 scenarios. The peat layer is chosen because it receives the greater load during the deposition of overlaying strata: variations in its parameters should show greater changes in the tidal marsh behaviour and in the peat layer itself. Node A, see Figure 6.3, corresponding to nore Id=954 was selected to represent the model outcomes in terms of strain and porosity.

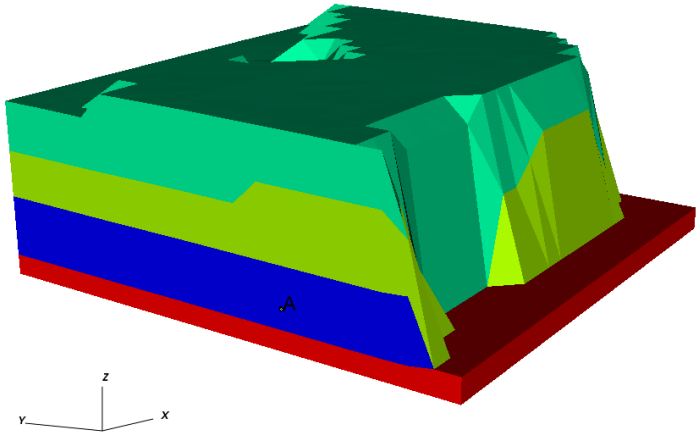

Figure 6.3. A is the node corresponding to the Node ID 954 beloging to the peat layer.
Perspective view of the numerical model in Visit.

6.1.1. Changing the peat compressibility index – C_c

Two simulations were run by dividing or multiplying the initial C_c (Table 6-1) by two:

- $C_{c,1} = 2\ C_c = 8$
- $C_{c,2} = 0.5\ C_c = 2$

Values for resulting time-dependent values of Strain and Porosity at node 954 are reported in Figures 6.4 (a) and (b), respectively.

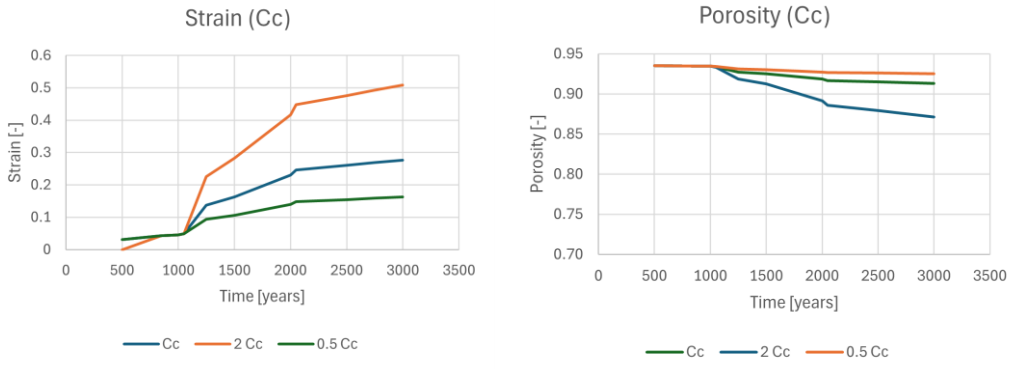

Figure 6.4. Strain (a) and Porosity (b) values at node 954 over time at changing compressibility index C_c for peat.
Strain_0 and Cc curves represent the strain values obtained with default values (Table 6-1).

From 500 to 1050 years curves are overlapped underlining no significant effect on Strain and Porosity due to the change of C_c. At 1250 years silt begins to deposit on the peat layer. The silt is characterized by the same γ_s as the peat but e_0 is 5 times lower (i.e., lower porosity and higher bulk density), therefore causing an increase in load that begins to highlight how porosity and deformation are influenced by the coefficient C_c. In other terms, the geostatic load caused by the silt deposition, triggers the C_c-related change in time derivative for strain and porosity functions.

6.1.2. Changing the peat void index – e_0

Similarly, the starting void index has been changed to eventually observe how it affects Strain and Porosity at node 954:

- $e_{0,1} = 0.5\ e_0 = 7.5$
- $e_{0,2} = {}^{2}/_{3}\ e_0 = 10$
- $e_{0,3} = {}^{4}/_{3}\ e_0 = 20$

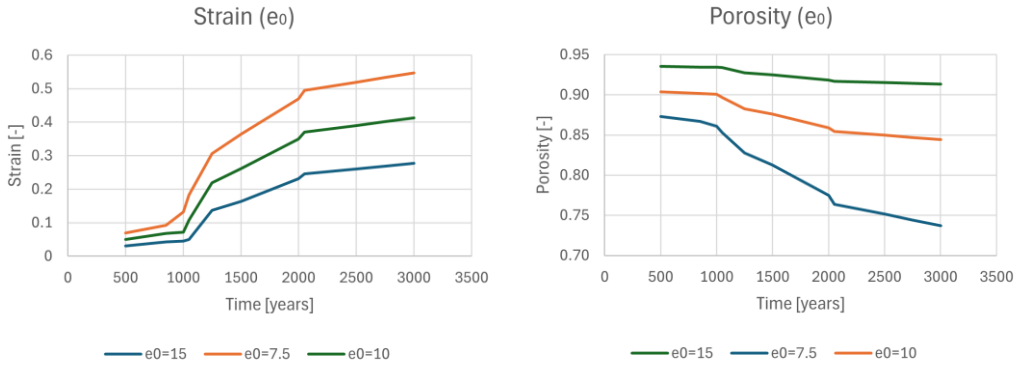

Figure 6.5. Strain (a) and Porosity (b) values at node 954 over time at changing void index e_0 for peat.

As shown in Figure 6.5, contrary to previous results, the variation in strain and porosity resulting from the modification of e_0 is immediately visible. However, in this case as well, the application of subsequent load accentuates the difference between the curves.

6.1.3. Changing the peat void index – K_z

The last soil mechanical parameter that has been changed to check the simulator sensitivity is K_z.

- $K_{z,1} = 0.01\ K_z = 10^{-9}$ m/s
- $K_{z,2} = 0.1\ K_z = 10^{-8}$ m/s
- $K_{z,3} = 10\ K_z = 10^{-6}$ m/s

Note that the first two values are not typically assigned to a peaty soil.

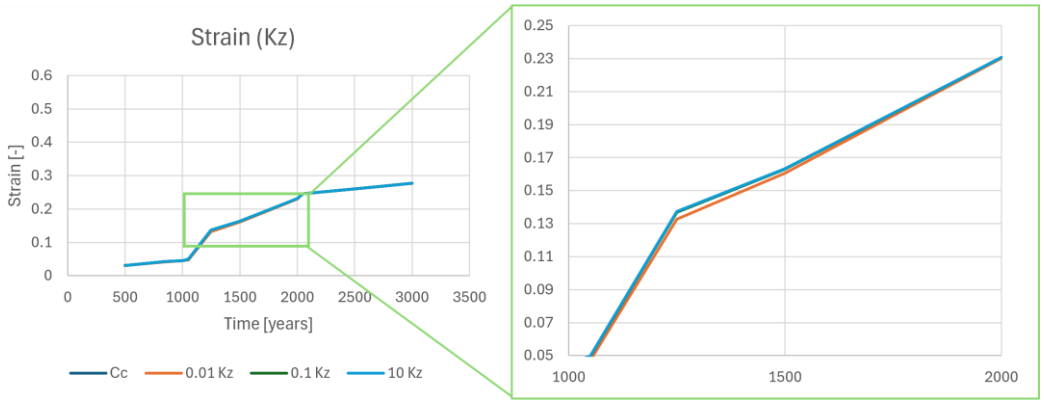

Figure 6.6. Strain values at node 954 over time at changing hydraulic conductivy K_z for peat.
The graph on the right is a close up of the period between 1000 and 1500 years of the main graph to highlight the little variation of strain occurring.

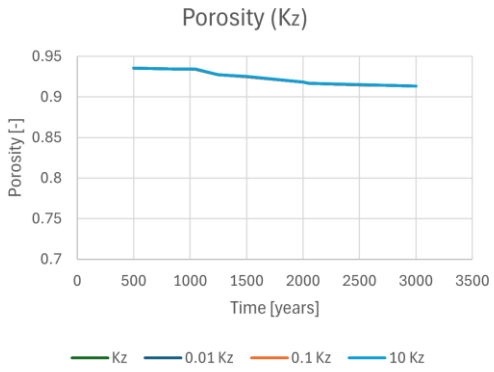

Figure 6.7. Porosity values at node 954 over time at changing hydraulic conductivy K_z for peat.

A very little effect of the change of K_z on strain is noticeable in the close up in Figure 6.6. This represents the delay for the dissipation of the overpressure caused

during the deposition of the heavier silt; once the overpressure is completely neutralized, the strain curve for $K_z = 10^{-9}$ m/s reallineates with the other ones.

Considering the model tolerance, no change at all is noticed for porosity (Figure 6.7).

To provide a comprehensive overview of the above sensitivity analysis, graphs collecting all strain and porosity curves are reported in Figrue 6.8 and 6.9.

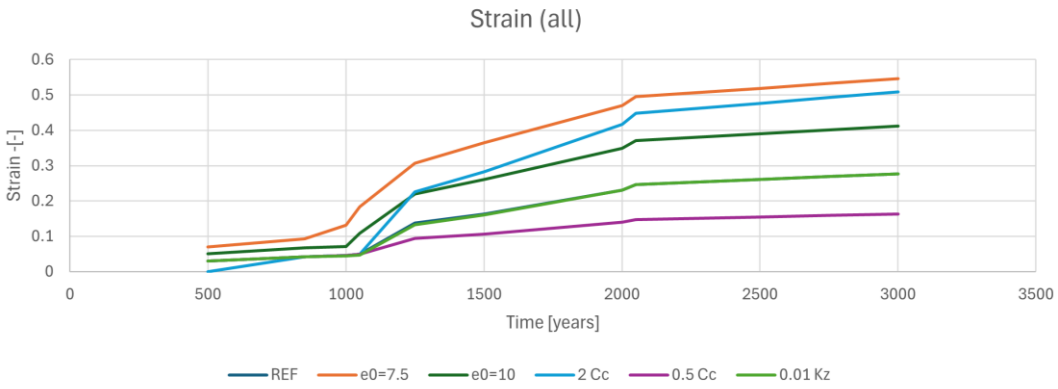

Figure 6.8. Strain curves relative to different C_c, e_0 and K_z.
Curves for $K_z = 10^{-8}\ m/s$ and $K_z = 10^{-6}\ m/s$ are not reported since they completely overlapped the reference curve obtained with default values (Table 6-1).

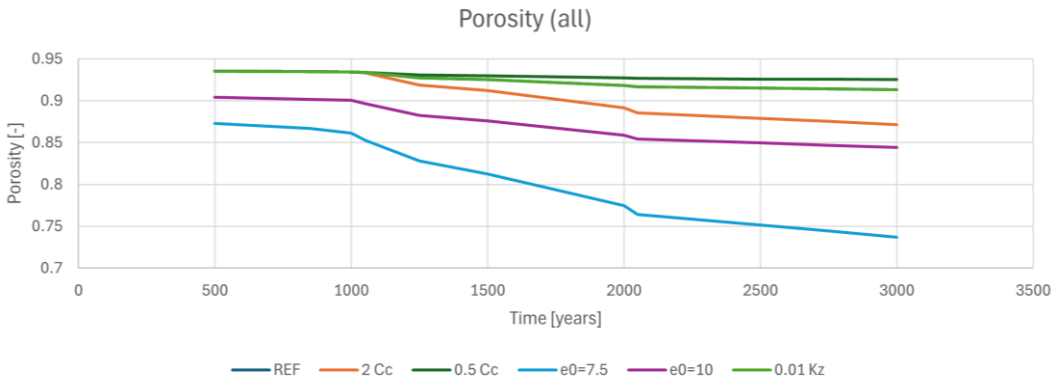

Figure 6.9. Porosity curves relative to different C_c, e_0 and K_z.
Curves for $K_z = 10^{-8}\ m/s$ and $K_z = 10^{-6}\ m/s$ are not reported since they completely overlapped the reference curve obtained with default values (Table 6-1).

6.2. Preliminary model of Le Sorelle-B

A simulation of the saltmarsh model was run with the initial values (Table 4-1) and its results are hereby discussed recalling that the soil is fully saturated and the boundary conditions described in Paragraph 4.2 impose an impermeable basement, no-flow lateral boundaries (Neumann condition) and hydrostatic pressure at top (null Dirichlet condition). The subsurface model evolution is reported in Figure 6.10 every time a new material layer is completely formed.

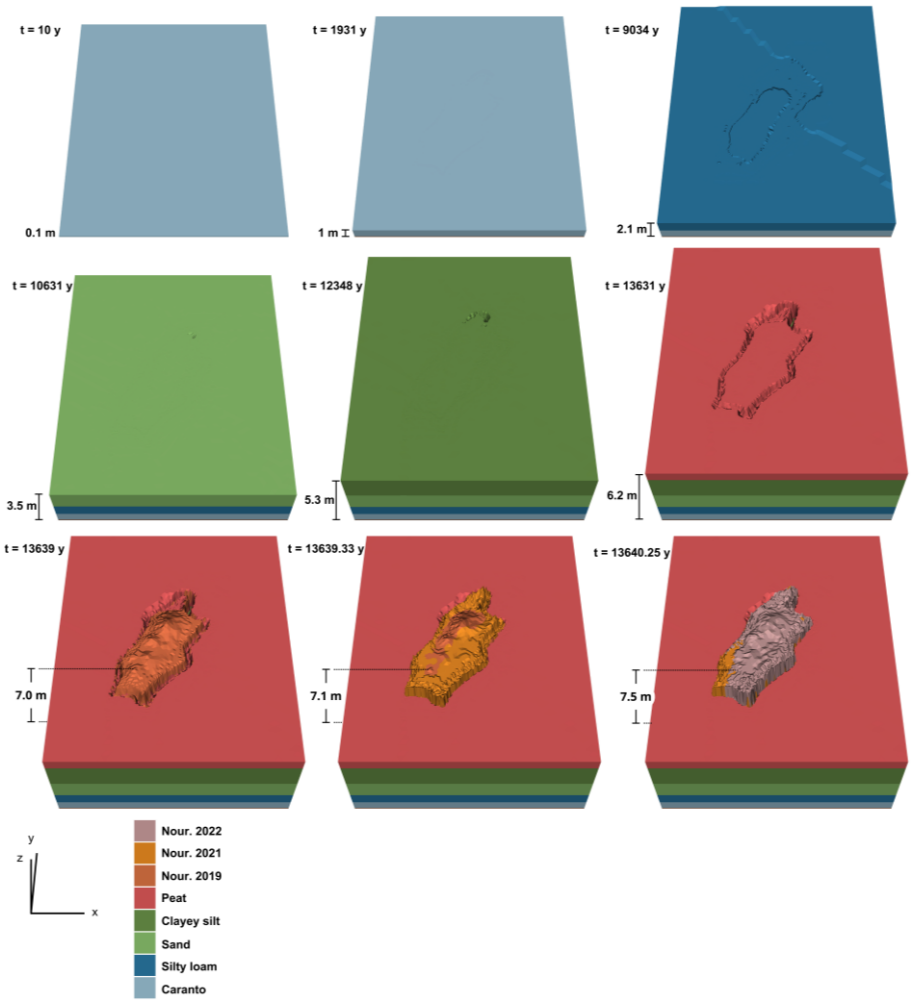

Figure 6.10. Evolution of the Venice Lagoon subsurface at Le Sorelle-B site.
Vertical exageration is 5.

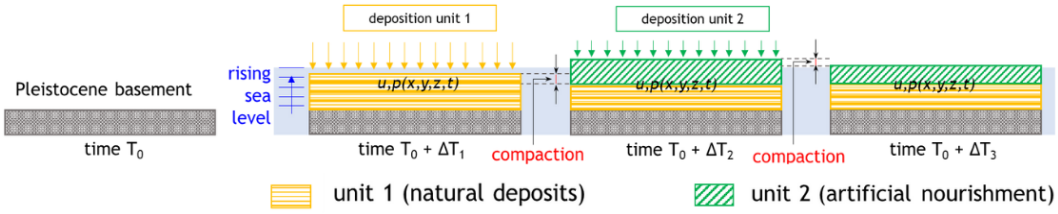

Figure 6.11. Sketch of the processes addressed by the NATSUB3D.

Figure 6.11 schematically represents the process addressed by the NATSUB3D simulator for Le Sorelle-B saltmarsh evolution and Table 6-2 reports the correlation between actual years and dates and simulation time

Table 6-2. Correlation between real and modelled time milestones.
(*) Material deposition time is reffered to when it is completed; (**) is the Present time reference. Colour shadings mark milestones (e.g., NEC measurements) from different years.

Mat. deposition, NEC or ***nourishment***	*Output N°*	*Date*	*Δt* [gg]	[mm]	[yy]	T_{sim} *[y]*
-	1	~ 13'642 y BP	-	-	0	0
*Caranto**	3	~ 11'711 y BP	-	-	1931	1931
*Silty loam**	11	~ 4'608 y BP	-	-	7103	9034
*Sand**	13	~ 3'011 y BP	-	-	1597	10631
*Clayey silt**	16	~ 1'294 y BP	-	-	1807	12348
*Peat**	22	~ 11 y BP	-	-	1193	13631
1° nour. - start	22	~ 11 y BP	-	-	0	13631
1° nour - end	28	~ 5 y BP	-	-	6	13637
2° nour. - start	30	01/09/2021			2	13639.00
	31	01/10/2021	30	0.986	0.082	13639.08
1	32	14/10/2021	13	0.427	0.036	13639.12
2	33	28/10/2021	14	0.460	0.038	13639.16
	34	01/11/2021	4	0.132	0.011	13639.17
3	35	18/11/2021	17	0.559	0.047	13639.21
	36	01/12/2021	13	0.427	0.036	13639.25
4	37	16/12/2021	15	0.493	0.041	13639.29
2° nour. - end	38	31/12/2021	15	0.493	0.041	13639.33
5	39	31/01/2022	31	1.019	0.085	13639.42
6	40	22/02/2022	22	0.723	0.060	13639.48
	41	01/03/2022	7	0.230	0.019	13639.50
	42	01/04/2022	31	1.019	0.085	13639.58
7	43	12/04/2022	11	0.362	0.030	13639.61
	44	01/05/2022	19	0.625	0.052	13639.66

Mat. deposition, NEC or ***nourishment***	*Output N°*	*Date*		*Δt*		T_{sim} *[y]*
	45	01/06/2022	31	1.019	0.085	13639.75
8	46	17/06/2022	16	0.526	0.044	13639.79
	47	01/07/2022	14	0.460	0.038	13639.83
	48	01/08/2022	31	1.019	0.085	13639.92
9	49	23/08/2022	22	0.723	0.060	13639.98
	50	01/09/2022	9	0.296	0.025	13640.00
3° nour. - start	51	01/10/2022	30	0.986	0.082	13640.08
10	52	13/10/2022	12	0.395	0.033	13640.12
	53	01/11/2022	19	0.625	0.052	13640.17
3° nour. - end	54	30/11/2022	29	0.953	0.079	13640.25
11	55	31/01/2023	62	2.038	0.170	13640.42
	56	01/03/2023	29	0.953	0.079	13640.50
	57	01/04/2023	31	1.019	0.085	13640.58
	58	01/05/2023	30	0.986	0.082	13640.66
12	59	22/05/2023	21	0.690	0.058	13640.72
	60	01/06/2023	10	0.329	0.027	13640.75
	61	01/07/2023	30	0.986	0.082	13640.83
	62	01/08/2023	31	1.019	0.085	13640.92
	63	01/09/2023	31	1.019	0.085	13641.00
13	64	05/09/2023	4	0.132	0.011	13641.01
	65	01/10/2023	26	0.855	0.071	13641.08
	66	01/11/2023	31	1.019	0.085	13641.17
	67	01/12/2023	30	0.986	0.082	13641.25
	68	01/01/2024	31	1.019	0.085	13641.33
	69	01/02/2024	31	1.019	0.085	13641.42
	70	01/03/2024	29	0.953	0.079	13641.50
	71	01/04/2024	31	1.019	0.085	13641.58
	72	01/05/2024	30	0.986	0.082	13641.67
14	73	13/05/2024	12	0.395	0.033	13641.70
	74	01/06/2024	19	0.625	0.052	13641.75
	75	01/07/2024	30	0.986	0.082	13641.83
	76	01/08/2024	31	1.019	0.085	13641.92
	77	01/09/2024	31	1.019	0.085	13642.00
	78	01/10/2024	30	0.986	0.082	13642.08
	79	01/11/2024	31	1.019	0.085	13642.17
	80	*01/12/2024**	*30*	*0.986*	*0.082*	*13642.25*
	81	01/01/2025	31	1.019	0.085	13642.34

Table 6-2 presents the correlation between the simulated years in the numerical model and the corresponding real-world dates for the evolution of the artificial salt marsh Le Sorelle-B.

To better visualize the stratigraphy and the properties of subsurface layers a section A-A’ was performed (Figure 6.12). It crosses the center of the East-West extention and parallel to the North-South direction.

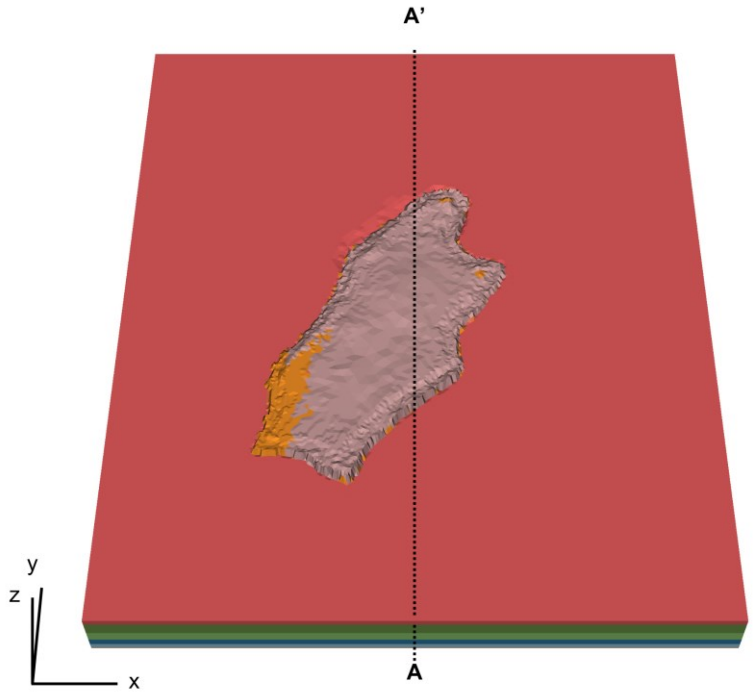

Figure 6.12. South-North central section A-A' at the end of the 2022 Nourishment deposition 13640.25 y.

Relative to this section, stratigraphy, mesh, strain, compactin, elevation, stress and pressure at the very end of the 2022 nourishment (simulation time 13640.25 y) are reported in Figures from 6.13 to 6.20. Pressure values for section A-A’ at time 13640.12 y are also reported because it is peak-pressure-values condition for 2022 nourishment.

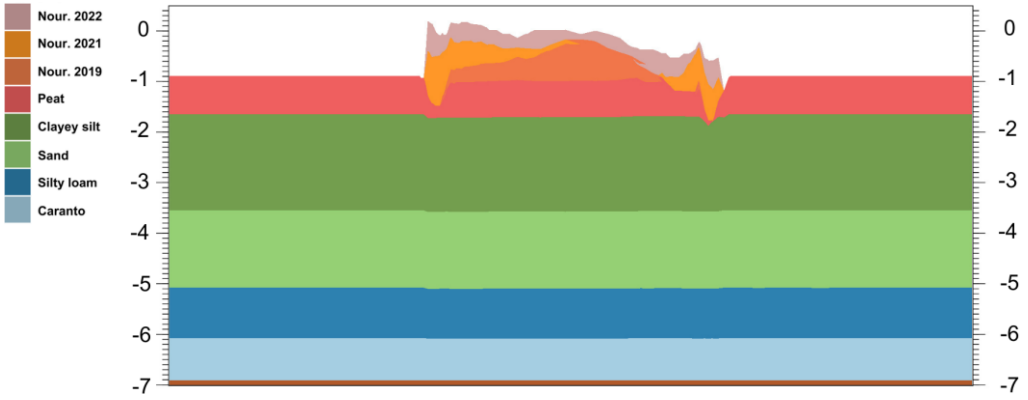

Figure 6.13. Stratigraphy along Section A-A' (left-right) at the end the 2022 nourishment (13640.25 y).
Vertical exaggeration is 5.

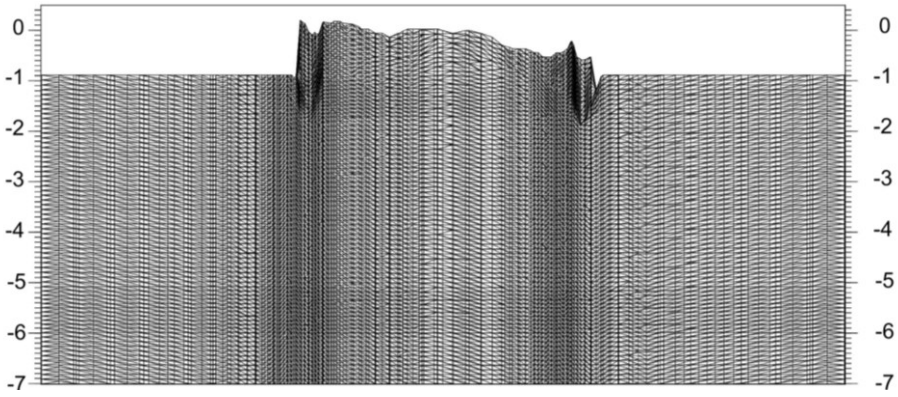

Figure 6.14. Mesh along Section A-A' (left-right) at the end of the 2022 nourishment (13640.25 y).
Vertical exaggeration is 5.

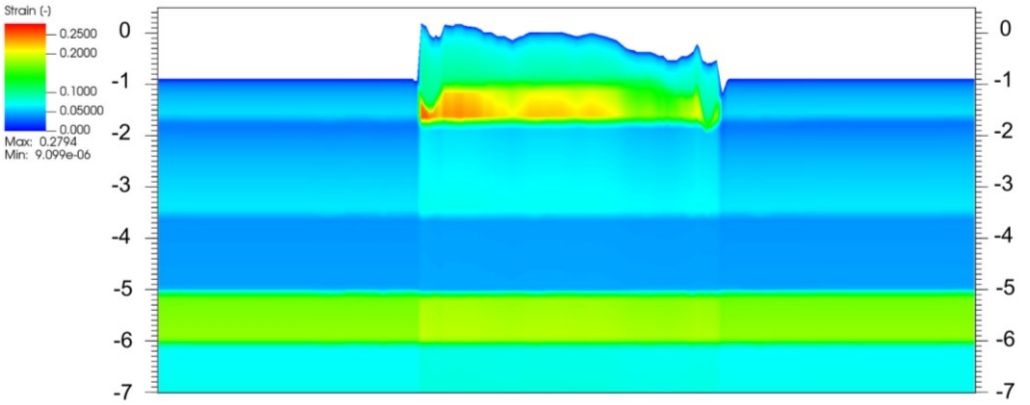

Figure 6.15. Strain [-] values along Section A-A' (left-right) at the end of the 2022 nourishment (13640.25 y).
Vertical exaggeration is 5.

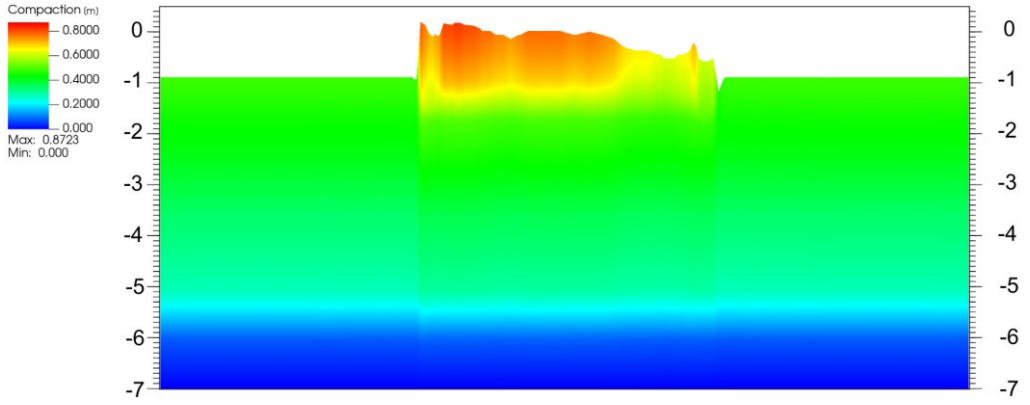

Figure 6.16. Compaction [-] along Section A-A' (left-right) at the end of the 2022 nourishment (13640.25y).
Vertical exaggeration is 5.

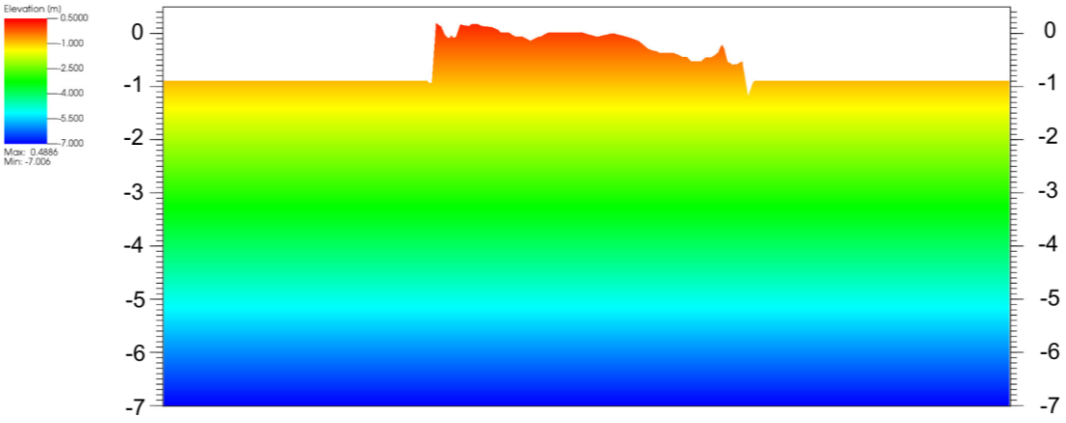

Figure 6.17. Elevation [m] along Section A-A' (left-right) at the end of the 2022 nourishment (13640.25 y).
Vertical exaggeration is 5.

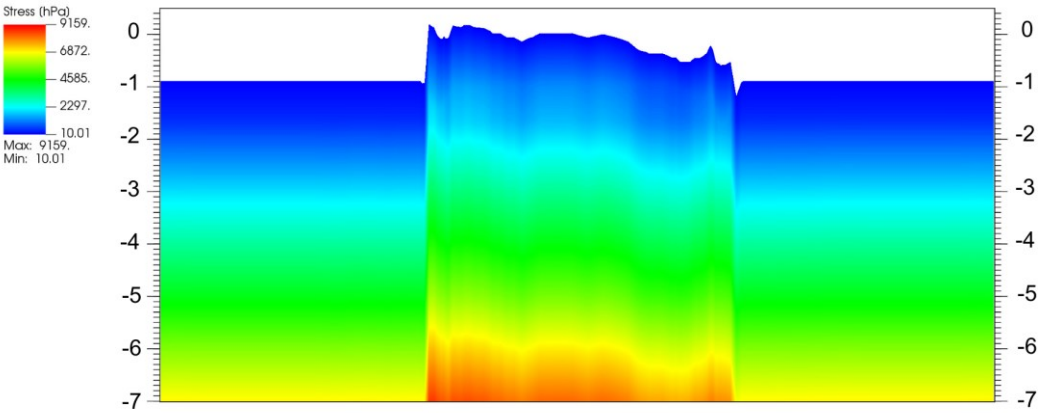

Figure 6.18. Stress [Pa] along Section A-A' (left-right) at the end of the 2022 nourishment (13640.25 y).

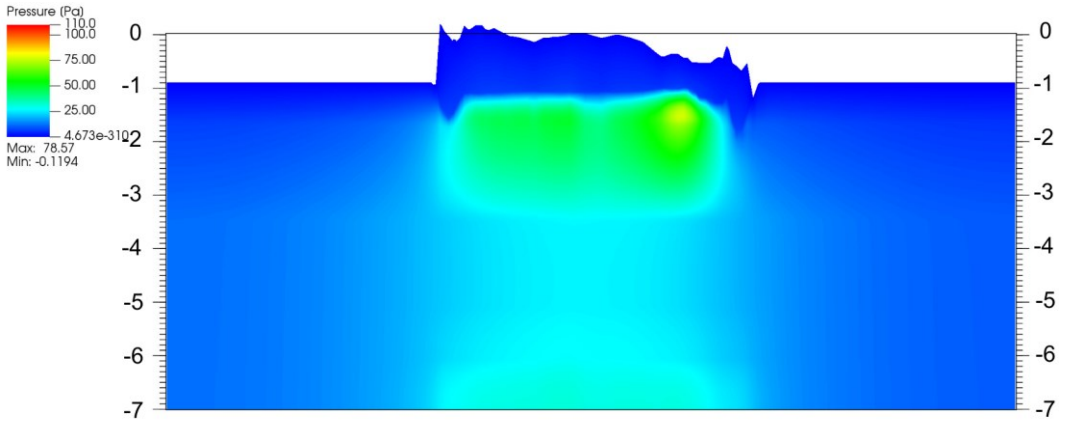

Figure 6.19. Pressure [Pa] along Section A-A' (left-right) at the end of the 2022 nourishment (13640.25 y).

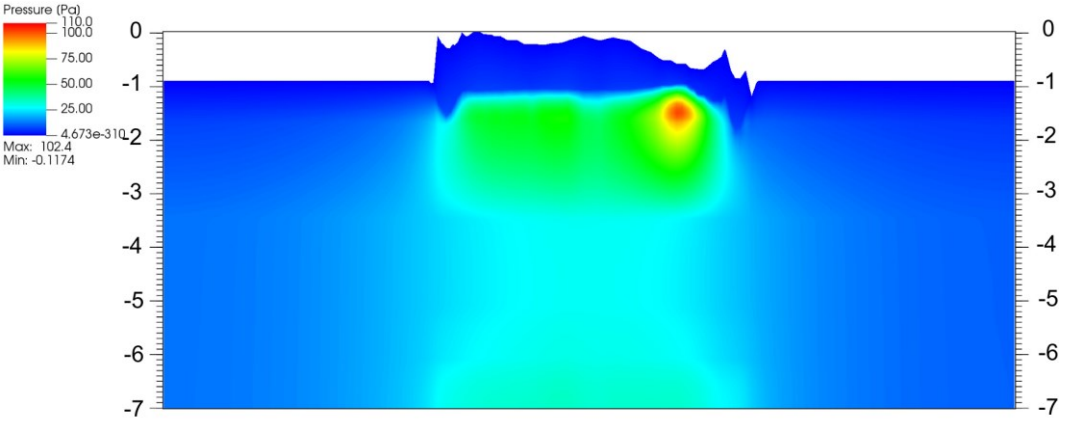

Figure 6.20. Pressure [Pa] values along Section A-A' (left-right) one month before the end of the 2022 nourishment (13640.12 y).
Vertical exaggeration is 5.

As anticipated in Paragraph 3.2, the stress within the simulated domain increases from top to bottom (Figure 6.18) because the soil grains must support a geostatic load that intensifies with depth. According to Terzaghi's principle, the time-dependent dissipation of overpressure (Figure 6.19 and 6.20) caused by autocompaction can delay the transfer of the total stress (i.e., the geostatic load) from the pore water to the grain contacts (i.e., the effective stress). Higher values for ovepressure are located below the zone where more sediment is deposited by the 2022 nourishment. It can also be said that, as expected, following new sedimentation, overpressure develops mostly within peat and clayey silt layers in

the areas that are immediately below the surface of the artificial salt marsh. The peat layer is also broadly affected in terms of strain.

The upper-surface elevation of the model before the 2021 nourishment is compared to the bathymetries provided by the Geomatics group of Dept. ICEA (Figure 6.24). NECs position are reported as well.

6.3. Use of the restart feature for Le Sorelle-B numerical model

The restart was typically used to run the simulation after the two years pause following the first nourishment in order to easily compare the modelled bathymetry with the Port Authority one and to run simulations just for the last two nourishments and beyond. Hence, the model inputs for the restart cover the first 13639 years while the consequent one the last 3.34 years – from 13639 to 13642.34 years – ending at the 31-th December 2024.

Unfortunately, while comparing the model results with the NECs records some discrepancies between the simulations that started from 0 and those who used the advanced configuration showed up. Firstly, a lower subsidences was noticed in the shallower layer in simulations computed with the restart option, inducing a significant underestimation of the artificial saltmarsh surface elevation. Then, it was noticed that the restart induced a reduction in the bulk compressibility c_b of strata belonging to the input model causing to use a stiffening of the geological soil and first nourishment (2019) strata.

To prove this, elements in the middle of each soil layer on the vertical alignment below the NEC 2 were identified (Figure 6.21), and their values over time of c_b were compared between the complete simulation and the “restarted” from year

13639 till the end (Figure 6.22). The elements were investigated instead of the nodes because c_b is an elemental property.

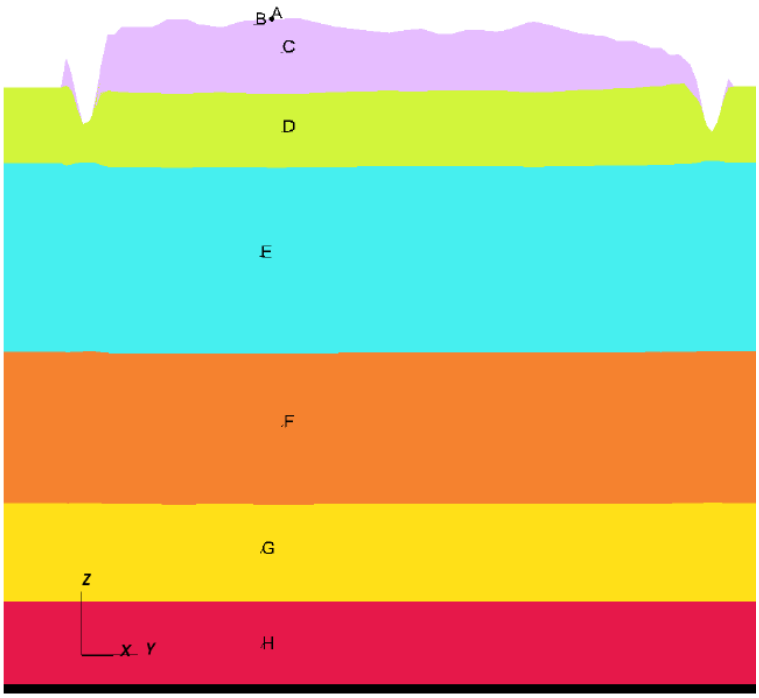

Figure 6.21. Section AA' entangling the position corresponding to NEC 2 (A) and the elements underneath it, from B to H.
The colors represent the different sediment types. Vertical exaggeration is 10.

The curves showing how bulk compressibility (c_b) varies over time for each element distinguishing the values with and without restart are reported top to bottom starting from the saltmarsh surface.

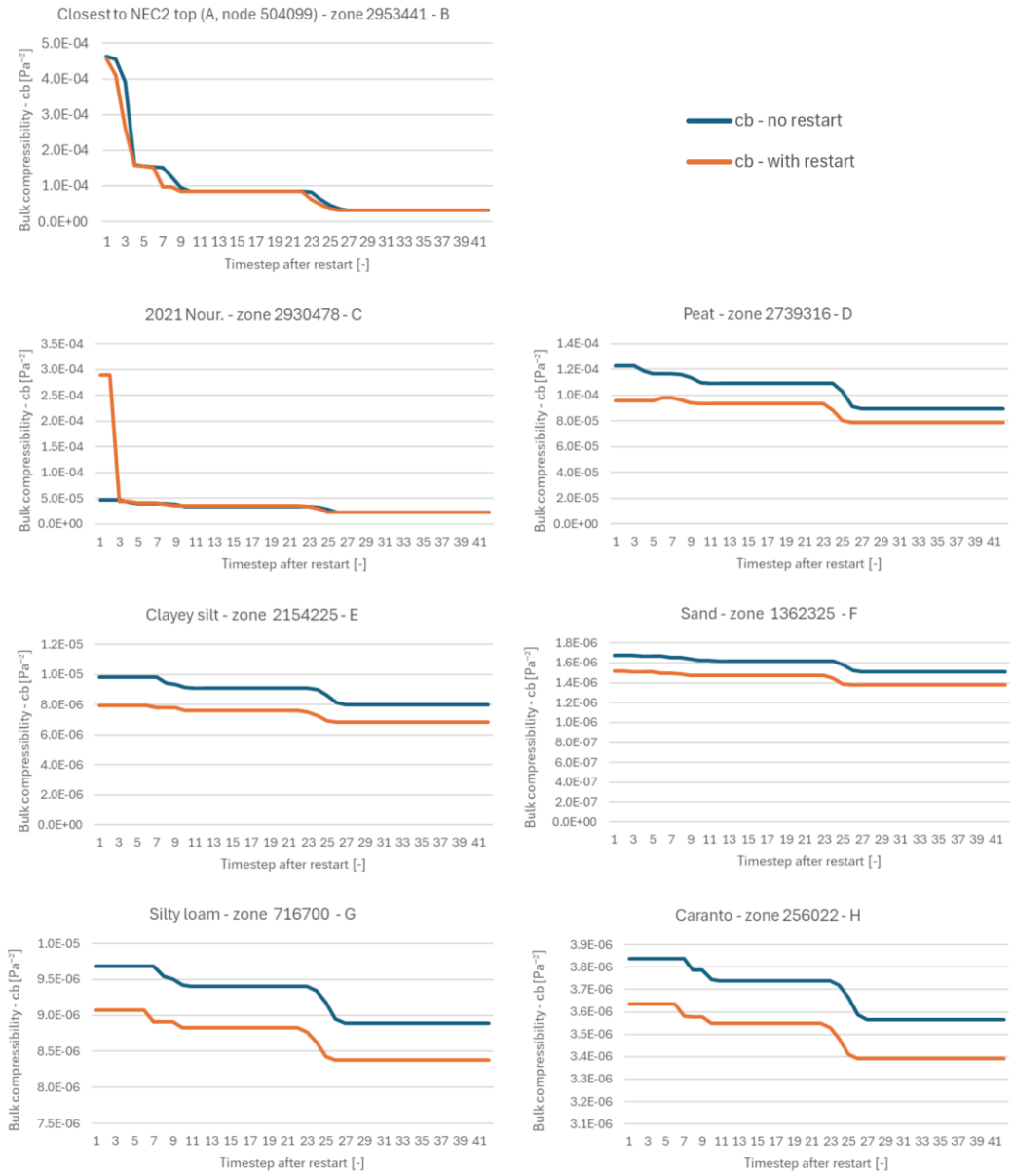

Figure 6.22. Bulk compressibility at the center of each material stratum beneath the NEC 2 station.

Note that the scale of the vertical axis differs picture by picture to better depict the different values. Although the absolute difference between bulk compressibilities with and without restart seems relatively small, the relative difference is not negligible (Figure 6.23). Table 6-2 reports the percentages relative to the maximum, minimum and average value along with the standard deviation for each element.

This was done starting from timestep 3, since in the very first timesteps the model recalculates some properties including c_b.

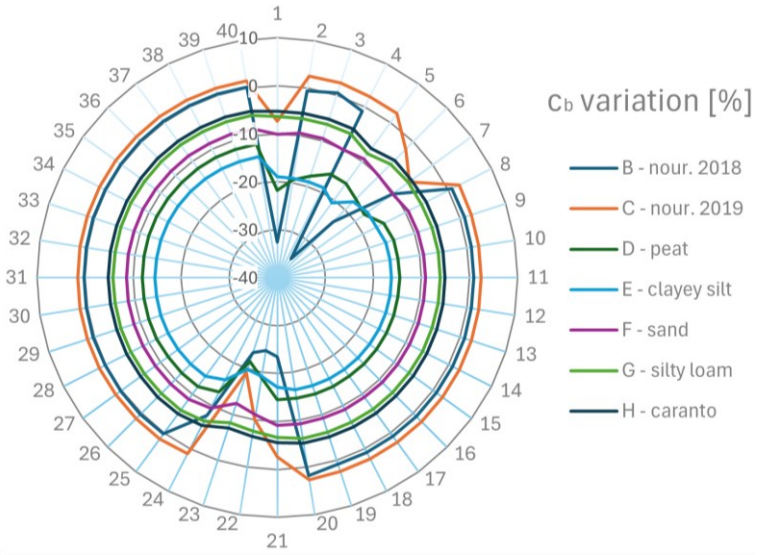

Figure 6.23. Percentage variation between model computed with and without the restart at elements under NEC 2.

Table 6-3. Maximum, minimum and average percentage variation while using the restart feature for aech element considered.

	B nour. 2019	***C nour. 2019***	***D peat***	***E clayey silt***	***F sand***	***G silty loam***	***H caranto***
Max [%]	1.81	2.66	-11.86	-14.54	-8.61	-5.78	-4.83
Min [%]	-35.17	-19.21	-21.77	-20.72	-12.41	-8.20	-6.97
avg [%]	-4.13	0.51	-14.31	-16.21	-9.20	-6.18	-5.16
Avg var.	7.40	2.53	2.01	1.34	0.50	0.37	0.32

The most affected layers are the peat and clayey silt units, which are the shallowest, and peat is the thickest as well. The latter fact worsens the overall underestimation of the saltmarsh compaction since it makes the layer more susceptible to consolidation when nourishments are deployed. The deeper layers already faced most of the total load in previous phases.

Due to this flaw and despite the higher computational cost, all following simulations were run from time 0, i.e. comprising the whole Holocene period.

6.4. Le Sorelle-B model calibration and validation using the NEC records

The simulation results were initially compared with the NEC records as anticipated in Paragraph 5.2.1. Then, to better match the real evolution of the saltmarsh, the void index and the compressibility index of some soil materials were calibrated.

6.4.1. NEC displacement as model results

Comparing the NEC records with the model results required to identify the nodes representing the NEC plates in the model outputs which came as vtk (Visualization ToolKit) files. A python script enabled the identification of these nodes and then the plotting of their elevation values over time by which the displacements were computed.

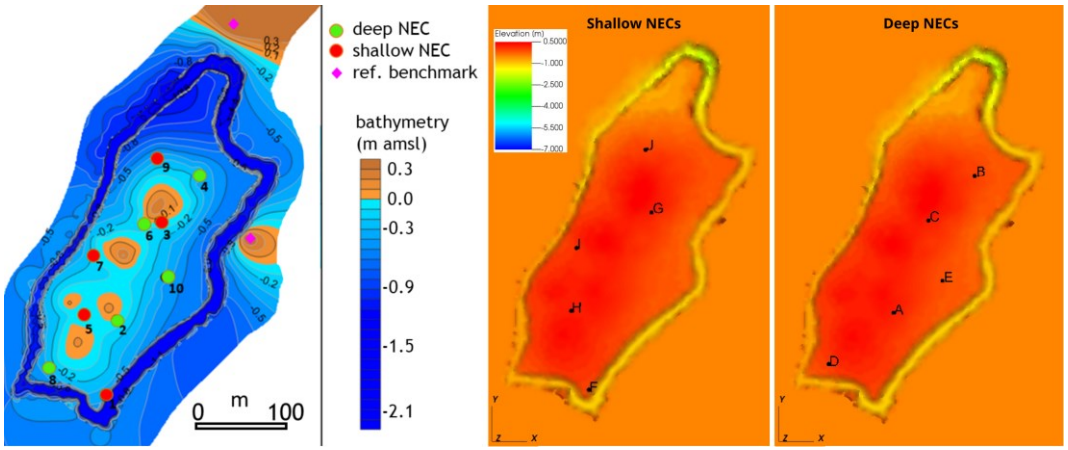

Figure 6.24. NECs position in the numerical model and in the UniPD bathymetry before the 2021 nourishment.

Note that the nodes for deep NECs shown in Figure 6.24 are not the actual nodes since deep NECs are 1 m below the surface. The differences between the position

of NECs as model nodes and the actual station are reported in Table 6-3 while the planar distance in Figure 6.25.

Table 6-4. Differences between the position of NECs as model nodes and the actual station and planar distance d.

NEC	*1*	*2*	*3*	*4*	*5*	*6*	*7*	*8*	*9*	*10*
Δx [m]	0.08	-0.19	0.13	-0.01	0.10	0.59	0.13	0.16	-0.05	0.04
Δy [m]	0.17	0.55	0.17	-0.19	0.02	0.15	0.17	0.02	0.24	-0.26
d [m]	0.19	0.58	0.21	0.19	0.10	0.61	0.21	0.16	0.25	0.27

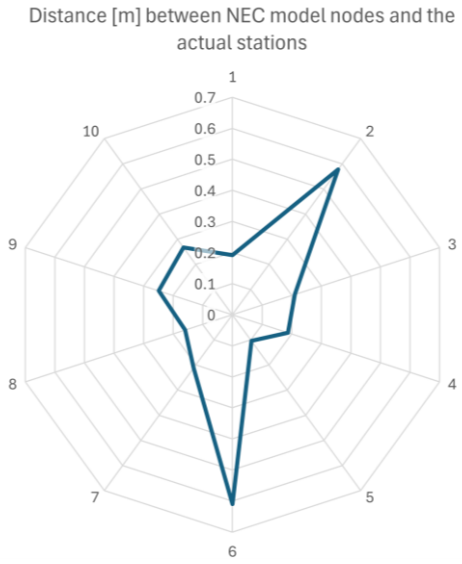

Figure 6.25. Planar distance in meters between the NEC nodes in the model and the actual NEC stations.

NEC 2 and NEC 6 nodes are the only ones that exceed a distance of ~ 25 cm, reaching 58 and 61 cm. Therefore, the distance between NEC nodes and actual NEC stations is considered sufficiently low to provide consistent values for the NEC displacements in the model. The latters are reported in Figure 6.26 and are obtained by running the simulation with the initial geomechanical values (Table 4-1).

Figure 6.26. Comparison among elevation changes at the NEC node, presenting three distinct data sets: actual observed measurements, creep-cleaned observed measurements, and initial-value numerical model predictions.

Although the numerical results for some NECs are sufficiently well matching the observed measurements cleaned from the secondary consolidation (e.g., NECs 3, 6 and 9), there's a general underestimation of compaction especially where cumulative subsidence is higher (e.g., NEC 1). Actually, this could also be caused by the uncertainity of nourishment maps depicting the amount of sediment in the zones around the NECs. In this context, it is woth noting that the last two nourishment maps were obtained from maps derived from datasets acquired several months apart.

6.4.2. Model calibration – e_0 of the last two nourishments

The void index was adjusted for the last two nourishments to determine if the geostatic load they conveyed was consistent with the displacements observed at NEC stations. Recalling the initial $e_0 = 10$ value for all nourishement materials three simulations were run with different e_0 and compared with the default model and NECs records to assess its influence:

A. $e_0 = 10$ for Nour. 2021 and $e_0 = 8$ Nour. 2022;
B. $e_0 = 8$ for Nour. 2021 and 2022;
C. $e_0 = 7$ for Nour. 2021 and 2022.

The displacement values for each NEC node and simulation are reported in Figures 6.27 along the observed measurements cleaned and not cleaned from the secondary compaction.

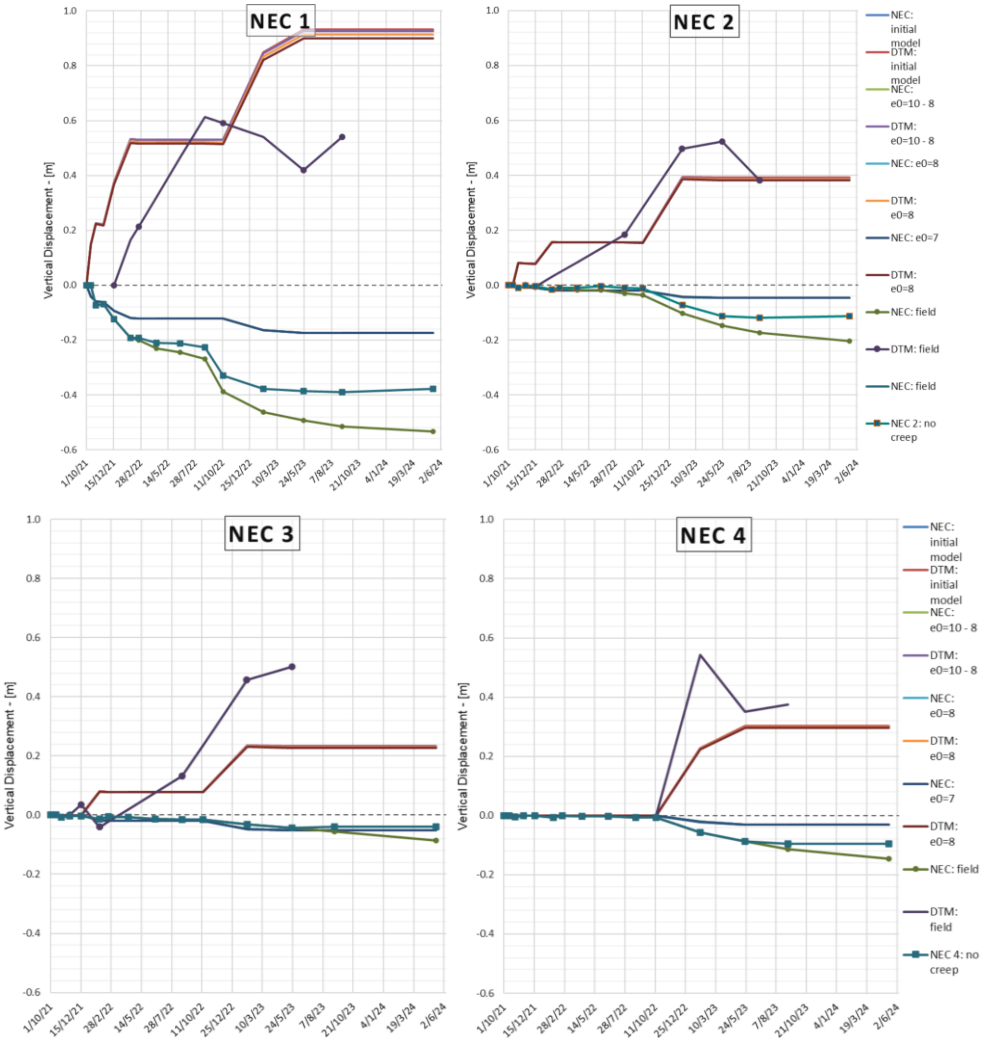

Figure 6.27. e_0 calibration results for displacements at NEC stations from 1 to 4 from compared with actual records and creep-cleaned records.

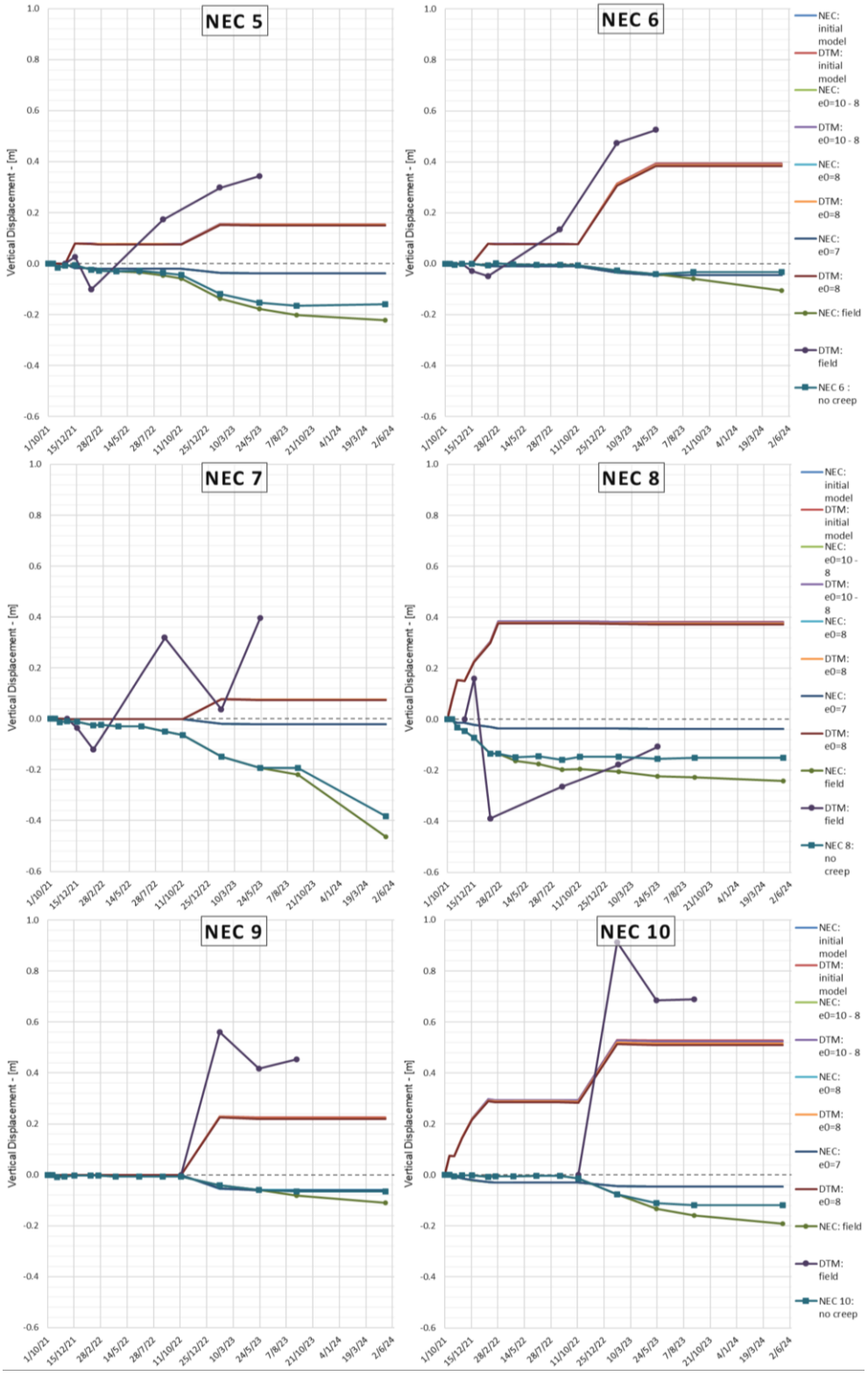

Figure 6.28. e_0 calibration results for displacements at NEC stations from 4 to 10 from compared with actual records and creep-cleaned records.

It is quite evident that there is little o no variation at all between displacement at NEC nodes as e_0 changes. A slight shift is observed only for the DTM curves when the imposed load increases as e_0 lowers. This is attributable to the fact that these are nodes on the surface of the marshland, whose subsidence is the sum of the subsidence of all the underlying layers, including those of the reclamations. The latter are characterized by loose materials with minimal preconsolidation - practically none in reality, but the model requires a value greater than zero, however small.

6.4.3. Model calibration – C_c of peat and 2019 nourishment strata

Since no relevant change occurred by varying e_0, the compressibility index C_c was modified for peat and the 2019 nourishment, although it was preferable to keep the original values of the geological formation unchanged from the default configuration (Table 4-1). This is because these values are obtained by decompacting the soil strata by means of numerical simulations previous to this work.

Recalling the initial C_c values for peat and 2019 nourishment materials $C_c = 2.4$ and $C_c = 0.5$ respectively, a simulation was runned for each of the following C_c combination:

A. $C_c = 8$ for the peat and no change for the 2019 nourishment;
B. $C_c = 3$ for the 2019 nourishment and no change for the peat;
C. $C_c = 8$ for the peat and $C_c = 3$ for the 2019 nourishment.

As for the calibration of e_0, the vertical displacement values for each NEC node and simulation are reported in Figures 6.29 and 6.30 along the actual measured values with and without the creep compensation.

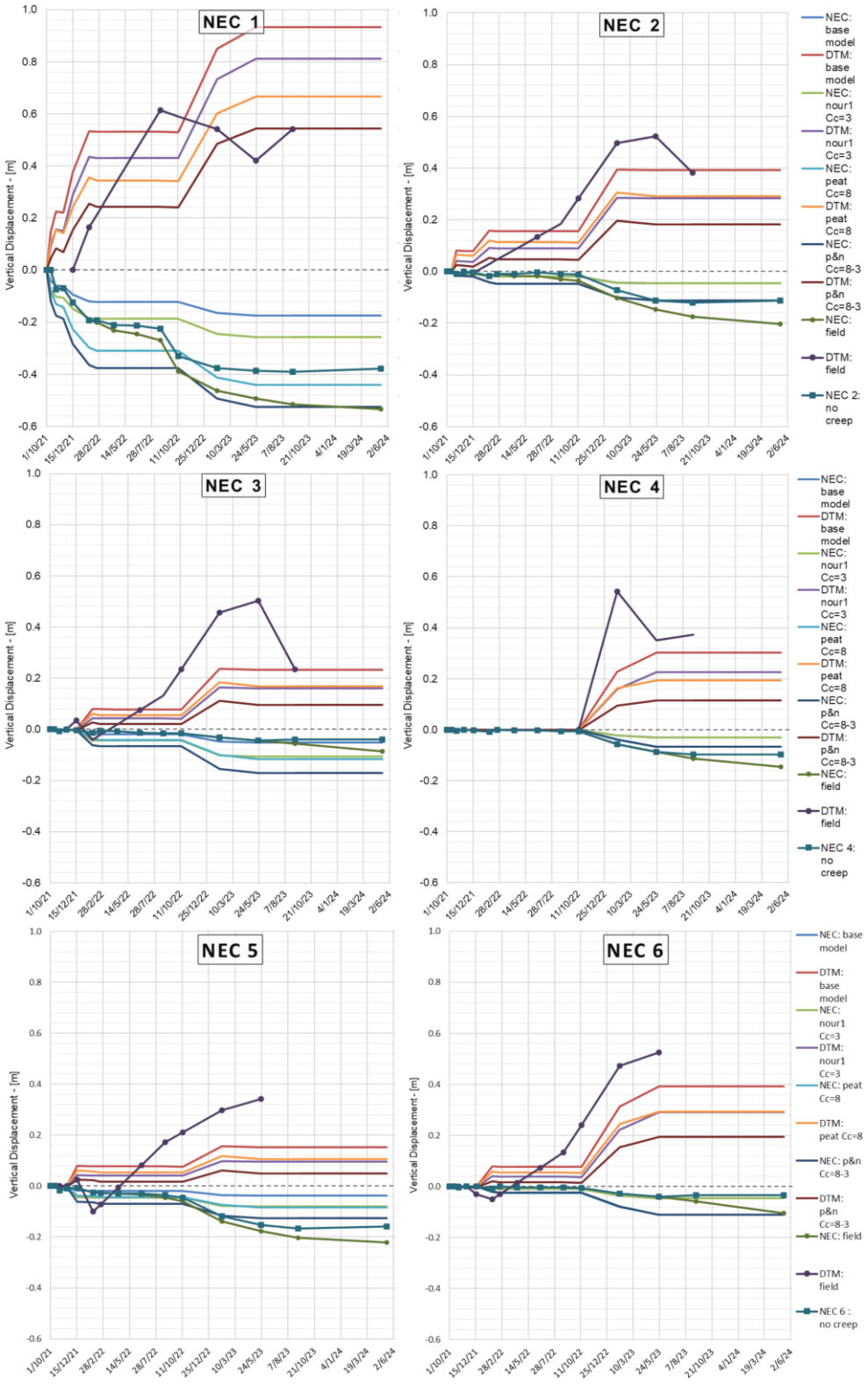

Figure 6.29. Cc calibration results for displacements at NEC stations from 1 to 6 compared with actual records and creep-cleaned records.

Figure 6.30. Cc calibration results for displacements at NEC stations from 7 to 10 compared with actual records and creep-cleaned records.

6.4.4. Choosing the new model after calibration

Among the above tested models, the simulation run with $C_c = 8$ for the peat no change for the 2019 nourishment is chosen as best fitting. The procedure by which it was determined is briefly described.

The Minimum Square Error (MSE) method was implemented to compare the models results with the NEC records once cleaned by the creep as described in Paragraph 6.3.1. MSE consist in averaging square of the differences between these two values for each time:

$$MSE = \frac{1}{n}\sum_{i=1}^{n}\left(Y_i - \widehat{Y}_i\right)^2$$

where

- n is the number of points in the data set
- Y_i are the observed measurement values
- $\widehat{Y}_i$ are the predicted values

Once computed the MSE value for each of 10 NEC record at a given model, the sum up of these MSE values was compared among the calibrated models. Results are reported in Table 6.5 along with the MSE for the DMT nodes computed as for NEC records.

Table 6-5. Sum of all MSE computed for each NEC and model along with the percentage variation respect to the "best-fitting" model (*).

	Initial model		***2019 Nour.: Cc=3***		***Peat: Cc=8 (*)***		***Peat: Cc=8 & 2019 Nour.: Cc=3***	
	NECs	*DTMs*	***NECs***	*DTMs*	***NECs***	*DTMs*	***NECs***	*DTMs*
$\sum MSE_i$	0.052	0.625	0.038	0.593	0.032	0.607	0.050	0.699
%Δ	61.1%	2.9%	16.5%	-2.3%	0.0%	0.0%	54.5%	15.2%

The modelled NEC records resulting from the e_0 calibration were not analysed with this method since none of them sufficiently differ from the initial model. Figures 6.31 and 6.32 reports the comparison between NEC and DTM actual and modelled records for the "best-fitting" model.

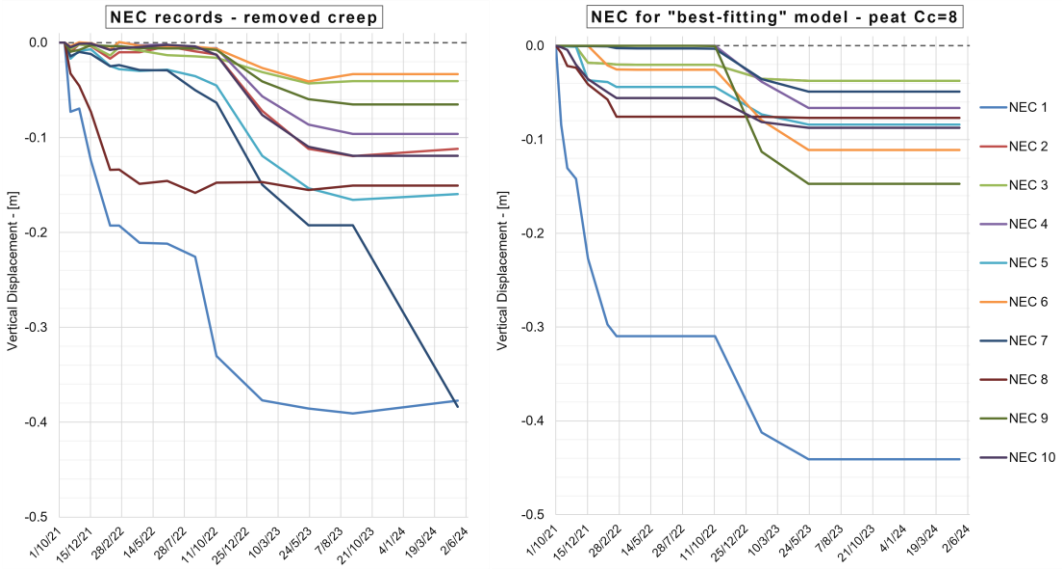

Figure 6.31. NEC creep-cleaned actual records (left) and corresponding modelled results (right).

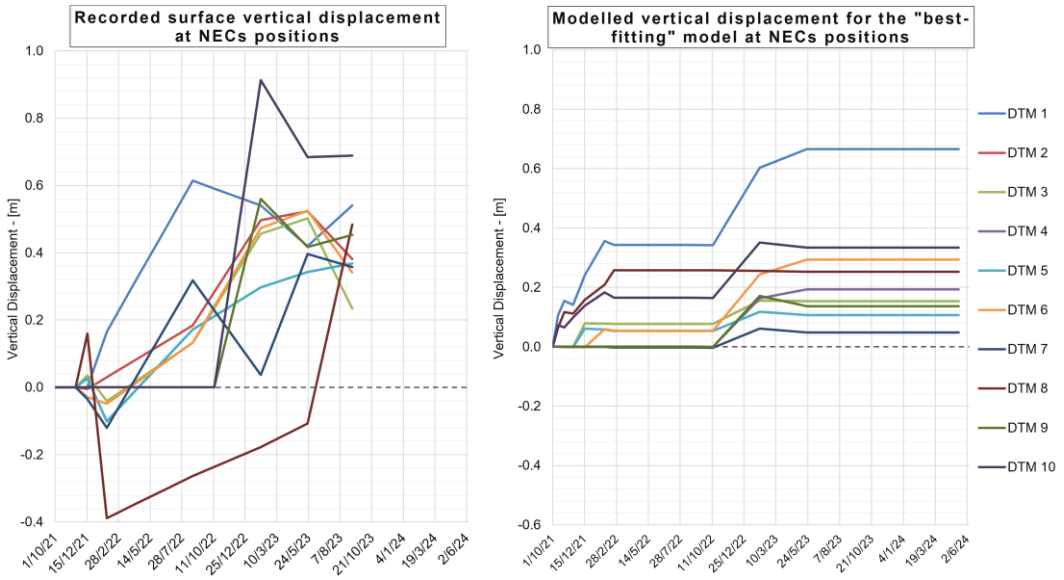

Figure 6.32. Actual (left) and modelled (right) displacement at the saltmarsh surface at NECs positions.

6.5. Final model analysis and prediction of the long-term evolution of Le Sorelle-B saltmarsh

The final model analysis concerns the results obtained with a compression index C_c of the peat equal to 8, which is considered the best-fitting model regarding the time measurements of the NECs. However, there are two critical issues: first, the subsidence curves of the DTM at the modeled NECs are less close to the real measurements compared to those of the initial model. The second issue arises from changing the C_c for a material whose properties were numerically calculated in previous studies through the decompaction process described in Section 4.4. Not repeating the decompaction process with this new compression index results in a final thickness of the peat layer that is underestimated compared to what is observed in the field through geological surveys (see Section 2.5).

These critical issues result in the model's bathymetry showing a generally lower elevation for the entire salt marsh surface at the end of peat deposition and subsequent moments when compared to the surface obtained with the initial model. The latter is validated since, in the simulation year 13639, it accurately represents the corresponding UniPD 2021 bathymetry.

To compensate for this excessive subsidence and still analyze the long-term evolution of the salt marsh in terms of elevations, the most relevant modeled bathymetries from the year 13639 onwards have been rigidly shifted upwards. The procedure for initial control and comparison and the translation is as it follows:

- Similarly to what was done for the NEC and DTM nodes in Section 5.2, the DTM files relative to the upper surface of the entire model at the times of interest were extracted from the vtk files;
- To analyze them with Surfer, maps of the salt marsh surface were obtained from the DTMs by creating the corresponding grids by kriging;

- The value for performing the aforementioned vertical translation Δh is equal to the difference of the arithmetic mean of the elevations of the 7840 nodes inside the contour obtained by "blanking" around the marsh perimeter;
- The elevation values of the modeled bathymetries of interest have been increased by Δh;
- With the same kriging and blanking operations, these were compared with the corresponding bathymetries and DTMs of the real salt marsh.

The computed mean elevation of the saltmarsh surface for the initial model is equal to - 0.5536 m.a.m.s.l, while the final or best-fitting model averages for - 0.7789 m.a.m.s.l. Hence, $\Delta h = 0.2253$ m. Figure 6.33 depicts the comparison between the actual 2021 UniPD bathymetry and the bathymetry of the final model at the corresponding time in the simulation before and after the upward translation.

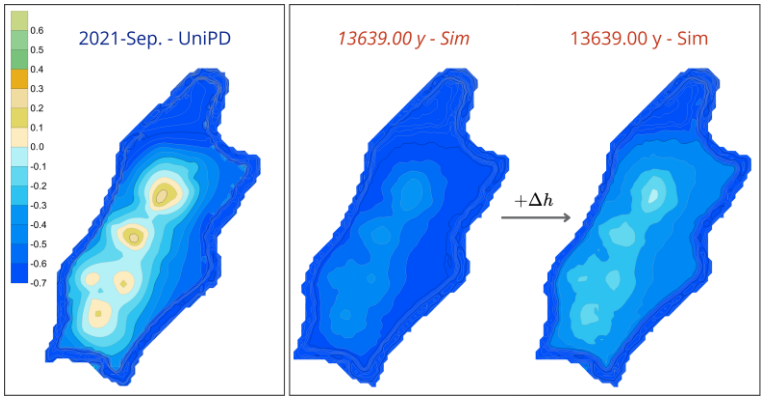

Figure 6.33. Upward translation of the final model bathymetry at year 13639 right before (center) and after (left) the 2021 nourishment in comparison to actual bathymetry of the same period (right).
Unit of measure in m.a.m.s.l.

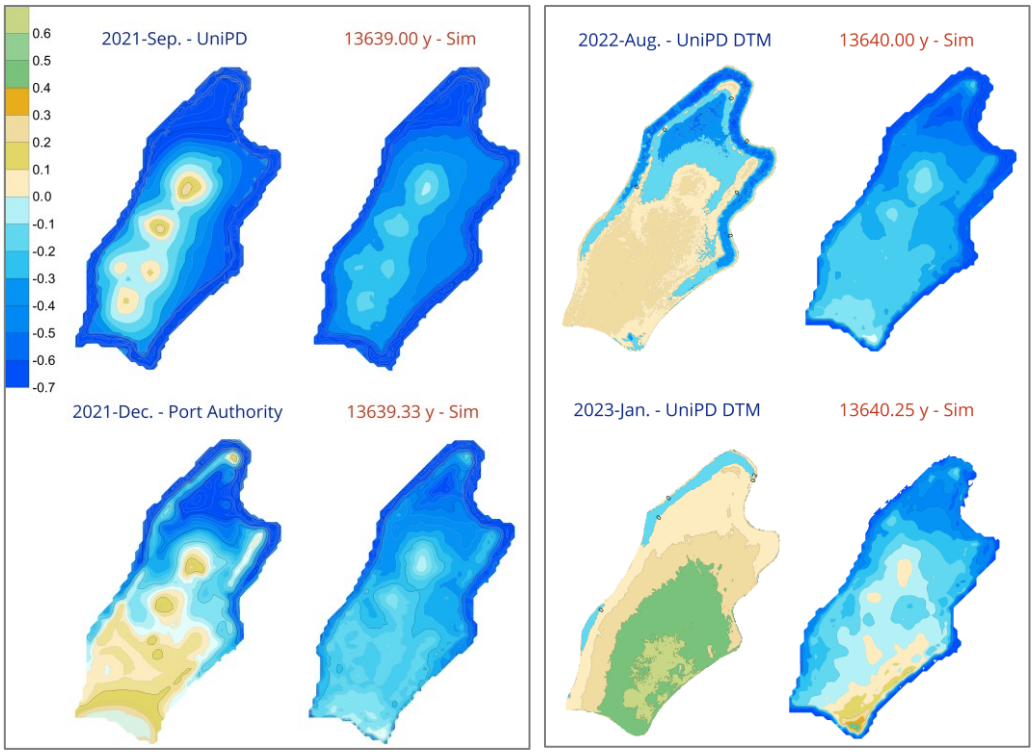

Figure 6.34. Actual bathymetries and DTMs (blue) compared with the translated model bathymetry (red) for 2021(left) and 2022 (right) nourishments.
From left to right, bathymetries on top row are relative to the beginning of nourishments respectively. On the contrary, the bottom row reports contour maps for end of the two nourishments. Unit of measure in m.a.m.s.l. and EPSG 3003 for 2021 nourishment and EPSG 3065 for 2022 one.

Note that the model bathymetries depicted in Figure 6.34 are already vertically translated by 0.2253 m, but this is still not sufficient to reach the same elevation values of the observed ones. Apart from this, there's a good match between the contours shape and their distribution suggesting that sedimentation rates are spatially consistent with actual sedimentation distribution and an overestimation of the overall subsidence. The lateral bluish contour fot he last two modelled bathymetries misleadingly represents the lagoon platform due to the fact that, as already mentioned, the saltmarsh perimeter used for the model cuts off part of the south-east portion.

Finally, bathymetries relative to the last recorded DTM (September 2023) and its relative modelled one (13642.34 y) are compared in Figure 6.35. At this time, it was observed that the model had already reached stationary condition at that time

so the second bathymetry can also be considered as the on that describe the long-term evolution.

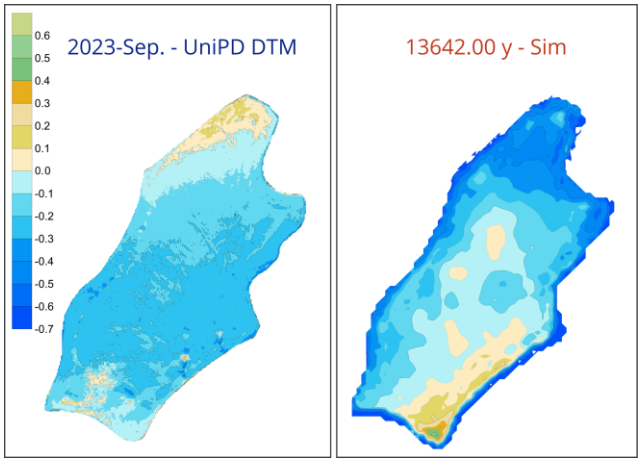

Figure 6.35. Comparison between the most recent actual (left) and modelled (right) bathymetry relative to September 2023.
Unit of measure in m.a.m.s.l.

Figures 6.36 and 6.37 report stress, strain, compaction and bulk compressibility values at 4 relevant times for the same section A-A' showed for the initial model in Paragraph 6.2.

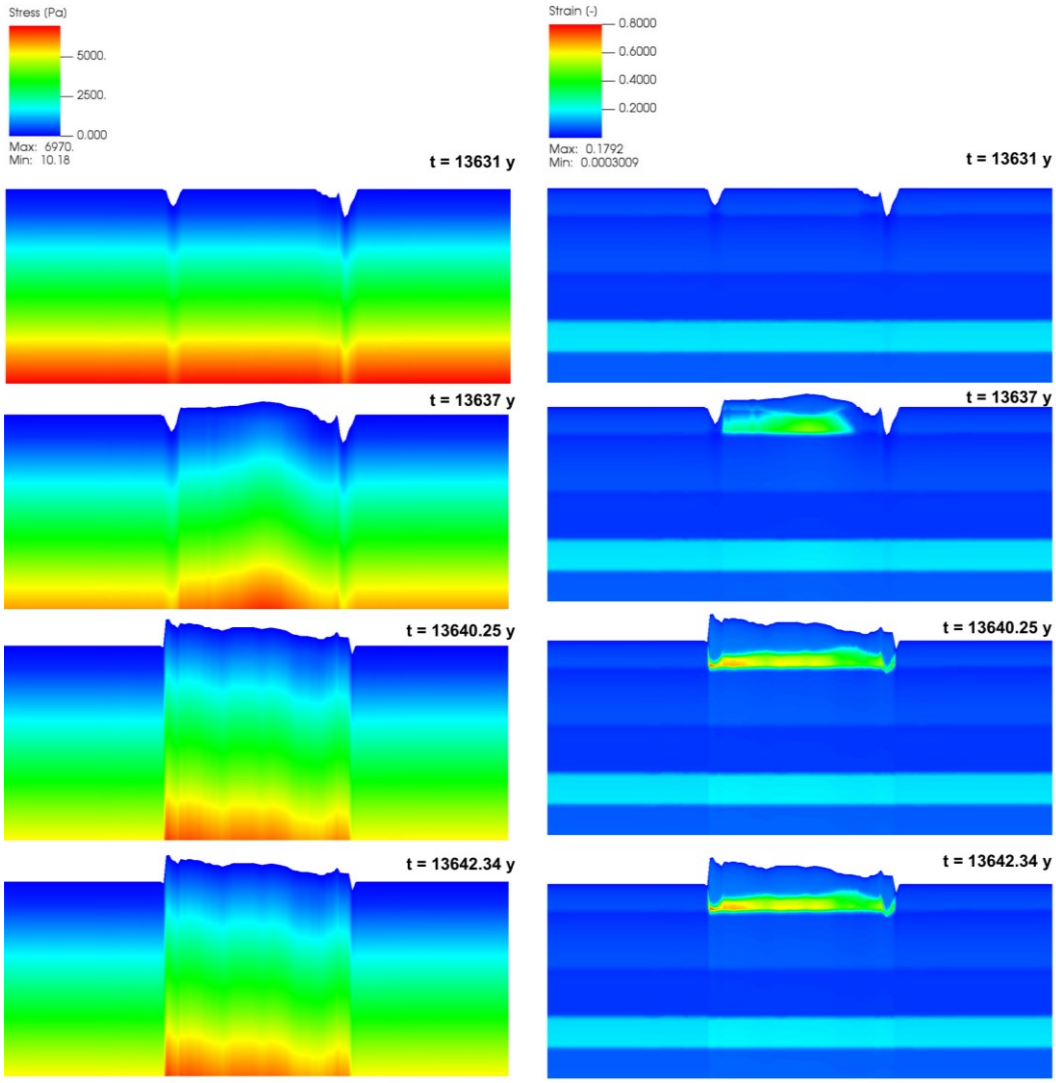

Figure 6.36. Stress and strain values at 4 relevant times for the section A-A'.
From top to bottom, the relevant times are: beginning of 2021 nourishment (13631 y); end of 2021 nourishment (13637 y); end of 2022 nourishment (13640.25 y); 1th January 2025 (13642.34 y) when the model has already reached stationary conditions.

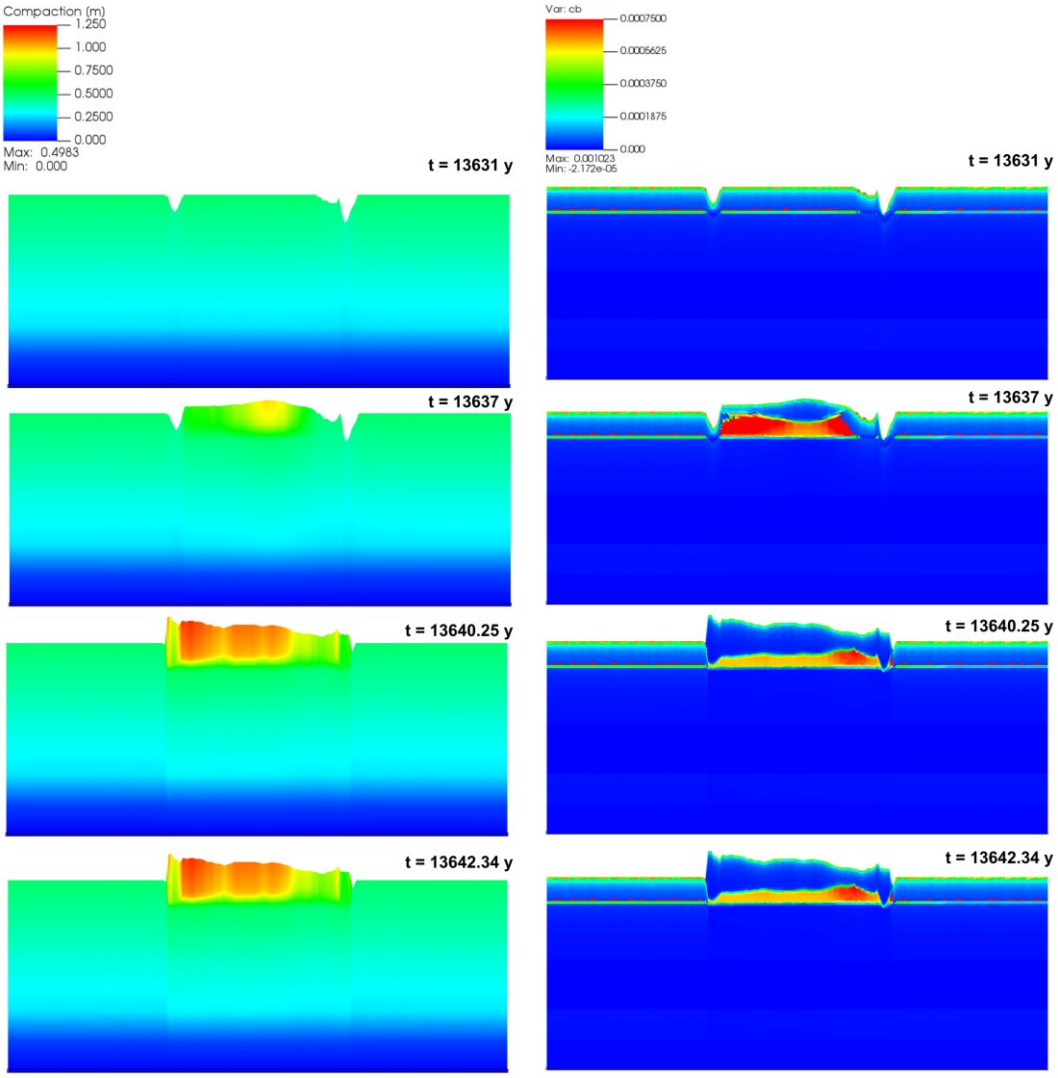

Figure 6.37. Compaction and compressibility values at 4 relevant times for the section A-A'.
From top to bottom, the relevant times are: beginning of 2021 nourishment (13631 y); end of 2021 nourishment (13637 y); end of 2022 nourishment (13640.25 y); 1th January 2025 (13642.34 y) when the model has already reached stationary conditions.

The figures above emphasize the substantial impact that increased compressibility of the peat layer has on the evolution of the salt marsh system. This relationship is critical to understand, as the compressibility directly influences the overall stability and subsidence rates of the salt marsh. A higher compressibility in the peat layer leads to greater settlement, which can significantly alter the topography and hydrodynamics of the marsh over time.

Furthermore, it is evident from the figures that the sediments deposited during the nourishment phases undergo the most significant autocompaction at any given time. These sediments are particularly susceptible to rapid consolidation due to the additional load imposed on them. The increased autocompaction of these nourished sediments can be attributed to their relatively loose initial state and the substantial overburden pressure they experience as new material is added.

7. Conclusion

The work carried out in this thesis is part of the restoration activities of the salt marshes in the Venice Lagoon. These areas are under significant stress due to a combination of factors, including the subsidence of the lagoon platform and sea-level rise driven by climate change. One fundamental aspect of marsh restoration design is determining its long-term elevation, which is crucial for the ecological functioning of the system and the landform's ability to keep pace with rising sea levels.

This study focused on the artificial salt marsh Le Sorelle-B (6.1 ha) with the aim of monitoring and modeling nourishment activities (3 phases), sediment autocompaction, and the consequent subsidence of the underlying layers to predict medium- to long-term evolution. The monitoring involved the use of various survey techniques and geological investigations, both traditional and modern, combined with new ten NEC monitoring stations installed at the study site. These stations allowed for the validation and calibration of the numerical model.

The NATSUB3D simulator was used to model the evolution of the salt marsh from the Holocene to the present day (approximately 13,600 years in total). It demonstrated that the medium-term evolution of the salt marsh system is heavily dependent on the geomechanical behavior of the layers formed during this period, as well as the sediments deposited through nourishment. The employed simulator effectively accounts for overpressure dissipation and large deformation caused by shallow soil autocompaction in a 3D setting.

The modelling results demonstrated that various factors significantly increase the response variability of the model. Proper quantification of the geomechanical characteristics of compressible soils is essential for more reliable predictions of the marsh's fate. In the case of the Le Sorelle-B marsh, significant compaction characterized the evolution of the natural sedimentary column over the Holocene.

The load of the nourishment deposits contributes to subsurface compaction, mainly concentrated in a shallow peat layer. Nourishment soil also compacted significantly, although this is likely an underestimate of the actual value. A more accurate assessment will be possible in the future as more specific field data become available. Currently, the marsh's ultimate elevation is expected to be within a range that would ensure the marsh's survivability in the mid-term.

While the reliability of the numerical model and the NATSUB3D simulator has been proven, it is necessary to report some limitations that have or may have influenced the consistency of the final results compared to real measurements. The first limitation is that the simulator was originally designed to model natural depositional processes, which have much slower sedimentation rates compared to those characterizing nourishments. Although the results are satisfactory, the simulator should be optimized or strengthened to handle these high-dynamic simulations. It would also be beneficial to make the restart feature more reliable, which unfortunately did not significantly reduce computational cost in this case because the recalculation of bulk compressibility was not adequately precise.

The perimeter of the salt marsh used to create the model mesh is derived from a previous thesis (Meneghini, 2022) and unfortunately does not include a part of the actual salt marsh: a significant portion of the modeled east side of the marsh is set back approximately 15 meters from the real perimeter of the containment. This discrepancy affected the determination of nourishment maps and their distribution in the model.

A significant component of the overall compaction affecting the salt marsh is due to secondary compaction (creep), which was not implemented in this thesis. While the simulator includes this function, it was decided not to introduce a multitude of additional variables that would have further complicated the validation and interpretation of the model. However, the results obtained provide an estimate of

the impact of secondary compaction on overall subsidence, demonstrating that it is a non-negligible phenomenon in describing these salt marsh restoration projects.

One function entirely absent from the simulator is the ability to model erosion. It is not possible to remove finite elements from the model, and therefore any sediment loss observed by comparing the time series of bathymetries and DTMs could not be modeled. Additionally, the excavation of the channel, which was necessary in 2019 for the establishment of the containment, could not be modeled following the actual timeline. Instead of simulating the peat sedimentation uniformly with nearly constant sedimentation rates over time and space, a reverse sedimentation rate was calculated to achieve the model with the already delineated channel.

In the preliminary phases, to visualize the rapid nourishment activities and subsequent compaction processes with higher temporal frequency, an attempt was made to introduce greater control over the output intervals when the software produces the output files. It was not possible to achieve the desired control because reducing the maximum timestep value beyond a minimum threshold resulted in matrix errors in the simulator. This issue has also been observed in other studies where overly fine temporal discretization caused such errors (Ferronato, Gambolati, and Teatini, n.d.). Despite not achieving the desired output frequency, the results obtained were still able to correlate correctly with real-time evolution without problematic gaps or shifts.

LIST OF FIGURES

LIST OF TABLES

REFERENCES

Barbier, Edward B., Sally D. Hacker, Chris Kennedy, Evamaria W. Koch, Adrian C. Stier, and Brian R. Silliman. 2011. "The Value of Estuarine and Coastal Ecosystem Services." *Ecological Monographs* 81 (2): 169–93. https://doi.org/10.1890/10-1510.1.

Calvin, Katherine, Dipak Dasgupta, Gerhard Krinner, Aditi Mukherji, Peter W. Thorne, Christopher Trisos, José Romero, et al. 2023. "IPCC, 2023: Climate Change 2023: Synthesis Report. Contribution of Working Groups I, II and III to the Sixth Assessment Report of the Intergovernmental Panel on Climate Change [Core Writing Team, H. Lee and J. Romero (Eds.)]. IPCC, Geneva, Switzerland." First. Intergovernmental Panel on Climate Change (IPCC). https://doi.org/10.59327/IPCC/AR6-9789291691647.

Campbell, Anthony D, Lola Fatoyinbo, Liza Goldberg, and David Lagomasino. n.d. "Global Hotspots of Salt Marsh Change and Carbon Emissions."

D'Alpaos, Chiara, and Andrea D'Alpaos. 2021. "The Valuation of Ecosystem Services in the Venice Lagoon: A Multicriteria Approach." *Sustainability* 13 (17): 9485. https://doi.org/10.3390/su13179485.

Ferronato, Massimiliano, Giuseppe Gambolati, and Pietro Teatini. n.d. "Ill-Conditioning of ®nite Element Poroelasticity Equations."

Finotello, Alvise, Davide Tognin, Luca Carniello, Massimiliano Ghinassi, Enrico Bertuzzo, and Andrea D'Alpaos. 2023. "Hydrodynamic Feedbacks of Salt-Marsh Loss in the Shallow Microtidal Back-Barrier Lagoon of Venice (Italy)." *Water Resources Research* 59 (3): e2022WR032881. https://doi.org/10.1029/2022WR032881.

Gambolati, Giuseppe. 1973a. "Equation for One-dimensional Vertical Flow of Groundwater: 1. The Rigorous Theory." *Water Resources Research* 9 (4): 1022–28. https://doi.org/10.1029/WR009i004p01022.

———. 1973b. "Equation for One-dimensional Vertical Flow of Groundwater: 2. Validity Range of the Diffusion Equation." *Water Resources Research* 9 (5): 1385–95. https://doi.org/10.1029/WR009i005p01385.

———. 1998. *Cenas: Coastline Evolution of the Upper Adriatic Sea Due to Sea Level Rise and Natural and Anthropogenic Land Subsidence*. Water Science and Technology Library, v. 28. Dordrecht: Springer Netherlands.

Koster, Kay, Jan Stafleu, and Esther Stouthamer. 2018. "Differential Subsidence in the Urbanised Coastal-Deltaic Plain of the Netherlands." *Netherlands Journal of Geosciences* 97 (4): 215–27. https://doi.org/10.1017/njg.2018.11.

"Land Subsidence in the Venetian Area: Known and Recent Aspects." 2005. *Giornale Di Geologia Applicata*, no. 1. https://doi.org/10.1474/GGA.2005-01.0-01.0001.

Miller, Carson B., Antonio B. Rodriguez, Molly C. Bost, Brent A. McKee, and Nathan D. McTigue. 2022. "Carbon Accumulation Rates Are Highest at

Young and Expanding Salt Marsh Edges." *Communications Earth & Environment* 3 (1): 173. https://doi.org/10.1038/s43247-022-00501-x.

Tognin, Davide, Andrea D'Alpaos, Marco Marani, and Luca Carniello. 2021. "Marsh Resilience to Sea-Level Rise Reduced by Storm-Surge Barriers in the Venice Lagoon." *Nature Geoscience* 14 (12): 906–11. https://doi.org/10.1038/s41561-021-00853-7.

Tosi, Luigi. 2024. "Vulnerability of Tidal Morphologies to Relative Sea-Level Rise in the Venice Lagoon." *Science of the Total Environment*.

Xotta, R., C. Zoccarato, P. S. J. Minderhoud, and P. Teatini. 2022. "Modeling the Role of Compaction in the Three-Dimensional Evolution of Depositional Environments." *Journal of Geophysical Research: Earth Surface* 127 (9): e2022JF006590. https://doi.org/10.1029/2022JF006590.

Zedler, Joy B. 2017. "What's New in Adaptive Management and Restoration of Coasts and Estuaries?" *Estuaries and Coasts* 40 (1): 1–21. https://doi.org/10.1007/s12237-016-0162-5.

Zoccarato, C., and P. Teatini. 2017. "Numerical Simulations of Holocene Salt-Marsh Dynamics under the Hypothesis of Large Soil Deformations." *Advances in Water Resources* 110 (December):107–19. https://doi.org/10.1016/j.advwatres.2017.10.006.

Zoccarato, Claudia, and Cristina Da Lio. 2021. "The Holocene Influence on the Future Evolution of the Venice Lagoon Tidal Marshes." *Communications Earth & Environment* 2 (1): 77. https://doi.org/10.1038/s43247-021-00144-4.

Bonardi, M., & Tosi, L. (1994). I sedimenti tardo quaternari del cordone litoraneo della laguna di Venezia: le sabbie. Technical Report CNR-ISMAR